EVERT NASEDKIN

SUB-STELLAR ATMOSPHERES IN THE MID INFRARED

Simulated Instrumental Constraints on Sub-Stellar Atmospheric Retrievals for the James Webb Space Telescope's Mid-Infrared Instrument.

Supervised by:
Sascha Quanz & Polychronis Patapis

Evert Nasedkin

Sub-Stellar Atmospheres in the Mid Infrared

Simulated Instrumental Constraints on Sub-Stellar Atmospheric Retrievals for the James Webb Space Telescope's Mid-Infrared Instrument.

Supervised by: Sascha Quanz and Polychronis Patapis

TITLEBACK

This document was written with LaTeX on Ubuntu using ArsClassica, designed by André Miede.

CONTACTS

☞ evertn@student.ethz.ch

Eidgenössische Technische Hochschule Zürich
Swiss Federal Institute of Technology Zurich

Declaration of originality

The signed declaration of originality is a component of every semester paper, Bachelor's thesis, Master's thesis and any other degree paper undertaken during the course of studies, including the respective electronic versions.

Lecturers may also require a declaration of originality for other written papers compiled for their courses.

I hereby confirm that I am the sole author of the written work here enclosed and that I have compiled it in my own words. Parts excepted are corrections of form and content by the supervisor.

Title of work (in block letters):

Authored by (in block letters):
For papers written by groups the names of all authors are required.

Name(s):

First name(s):

With my signature I confirm that
- I have committed none of the forms of plagiarism described in the 'Citation etiquette' information sheet.
- I have documented all methods, data and processes truthfully.
- I have not manipulated any data.
- I have mentioned all persons who were significant facilitators of the work.

I am aware that the work may be screened electronically for plagiarism.

Place, date

Signature(s)

For papers written by groups the names of all authors are required. Their signatures collectively guarantee the entire content of the written paper.

ACKNOWLEDGEMENTS

Astronomy compels the soul to look upwards
and leads us from this world to another.

— Plato

First and foremost I'd like to thank my supervisor, Sascha Quanz, for providing me with the guidance and resources with which to pursue this project. You have been an inspiration, and my experience here at ETH has set me down an exciting path in exoplanet research. It has been an honour to be a part of the growth of your group for the last two years, and I look forward to working with you in the future.

I have to thank the rest of the Exoplanet and Habitability Group for accepting me and teaching me over the last few years. Bibiana, thank you for our coffee discussions and your editing of this manuscript, I can't wait to see where you will go next. To Judit Szulagyi, I cannot thank you enough for your constant support and mentorship, both in and outside of academia. Your advice has helped shape the course of my future, and I will always be grateful for that. I'd especially like to thank Gabrielle Cugno for always answering my questions, Eleonara Alei for our discussions of atmospheres and music and Adrian Glauser for getting me started at ETH and involved with this project. And to all the rest: Anna, Franziska, Greta, Haiyang, Hans-Martin, Jie, Natalia, Silvan, Timothy and Tomas, thank you for our discussions, literature meetings, lessons and laughter. It has been a true pleasure to be a part of this group, I will miss it.

I must also thank my Zurich friends, without you it would have been impossible to survive here. You have all made this a truly memorable experience. Of course I have to thank my parents, Bill and Sherry, for supporting me in every possible way: not just here in Zurich, but throughout my life. I am eternally grateful for your love and encouragement.

Last, and certainly not least, I have to thank Polychronis Patapis for his supervision of this project. You got me into this and have set me on a path that I am excited to explore. I can't imagine many others answering my constant questions late at night, and for pushing me to always do better. I'm so grateful to call you not just my supervisor, but my friend. There will always be coffee waiting for you whenever you come to visit.

ABSTRACT

Following its launch in 2021, the James Webb Telescope will provide the best infrared observations of exoplanets and brown dwarfs to date. In particular, the Mid-Infrared Instrument (MIRI), will allow for medium resolution spectroscopy across a wide wavelength band, from 4.9-28.8μm. This will allow us to derive atmospheric properties of objects at lower temperatures than currently possible. MIRI's medium resolution spectrometer (MRS) is an integrated field unit that will perform these observations, providing both spatial and spectral information about targets. Understanding the instrumental effects is critical to analyzing data from MIRI. With that in mind, the MIRISIM instrumental simulator was developed to provide observational simulations of the various sub instruments of MIRI.

This thesis improves the implementation of a thin-film fringing model for point sources to MIRISIM, considering how the fringing effect from the detector layers varies with position. Fringing is a periodic, wavelength dependent effect, and thus has a strong impact on any spectroscopic observations. A comparison to the existing model was made, demonstrating the necessity of considering this effect when analyzing data. We will improve the fringing removal by identifying the point source location from the constructed data cube, and select the correct fringe flat for removal.

Understanding the instrumental effects is key to quantifying the ability of MIRI to derive atmospheric properties. Existing literature has considered the NIRCAM instrument and the MIRI Low-Resolution Spectrometer, but to date no retrieval studies have been performed using MIRISIM, or for the MIRI MRS, though it is critical to extend wavelength coverage to improve the results of an atmospheric retrieval. Model atmospheres will be generated using PetitRadTrans, and processed using MIRISIM and the JWST pipeline to produce a mock observation. An atmospheric retrieval will be performed, demonstrating to what extent MIRI will be able to retrieve atmospheric parameters such as temperature, pressure and composition. The posterior distributions of these parameters are compared with and without the fringing removal, again demonstrating the importance of correcting for this effect.

CONTENTS

1 INTRODUCTION

Since the first detection of a planet around a sun-like star (Mayor and Queloz, 1995) the field of exoplanets has evolved rapidly. Thousands of companions have been identified using the radial velocity and transit detection methods, and a handful have been imaged directly using both ground and space based observatories. In the last decade, many advances have been made that allow us to begin to characterize the properties of a few of these planets using spectroscopy. With the launch of the James Webb Space Telescope (JWST) in 2021, and the dawn of the era of extremely large telescopes, we will be able to peer deeper into these planets and further constrain atmospheric or geological properties. This will allow us to answer questions about their formation history, climate, and in the long term even the prospects for habitability and life.

JWST will operate in near to mid infrared wavelengths, which will provide a new window into studying the atmospheres of exoplanets and brown dwarfs. The Mid Infrared Instrument (MIRI) will provide unprecedented spectral resolution in the mid infrared, allowing for the measurement of composition, pressure and temperature. Novel instrumentation does not come without challenges. Optical and instrumental effects will constrain the ability to which we can measure spectral features, which will ultimately limit the science that can be accomplished.

In this thesis, we will measure the impact of thin-film fringing in the layers of the detectors in the MIRI Medium-Resolution Spectrometer (MRS) on measurements of atmospheric parameters of brown dwarfs and exoplanets. This will provide a baseline for determining the level of correction necessary to minimize the impact of fringing, as well as providing a first look into the ability of the MRS to characterize atmospheres through mid-infrared spectroscopic observations, and using modern atmospheric retrieval techniques.

1.1 EXOPLANETS

The last quarter century of observations has revealed the diversity of exoplanets and extra-solar systems. Both the architecture and individual planetary characteristics vary greatly when compared to each other, as well as to our own solar system. From the hot Jupiters initially found by Mayor and Queloz (Mayor and Queloz, 1995) to the thousands of planets discovered by the Kepler mission, the variety in exoplanets has raised questions about their formation and development, as well as their present day structure and climate. Improvements to observational techniques have allowed us to improve our understanding of these planets. Secondary eclipse and transmission spectroscopy has opened the door to the study of planets in close orbits to their host stars, while emission spectroscopy of young planet has allowed for constraints on models of planet formation. Over the next decades new instruments will be developed that improve sensitivity, allowing us to study smaller, colder and fainter planets. This will address one of the ultimate goals of exoplanet science in studying the atmospheric and surface features of an earth-like planet in the hopes of detecting unambiguous biosignatures.

Of particular interest are observable features that allow us to measure physical properties of exoplanets. The radial velocity (RV) method provides a measure of the planet mass, while a transit can constrain the radius. Already these properties tell us something about the overall structure of the planet. Spectroscopy can provide insight into the composition of the planet's atmosphere, as well as its temperature and pressure. These properties are linked to its age and location of formation in the circumstellar disk. The atmosphere, combined with the distance between the planet and its star determine the climate of the planet.

Direct Imaging

While the majority of exoplanet detections have been made using the radial velocity or transit techniques, direct imaging opens up the possibility of collecting light from the planet itself. This provides a window into the planet's atmosphere and surface. Most direct imaging to date has used near-to-mid infrared wavelengths, where the contrast between the thermal emission from the planet and the star is at a minimum, as in Fig. 2. This has its drawbacks: we are so far only able to image young planets that have retained some of the heat from their formation.

Direct imaging can make use of both ground and space based observatories. However, the high spatial resolution required drives the need for a large primary mirror, limiting the possibilities of space-based telescopes. On the other hand, atmospheric turbulence necessitates the use of an adaptive optics equipped facility to observe from the ground. Atmospheric absorption due to telluric lines (absorption lines of Earth's atmosphere) along with the strong background due to thermal emission from the ground and atmosphere also restrict infrared observations to narrow bands.

In addition to the requiring high spatial resolution, it is also challenging to separate the light emitted by the planet from that of the star. Imaging techniques such as Angular Differential Imaging (ADI) (Marois et al., 2006) and Reference Differential Imaging (RDI) (Lafrenière et al., 2009; Soummer et al., 2011) provide methods for reducing the stellar point-spread-function (PSF). Coronagraphs are optical elements which suppress the stellar PSF through self-destructive interference or physical occultation, depending on the position in the optical path. The difference in spectra between the planet and the star can also be used to separate the two sources.

Presently, 10m class telescopes such as the Very Large Telescope (VLT) in Paranal, Chile or the Gemini Observatory split between Hawaii and Chile provide the best combination of resolution and instrumentation to perform direct imaging of exoplanets. The NACO instrument at the VLT provided the first image of an exoplanet in 2004 (Chauvin et al., 2004). These observatories are among those equipped with an adaptive optics system, corona-

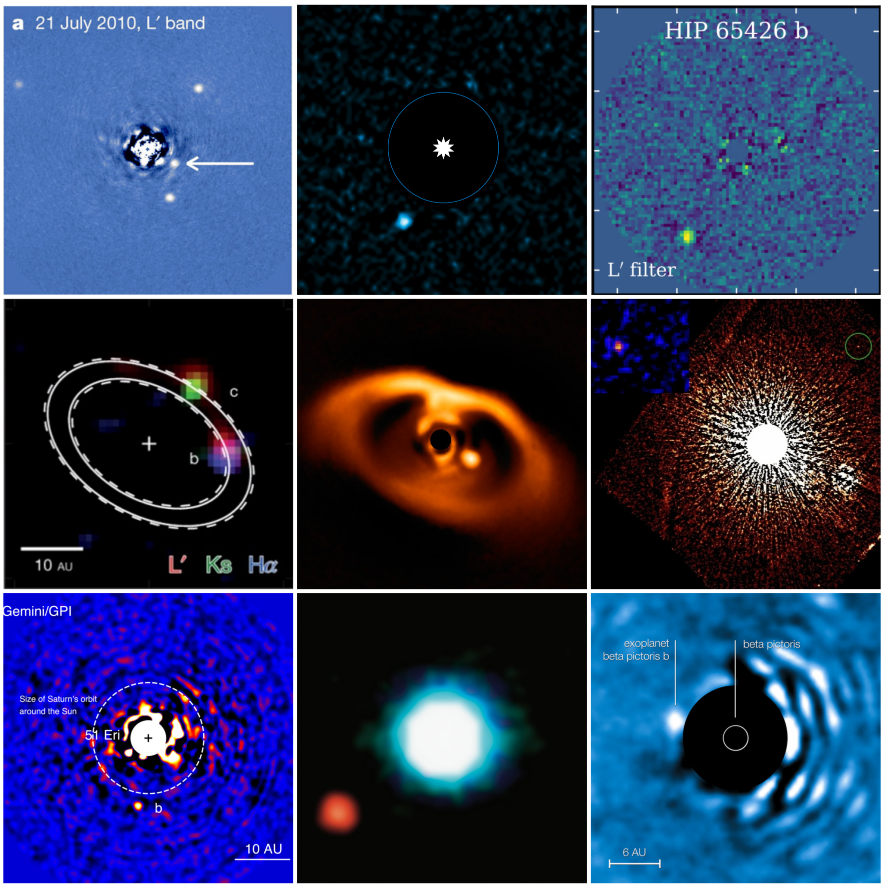

Figure 1: A family portrait of some of the directly imaged exoplanets. In order: (Marois et al., 2010), (Rameau et al., 2013), (Stolker et al., 2020), (Sallum et al., 2015), (M. Keppler et al., 2018), (Currie et al., 2012), (Macintosh et al., 2015), (Chauvin et al., 2004), (Quanz et al., 2010).

graphic instrumentation and near to mid infrared imaging and spectroscopic capabilities to directly image exoplanets, with several exemplar systems becoming standard objects of interest. While it's terribly interesting to explore the details of each of these objects, we will focus our discussion on objects will be used further in this study, due to their scheduled observation as part of the JWST GTO and Early Release Science (ERS) programs (Charles A Beichman et al., 2019c). The parameters of these and other directly imaged exoplanets and brown dwarfs are summarized in table 1.

In order to understand these objects, we must use a measured spectrum in order to infer physical properties. Parameters such as the carbon-to-oxygen (C/O) ratio provide insight into formation mechanisms (Nikku Madhusudhan, 2012). A planet that forms near its star will form in a hot region of the circumstellar disk, with a depletion of volatiles due to the high temperature - various species will freeze out at different radii within the disk. The measured C/O ratio of a planet will thus depend on its initial formation location and its migration path. (Turrini et al., 2015) outlines several formation pathways and how the C/O ratio will be affected. The current climate of exoplanets is also of interest. This requires inferences of atmospheric composition and structure from the spectrum, and will ultimately require time resolved measurements in order to study dynamics and variability.

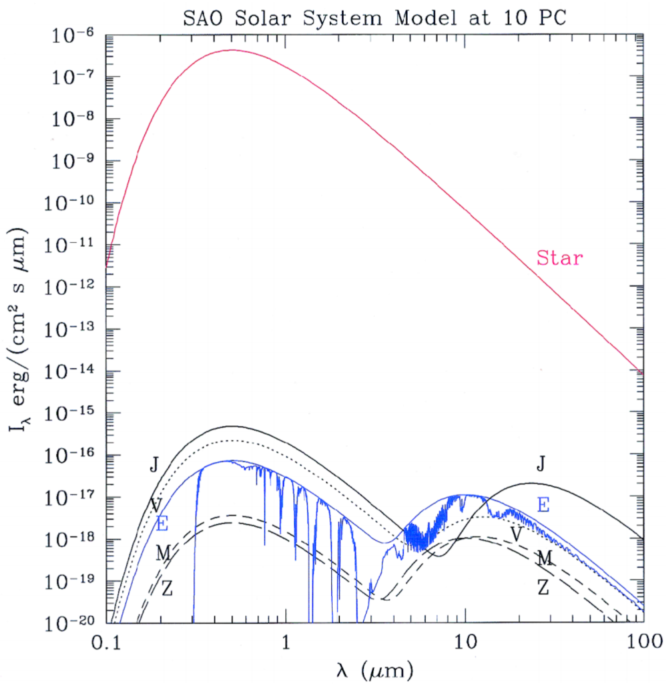

Figure 2: SAO solar system model at 10pc, illustrating the vast difference in luminosity between the Sun and the surrounding planets. However, in the mid infrared the contrast is dramatically reduced at the peak of the planet's emission spectra (Des Marais et al., 2002).

VHS-1256 b

Originally discovered in 2015 (Gauza et al., 2015) as part of the VISTA Hemisphere Survey, VHS-1256b is a late-L dwarf in a 102 AU orbit around an M dwarf. (Gauza et al., 2015) present astrometric, photometric and spectroscopic data on the planet, finding an age of 150-300 Myr from a moving group association, a luminosity $\log(L_{bol}/L_{\odot})$ of -5.05±0.22 and infer a mass of $11.2^{+9.2}_{-1.8}$ M_J. The effective temperature is found to be 880^{+140}_{-110} K from evolutionary models. This is substantially colder than field dwarfs of a similar spectral type (typically 1400K), and so it is proposed that a thick Fe and Mg-Si cloud layer acts to reduce the effective temperature. Similar findings are presented by (Rich et al., 2016) using Subaru/IRCS.

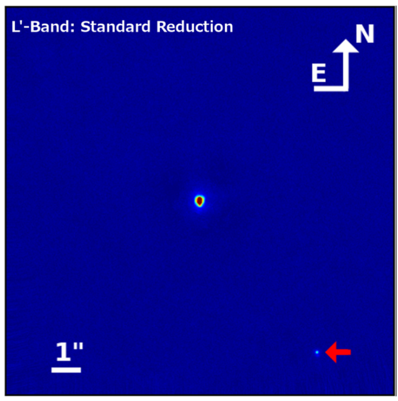

Figure 3: VHS-1256b as observed with Subaru/IRCS in the L′-band (Rich et al., 2016), reduced using the LOCI algorithm (Galicher et al., 2011).

In (Miles et al., 2018), methane is detected using KECK/NIRSPEC in the L-band. The shallow depth of the feature indicates chemical disequilibrium in the photosphere, as the derived abundance departs from an equilibrium abundance by a factor of 10-100.

However, the best fit model retrieves substantially different parameters for temperature (1240 K) when compared to previously published results.

The wide separation (8") and proximity to Earth make VHS-1256b an ideal target for studying atmospheric properties. It will be observed as part of the JWST ERS Program (Hinkley et al., 2019), where a medium resolution spectrum (R≥1700) will be measured from 0.6-28 micron. This will enable a more precise measurement of the abundance of methane and other species in the atmosphere, and will allow for investigation of the cloud properties in the mid infrared.

2M1207b

Using VLT/NACO, (Chauvin et al., 2004) discovered a low mass companion to the brown dwarf 2MASSWJ 1207334-393254 (2M1207) at a separation of 0.8", or 55 AU, shown bottom-center in Fig 1. From their H,K and L′-band photometric observations and NIR spectroscopic measurements, 2M1207b was found to have a spectral type of L5-L9.5, a mass of 5±2 M_J and an effective temperature of 1250±200 K. Followup VLT/NACO observations from (Mohanty et al., 2007) found a higher effective temperature of 1600±100 K, and a higher mass of 8±2 M_J, pushing it closer to the deuterium burning limit. More recent observations have measured periodic signals due to rotation and variability, but failed to constrain the rotation rate due to pointing variance (Zhou et al., 2019).

(Zhou et al., 2019) also present simulated JWST/NIRCAM observations of 2M1207b. Access to medium resolution spectroscopy in the mid infrared will allow the characterization of cloud condensate properties. The improvement in photometric precision by an order of magnitude will allow better measurement of the rotation rate and variability, and the increase in sensitivity will place lower limits on the possibility of further companions within the system. It will be observed as part of the JWST GTO program (Birkmann et al., 2019).

Name	d [pc]	Mass [M_J]	Sep [AU]	Sep ["]	Age [Myr]	$\log(L_{bol}/L_\odot)$	T_{eff} [K]	References
Widely separated companions								
VHS 1256b	12.7 ± 1.0	2 ± 1	102	8.1	$10^3 - 10^4$	-5.05 ± 0.22	880	(Gauza et al., 2015)
Fomalhaut b	7.704 ± 0.028	≤ 2	119	13	440 ± 40	...	1600 ± 100	
Close in companions								
2M1207b	152.4 ± 1.1	2 ± 1	41	0.8	10 ± 3	-4.68 ± 0.05	1600 ± 100	
51 Eridani b	29.4 ± 0.3	2 ± 1	13	0.45	23 ± 3	-5.06 ± 0.2	700	(Macintosh et al., 2015)
β Pic b	19.3 ± 0.2	2 ± 1	9	0.4	23 ± 3	-3.78 ± 0.03	1600 ± 100	(Quanz et al., 2010)
GJ 504b	17.56 ± 0.08	$3 - 30$	44	2.5	$100 - 6500$	-6.13 ± 0.03	544	(Skemer et al., 2016a)
HD 95086b	90.4 ± 3.3	5 ± 2	56	0.6	17 ± 4	-4.96 ± 0.10	1050	(De Rosa et al., 2016)
HR8799b	39.4 ± 1.0	5 ± 1	68	1.7	40 ± 5	-5.1 ± 0.1	870^{+30}_{-70}	(Marois et al., 2008; Skemer et al., 2012)
HR8799c	39.4 ± 1.0	7 ± 2	38	0.95	40 ± 5	-4.7 ± 0.1	1090^{+10}_{-90}	(Marois et al., 2008; Skemer et al., 2012)
HR8799d	39.4 ± 1.0	7 ± 2	24	0.62	40 ± 5	-4.7 ± 0.2	1090^{+10}_{-90}	(Marois et al., 2008; Skemer et al., 2012)
HR8799e	39.4 ± 1.0	7 ± 2	14	0.38	40 ± 5	-4.7 ± 0.2	1000	(Marois et al., 2008; Skemer et al., 2012)
LkCa 15b	145 ± 15	6 ± 4	20	0.08	2 ± 1	...	...	
PDS 70b	113.43 ± 0.52	7 ± 2	23	0.19	5 ± 1	...	900	(Haffert et al., 2019)
PDS 70c	113.43 ± 0.52	4.4 ± 1	30	0.24	5 ± 1	...	10^4	(Haffert et al., 2019)
Nearby Brown Dwarfs								
WISE 0855	2.2 ± 0.2	$3 - 10$	...	...	$10^3 - 10^4$	-10.5	$225 - 260$	(Luhman, 2014; Tinney et al., 2014)
Luhman 16B	1.998 ± 0.0004	28.6 ± 0.3	...	...	$600 - 800$	-4.68	1201	(Sahlmann and Lazorenko, 2015); (Garcia et al., 2017)

Table 1: Summary of directly imaged planet and brown dwarf parameters based on (Bowler, 2016) and references therein. Luminosity for WISE 0855 is calculated in H band.

1.2 BROWN DWARFS

Brown dwarfs are the low mass result of a failed star formation process. On the low end of the mass scale, an object is considered a brown dwarf at >13M_J, which is the deuterium burning limit. Recent observations of low mass (1 M_J), free floating observations have led to challenges of this definition defining the boundaries between planets and brown dwarfs. By 75M_J, the object is heavy enough to sustain hydrogen fusion and the object is considered a star. However, there have recently been observations even lower mass brown dwarfs, down to several Jupiter masses, raising questions of formation processes (Luhman, 2014). It is generally thought that brown dwarfs form during the gravitational collapse of a molecular cloud, while exoplanets form through a core accretion process in a circumstellar disk. Observations of high mass companions and low mass field objects then challenge these standard models.

While brown dwarfs are objects of scientific interest in their own right, we are particularly interested in their use as analogs for exoplanets due to their similar temperatures and pressures. Without the issue of contrast between an exoplanet and its host star, brown dwarfs are ideal targets for medium and high resolution spectroscopic characterization. As shown in table 1, they are also some of the closest known objects to the solar system, with several having been observed at around 2pc.

1.2.1 Observational Properties

Brown dwarfs are characterized by their spectral type, either by comparison to spectral templates, using indices derived from spectral parameters or through broadband photometric comparison (Helling and Casewell, 2014). Directly imaged exoplanets can also be classified using brown dwarf spectral types. Unlike stars which maintain their temperature and luminosity through fusion, brown dwarfs cool and change their spectral type with age, leading to a degeneracy between mass and age (Burrows et al., 2001). This spectral series is shown in Fig. 4.

As a brown dwarf cools and contracts over time, its surface gravity will increase, leading to the use of log(g) as a tracer of age (Manjavacas, 2014). Young, low surface gravity objects are particularly comparable to directly imaged exoplanets. In these young objects, clouds are a nearly universal feature (Cooper et al., 2003; Helling and Casewell, 2014), with thicker cloud decks appearing in low gravity objects (Helling and Casewell, 2014).

L-Type

L-dwarfs are the hottest brown dwarfs, with typical effective temperatures between 1300 K and 2100 K (Burrows et al., 2001). L-type spectra are notable for the disappearance of VO and TiO NIR absorption lines and the onset of molecular absorption features such as H_2O and CO, with CH_4 appearing in late L types (Manjavacas, 2014). Further key features of L-dwarfs is the formation of iron and silicate condensate, as well as the growth of neutral alkali lines (Burrows et al., 2001).

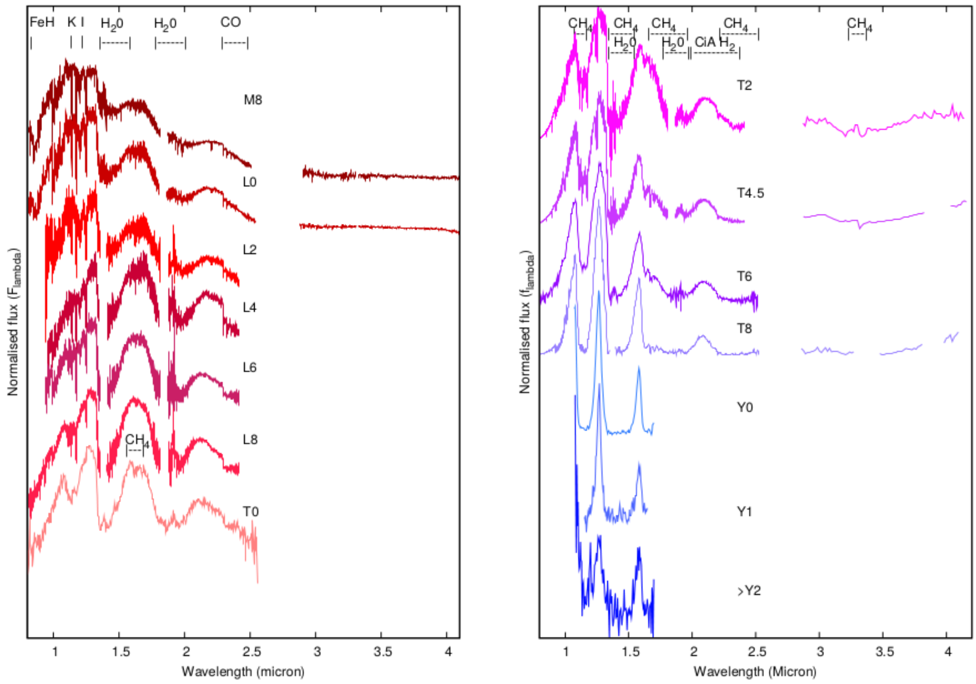

Figure 4: Near Infrared spectral series of brown dwarfs from early-M to early-Y as shown in (Helling and Casewell, 2014).

T-Type

As a brown dwarf ages it moves towards a T-type spectrum. The L/T transition occurs with the appearance of both CH_4 and CO absorption, and is characterized by increasingly blue J-H colour as the temperature decreases. There are several proposed mechanisms for this transition, with cloud fragmentation due to particle microphysics (Burningham et al., 2017) and convection processes being two examples (Tremblin et al., 2015). Both T- and L-dwarfs are highly variable due to complex atmospheric dynamics ranging from clouds to banding structures to hot spots and more (B. Biller, 2017). (Vos et al., 2019) presents how monitoring with JWST/MIRI will be able to constrain the mechanism behind this transition.

Y-Type

Y-type dwarfs are ultra-cool objects first discovered in (Cushing et al., 2011). With such cold temperatures, they contain deeper water and methane absorption features than present in T-dwarfs, and likely have ammonia present as well. Atmospheric models suggest typical temperatures between 300-500 K, which places them as the coldest detected and spectroscopically measured brown dwarfs to date (Cushing et al., 2011). Due to the very low temperatures of Y-dwarfs, mid-infrared observations are ideal for detection and characterization. Most spectral features of interest (CH_4,NH_3,etc) will be present at longer wavelengths, while the mid infrared will also present opportunities for measurements of cloud properties and composition.

WISE 0855-0714

WISE-0855 is the coldest known brown dwarf at 250 K, with an inferred mass of 5 M_J (Luhman, 2014), and a Y2-4 spectral type (Leggett et al., 2015). Although faint, with a J-band magnitude of 25, its proximity to the sun makes allows for its spectral characterization. Present measurements indicate the presence of ammonia (Leggett et al., 2015) and water clouds (Jacqueline K Faherty et al., 2018; Morley et al., 2014) in its atmosphere.

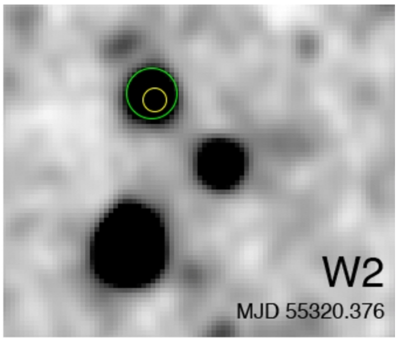

Figure 5: W2, epoch 1 image of WISE0855 on top of a known background clump. The green circle represents the location of WISE0855, the yellow is the position of the background source (E. L. Wright et al., 2014).

WISE 0855, along with other Y-dwarfs will be the subject of JWST investigation (Oliveira, 2015; Oliveira et al., 2019). Its low mass and cold temperature make it the closest analog to solar system objects, especially to Jupiter. Further observations will allow for tighter constraints on atmospheric composition and cloud properties, as well as insight into whether such objects are the result of a star-like formation process or are an ejected, free floating planet (C. Beichman et al., 2014).

1.3 MOTIVATION

1.3.1 Current Status of Atmospheric Characterization

Both exoplanets and brown dwarfs raise interesting questions with regards to atmospheric properties, but there are substantial challenges both in gathering the data necessary to answer them and modeling the physics underlying the observable parameters. The best methods currently in use involve taking spectroscopic data and inferring atmospheric properties from the spectral features. The light we measure may be thermal emission from the planet, where it is absorbed and scattered as it passes through the planet's atmosphere, or it may be light from the planet's host star which passes through the upper layers of the atmosphere. These provide complementary information about the composition and structure of the atmosphere, probing different altitudes and pressures. While a more complete overview of exoplanet atmospheres is covered in the literature, e.g. (Nikku Madhusudhan et al., 2014; Sara Seager and Deming, 2010; Sing et al., 2018), we will briefly summarize the current methods used and what has been learned so far.

Transmission Spectroscopy

Many exoplanets have been discovered using the transit technique in which the planet passes in front of its host star, blocking a small fraction of its light.

Through time series observations, particularly with satellites such as Hubble, Kepler, and TESS, we can observe this dip in stellar brightness, and infer properties of the planet. A key feature of this observation is that in the case the planet has an atmosphere, the brightness dip is wavelength dependent. Depending on the wavelength, different species within the atmosphere will absorb the light to a greater or lesser extent. Thus if a species is abundant within the atmosphere, it will create deep absorption features, which will make the apparent radius of the planet larger, increasing the transit depth. Measuring this radius variation is the procedure of transmission spectroscopy, and is used to probe the composition and structure of the upper atmospheres of transiting planets. In addition to transmission spectroscopy, secondary eclipse spectroscopy is another transit measurement that uses the reflected light and thermal emission of the planet, and measures the dip in total luminosity as the planet passes behind its host star. This provides a more direct measurement of the planet's reflection or emission spectrum. (Kreidberg, 2018) presents a concise overview of transmission and eclipse spectroscopy.

Transmission spectroscopy attempts to answer questions about atmospheric composition, formation history and present climate. To date, water features and carbon-bearing molecules have been detected, though molecules commonly present in the solar system such as methane and ammonia have not been detected, largely due to lack of long wavelength coverage and the high temperatures of most transiting planets (Kreidberg, 2018; Lee et al., 2012). The C/O ratio has been measured in some hot Jupiters, including WAST-12b, which provides a trace for formation history and current composition (Nikku Madhusudhan et al., 2011). For WASP-12b, the high C/O ratio (>1) and the lack of an observed thermal inversion in the highly irradiated atmosphere both stand in contrast to theoretical predictions, and demonstrate the necessity for improvements in atmospheric and formation modeling (Nikku Madhusudhan et al., 2011). In other atmospheres, nitrogen chemistry has been observed, and condensates (clouds and hazes) are nearly universal (MacDonald and Nikku Madhusudhan, 2017). Water has been detected on hot Jupiters (Kreidberg et al., 2014), as well as on smaller planets within the 'habitable zone' (Björn Benneke et al., 2019; Tsiaras et al., 2019).

Future observations will increase the spectral resolution of transit observations, and will also extend the wavelength coverage. By probing the mid infrared, it may be possible to determine the composition of the clouds observed, and place tighter constraints of the abundances of species present within atmospheres (Kreidberg, 2018).

Emission Spectroscopy

In contrast to transit observations, emission spectroscopy is a direct measurement of the light emitted by the planet, usually in the infrared, where the planet's luminosity peaks due to Wein's law. Due to the low levels of flux emitted from most planets, most emission spectroscopy to date has been low to medium resolution, in order to collect enough light for measurement. However, this has already allowed us to begin to answer similar questions as posed for transmission spectroscopy. What are these atmospheres made of?

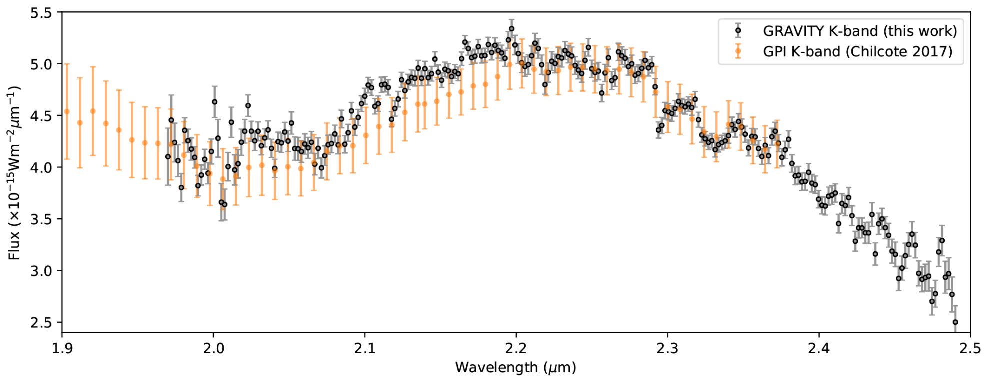

Figure 6: Flux calibrated K-Band emission spectrum of β Pic b as measured using the VLTI/GRAVITY at R=500 (GRAVITY Collaboration et al., 2020), along with the GPi K-Band spectrum from (Chilcote et al., 2017).

How did these planets form? In many ways though, emission and transmission spectroscopy provide complementary information, and multiple ways of approaching these problems. Due to the different wavelength regimes, they are able to identify different species and probe different atmospheric depths.

Only recently has high quality exoplanet emission spectroscopy become possible, and a comprehensive overview is provided in (B. A. Biller and Bonnefoy, 2018). Measurements of Hα emission in LkCa 15b have allowed for inferences of the mass accretion rate of a forming planet (Sallum et al., 2015), while observations of the PDS 70 system indicate the presence of a circumplanetary disk around PDS 70b (Christiaens et al., 2019; M. Keppler et al., 2018). With integrated field spectroscopy, (Hoeijmakers et al., 2018) show how spectroscopy can identify the presence of molecular species in a spectrum and how this can be used to discover companions within the contrast-limited regime. Using the VLTI/GRAVITY instrument, which combines light from all four Unit Telescopes (UTs) of the VLT into a single interferometer, medium resolution (R=500) spectra have been taken of HR 8799e (Lacour et al., 2019) and β Pic b (GRAVITY Collaboration et al., 2020), the latter of which is shown in Fig. 6. These spectra represent some of the best data available to date for exoplanets, and additional observations of well-known directly imaged planets are planned in the near future. With such spectra, atmospheric retrievals are used to infer properties of interest using Bayesian inference, fitting parameterized 1D atmospheric models to the spectrum in order to find the most likely value of those parameters (Madhusudhan and Seager, 2009). While not yet accomplished for an exoplanet, it may be possible in the near future to longitudinally map cloud features of exoplanets, as has already been accomplished for brown dwarfs using the CRIRES instrument (Crossfield et al., 2014).

As most older planets will emit primarily in the thermal infrared, JWST/MIRI will provide unprecedented capabilities at imaging and characterizing these systems. (Danielski et al., 2018) shows that the MIRI Low Resolution Spectrometer will allow for the detection of ammonia in the coldest targets, as well as characterize the abundances of other molecules such as

CH_4, H_2O, CO_2 and PH_3. Many direct imaging observations of exoplanets have been proposed as part of the JWST GTO and ERS programs. In a white paper, (Charles A Beichman et al., 2019c) discuss how JWST will provide new insight into exoplanet atmospheres using direct emission imaging and spectroscopy, while (Michael R Line et al., 2019) examines the possibility of characterizing terrestrial planets using thermal emission spectroscopy.

1.3.2 JWST Studies

With the launch of JWST imminent, many proposals have been made to cover a wide range of science cases, as well as performing instrumental testing, calibration and validation. Exoplanet science is well represented within these first observations, and several of the proposals will be presented here.

Early Release Science

The Early Release Science program is an initiative designed to help scientists develop an understanding of the instruments available on JWST, as well as the tools needed to process the data. Thus the ERS provides an extensive catalog of public data immediately upon observation, and will take place within the first 5 months of JWST science operations. Both a transiting program (Bean et al., 2018) and a direct imaging program (Hinkley et al., 2019) have been approved. The direct imaging proposal has 52 hours observing time in order to take data using the full range of JWST instrumentation and observing modes. The goal is to image a representative sample of known directly imaged planets, in order to develop the tools and techniques necessary to push the limits of the instrumentation. For a subset of the imaged planets, including VHS-1256b, spectroscopic data covering the full wavelength range of JWST will be taken using a combination of the available instruments.

GTO Programs

In addition to the ERS program, the Guaranteed Time Observations (GTO) program is designed to provide scientists who helped in the development of JWST hardware and software with a set amount of observing time. Many GTO programs focused on exoplanet science have been approved, including spectroscopic studies of 2M1207b and other commonly studied systems (Birkmann et al., 2019). Brown dwarf science is also well represented within the GTO program, with WISE-0855 receiving full spectroscopic coverage from 0.6-28 μm (Oliveira et al., 2019). Details of the observations for VHS-1256b, 2M1207b and WISE-0855 are discussed in 4.3.

1.3.3 Biosignatures and Future Missions

While JWST will provide higher spectral and spatial resolution in the infrared than any previous observatory, many questions will remain open for future missions. One of the ultimate unanswered questions in science is "Are we alone?". The detection of biosignatures in the near future with next generation 40 m class telescopes (López-Morales et al., 2019) or proposed space missions such as LIFE (Quanz et al., 2019) and LUVOIR (LUVOIR Mission Concept Study Team, 2019) may provide our best chance at answering such questions. Instruments such as METIS on the ELT will offer high resolution (R=100000) integral field spectroscopy of nearby terrestrial planets, while both proposed space missions will have the spatial and spectral resolution necessary to characterize a nearby earth like planet. With such a goal in mind, it is necessary to develop the technical capabilities in both theory and observation order to achieve such ambitious goals in the not-so-distant future.

1.4 THESIS OVERVIEW

With sufficient background and motivation, we will now outline the remainder of this thesis.

Chapter 2 will provide a more extensive background of the James Webb Space Telescope, and in particular the MIRI Medium Resolution Spectrometer (MRS). We will outline the principle optical components dedicated to integral field spectroscopy, as well as the detector characteristics of MIRI. This will provide the necessary background to understand the instrumental and optical effects discussed in Chapter 3.

The third chapter examines the fringing effect in the MIRI MRS instrument. We discuss the optical effects that result in fringing patterns, as well as outlining current and future strategies for fringe correction. We describe the creation and processing of our mock observations using the MIRI instrumental simulator and the JWST data reduction pipeline. With the degraded spectra from the simulated data, we measure the impact of fringing on spectral extraction using cross correlation techniques, and and how this impacts molecular mapping studies. This in turn motivates Chapter 4, where the species identified using molecular mapping can justify the inclusion or exclusion of particular species in an atmospheric retrieval.

In Chapter 4 we explore atmospheric retrievals with the MIRI MRS. We outline our procedure for performing a retrieval using the petitRADTRANS radiative transfer code and Multinest as an implementation of the nested sampling strategy for parameter space exploration. We measure the impact of fringing on parameter estimation, and also investigate how observing parameters will impact retrievals, discussing the advantages and challenges of studying atmospheres in the mid infrared.

Finally we summarize and discuss our findings and future investigations in Chapter 5.

2 MIRI: THE MID-INFRARED INSTRUMENT

MIRI is an instrument that will provide unique capabilities for studying exoplanets and other cold and distant objects. This chapter will provide a detailed overview of the technical details and capabilities of the instrument. A complete description of MIRI is provided in a series of papers from (Boccaletti et al., 2015; Bouchet et al., 2015; Glasse et al., 2015; P. Lagage et al., 2015; Ressler et al., 2015; Rieke et al., 2015a,c; Wells et al., 2015; G. S. Wright et al., 2015).

2.1 THE JAMES WEBB SPACE TELESCOPE

JWST is a 6.5 m space based observatory built in collaboration between NASA, ESA and CSA that will be located in a halo orbit at the L2 Earth-Sun Lagrange point. As the successor to the Hubble Space Telescope and the Spitzer Space Telescope, it will provide a new perspective for infrared astronomy. It is currently scheduled to launch in March 2021.

James Webb is fully optimized for infrared astronomy. To reduce instrumental thermal background, the entire telescope will operate at cryogenic temperatures. A large sun-shield will help block solar infrared radiation. The lightweight beryllium mirrors are coated in gold to maximize reflectivity out to the mid infrared.

Of key interest to exoplanet science is the both the sensitivity and spatial resolution of the instrument. With its 6.5 m primary, JWST will have a spatial resolution from 0.01" at 0.6 micron to 0.92" at 29 micron. The increase in sensitivity is due in part to the larger collecting area, but also to advances in detector technology since the previous generation of infrared observatories. For example, the MIRI instrument will have a minimum detectable flux of 0.13 μJy at 5.6 micron and a 10 000 second integration, or roughly a factor of 1000 better than what was possible with the Spitzer Space Telescope (Glasse et al., 2015).

There are four primary instruments that constitute the Integrated Science Instrument Module (ISIM). Near-Infrared Camera (NIRCam), which provides imaging with coronagraphic capabilities from 0.6-5 micron. The Near-Infrared Spectrograph (NIRSpec) provides fixed slit and integrated field unit spectroscopy capable of analyzing multiple objects simultaneously, and operates in the same wavelength range as NIRCam. The Fine Guidance Sensor/ Near-Infrared Imager and Slitless Spectrograph (FGS/NIRISS) allows for low and medium resolution spectroscopy with high photometric stability, as well as aperture masking interferometry. The final instrument, MIRI, is the subject of this thesis.

Figure 7: The James Webb Space Telescope during integration of the telescope into the Spacecraft Element (Gunn, 2019).

Subsystem	λ Range [μm]	Px Scale ["/px]	$\Delta\lambda/\lambda$
Imaging	5-28	0.11	3.5-16.1
4QPM Coronagraphic Imaging	10.65,11.4,15.5	0.11	14.1-17.2
Lyot Coronagraphic Imaging	23	0.11	4.1
Low Resolution Spectroscopy	5-12	0.11	100 @ 7.5μm
Medium Resolution Spectroscopy	4.9-28.8	0.196-0.273	1550-3300

Table 2: Summary of MIRI observing modes.

2.2 MIRI

The Mid-Infrared Instrument (MIRI) provides imaging, fixed slit and integrated field spectroscopy between 4.8 and 28 micron (G. S. Wright et al., 2015). These sub-instruments are enclosed in a closed-cycle cooler to maintain a temperature of 6.7 K in order to reduce the thermal background. At its most sensitive, MIRI is about 1000$\times$ more sensitive than comparable instrumentation on Spitzer. Sub-instrument sensitivities are shown in Fig. 8. While this will prove tremendously valuable for exoplanet science, it will also allow exploration of star formation, extra galactic astronomy and high-redshift observations. These and further science cases are described in (Rieke et al., 2015a). In its imaging mode, MIRI can operate with either a Lyot or 4-Quadrant-Phase-Mask coronagraph to reduce stellar glare, the MRS is not equipped with such an element. Thus its use for exoplanet observations is restricted to highly separated or bright targets. It may also be possible to use the differences between the host star and companion spectra in order to image close in planets.

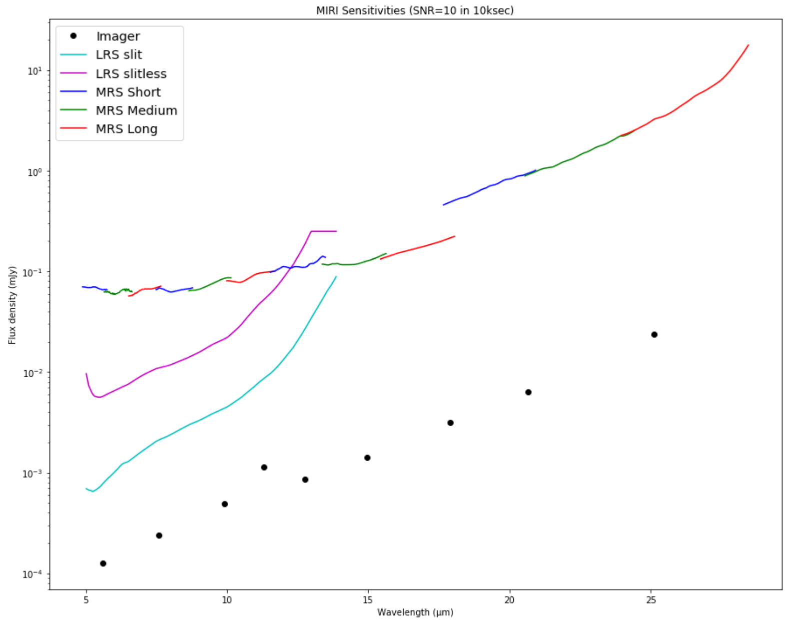

Figure 8: Sensitivities of MIRI sub-instruments for an SNR of 10, with a 10 000s integration (Rieke et al., 2015a).

2.3 THE MEDIUM RESOLUTION SPECTROGRAPH

The Medium Resolution Spectrograph (MRS) consists of four integrated field spectrographs projected onto two detectors, covering 4.8-28 micron with a spectral resolution varying from R=1700 to R=3500. Its FoV ranges from 4"×4" to 7.7"×7.7". While a full description of the MRS is given in (Wells et al., 2015), in this section we will outline the optical design of the instrument.

2.3.1 Coordinates

There are three primary coordinate systems in use with JWST/MIRI-MRS, of which two will be relevant for this thesis, with the detector and local MRS coordinates described in Fig. 9 (Argyriou et al., 2020).

The detector coordinate grid is formed by counting x/y pixels, as well as the slice number. Each of the two MRS detectors is an array of 1032×1024 pixels, though only 1024 are photosensitive in the horizontal direction. Each image slice from the IFU appears as a curved stripe on the detector, though neighboring stripes on the detector do not correspond to neighbouring slices of the image.

The local MRS coordinate system is described in terms of α, β and λ. The continuous α coordinate is the along slice direction, while β is perpendicular and discrete, corresponding to the slice number. λ is the wavelength. Both α and λ are fit by a second order polynomial to account for along and across slice distortion (Wells et al., 2015). Each detector sub array has its own mapping to α, β, λ space, due to the differences in FoV, slice count, distortion and spectral resolution.

Channel	Sub-band	Band	Detector	λ Range [μm]	FoV [as]	$\lambda/\Delta\lambda$
1	Short	1A	SW	4.83 - 5.82	3.46×3.72	3500
	Medium	1B		5.62 - 6.73	3.46×3.72	3500
	Long	1C		6.46 - 7.76	3.41×3.72	3300
2	Short	2A	SW	7.44 - 8.90	4.16×4.76	3000
	Medium	2B		8.61 - 10.28	4.16×4.76	3000
	Long	2C		9.94 - 11.87	4.12×4.76	3000
3	Short	3A	LW	11.47 - 13.67	6.00×6.24	2700
	Medium	3B		13.25 - 15.80	5.96×6.24	2300
	Long	3C		15.30 - 18.24	5.91×6.24	2300
4	Short	3A	LW	17.54 - 21.10	7.14×7.87	1700
	Medium	3B		20.44 - 24.72	7.06×7.06	1700
	Long	3C		23.84 - 28.82	6.99×7.87	1500

Table 3: Properties of the MIRI MRS channels (Wells et al., 2015).

The third coordinate frame is the global coordinate system of JWST itself, V1,V2,V3. The V1 coordinate refers to the symmetry axis of the telescope, V3 points towards the foldable secondary mirror support structure strut. V2 completes the coordinate system, being orthogonal to V1 and V3. This coordinate system will not be used in this thesis.

2.3.2 Integral Field Spectroscopy

As an integrated field spectrograph (IFS) consisting of 4 integrated field units (IFUs), the MRS provides both spatial and spectral information. This is accomplished by slicing the on sky image, and performing spectroscopy on each of the image slices. Here we will step step through some of the key optical systems used to accomplish this, while a more detailed description of the optics is given in section 2 of (Wells et al., 2015).

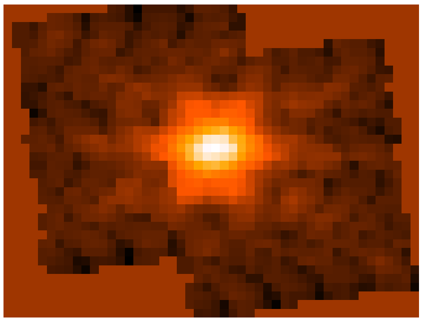

Figure 11: The reconstructed JWST PSF as imaged by the MRS, using a 2-pattern dither.

A series of optics picks off a FoV from the telescope beam, and directs it to the IFU slicing mirrors, where the focal plane is re-imaged. The image slicer consists of an array of thin mirrors at unique angles, in order to separate different spatial slices of the on-sky image. The across slice width is equal to the FWHM of the Airy pattern at the shortest wavelength of the given IFU. There are a total of 4 image slicers, one for each of the MRS channels. Each slice is then collimated, and directed to a diffraction grating. Each channel has 3 separate gratings, each covering approximately a third of the wavelength range of each channel. Thus it requires 3 total exposures to cover the wavelength range of a channel. Channels 1 and 2 are each projected onto separate halves of a single detector, as are channels 3 and 4 as seen in Fig. 10. When reconstructed, the PSF is an

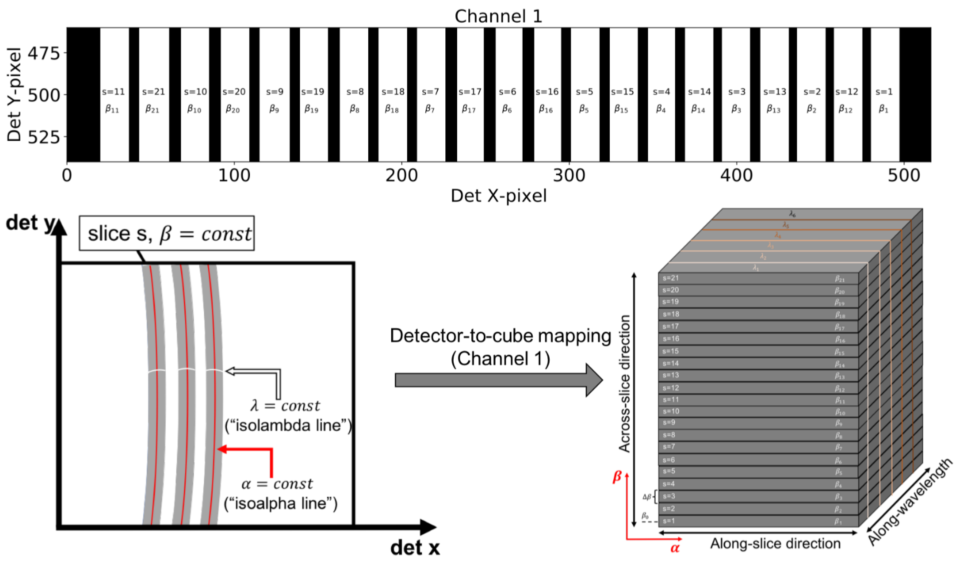

Figure 9: Description of the MRS detector (x,y,s) coordinate system to the local MRS (α, β, λ) cube coordinates. **Top**: Detector coordinates. Note that the consecutive stripe numbers s_i, s_{i+1} correspond to neighbouring image slices. **Bottom**: Description of the (invertible) detector-to-cube transformation (Argyriou et al., 2020).

undersampled image of the JWST PSF, though dithering can be used to improve the spatial sampling. As such, multiple wavelength ranges are imaged simultaneously, and it requires only 3 exposures in order to cover the entire MRS wavelength range.

2.3.3 Detectors

MIRI uses three arsenic-doped silicon (Si:As) impurity band conduction (IBC) detectors descended from those used in the Spitzer Space Telescope. Each detector uses a 1024×1024 pixel format. One detector is used for the imaging and LRS modes, while the remaining two detectors are used in the MRS. The full technical details of the detectors are described in (Rieke et al., 2015c).

Si:As IBC detectors are ideal for mid-infrared measurements. Each detector is built onto a high resistivity transparent contact. A 25-35 micron thick, heavily arsenic doped layer acts as the absorption layer, with an electric field maintained across the layer in order to transport the generated photoelectron. A transparent contact layer provides a connection to the detector electronics, where the signal is amplified and read out. A schematic of the layers in the detector is provided in the context of the fringing effect in Fig. 13. These detectors have a quantum efficiency that is wavelength dependent, and provides a fundamental limitation on the sensitivity. Precise measurement of this photon-to-electron conversion efficiency is critical for photometrically calibrating observations. The efficiencies are shown for each sub-band of the MRS detectors in Fig. 12.

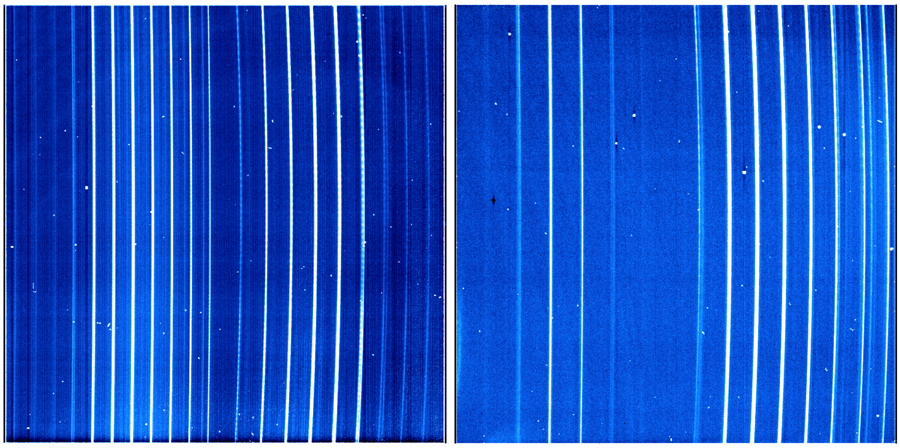

Figure 10: Raw detector images of the FM calibration source for channels 1 and 2 (left), channels 3 and 4 (right).

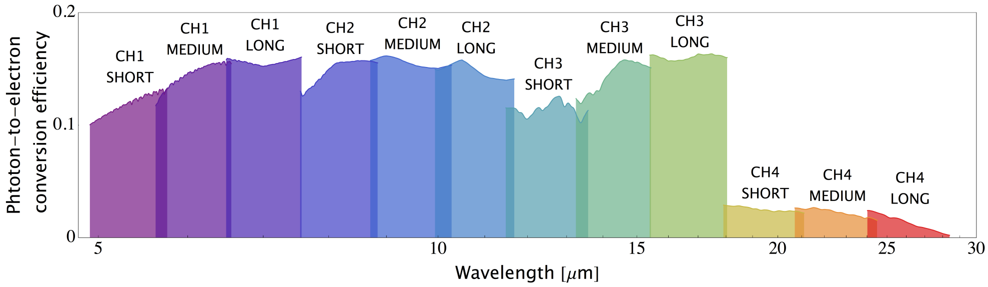

Figure 12: Average photon-to-electron conversion efficiencies for the MIRI MRS detectors.

Readout Modes

The MRS has two primary readout modes, which can be selected for different observing strategies.

- FAST - A 2.78 s integration with a single sample per pixel. Higher noise, but more suited for bright targets.
- SLOW - a 24 s integration, with 9 samples per pixel. A lower noise mode, but can saturate on bright sources.

2.4 OBSERVATIONS

The observations in this work are based on proposed exoplanet observations for the ERS and GTO programs. The observing parameters have been checked using the JWST Exposure Time Calculator in order to ensure sufficient SNR. Several of the observations make use of a dithering procedure, described below.

2.4.1 Dithering

The MIRI PSF is spatially undersampled in the MRS in order to allow for wider wavelength coverage and increased throughput. This design choice was made in order to reduce the weight of components that would be necessary in order to provide a fully sampled PSF while meeting the spectroscopic requirements. In order to fully sample the PSF, observations are dithered: that is, multiple telescope pointings are used, and the exposures from each pointing combined into a single observation. An optimal dithering strategy for each channel has been designed in order to fully sample the PSF in a minimum of observations. For a point source, it will be typical to use a 2 or 4 point dither pattern.

2.4.2 Exposure time calculations

The JWST Exposure time calculator (ETC) is a publicly available tool that can be used to estimate outcomes of a given set of observational parameters on a specified target. This can be used to estimate the SNR in different wavelength bands, optimize observing and check for detector saturation. All observations in this work were checked using the ETC in order to prevent saturation and ensure sufficient SNR. However, we did not attempt to optimize the observing strategy for our targets, and instead used the parameters specified in the ERS and GTO observing proposals.

3 FRINGING EFFECTS IN MIRI

Understanding optical and instrumental effects is critical for creating accurate simulated observations and for characterizing systematics. These systematics and uncertainties in turn impact the potential science results from any instrument by biasing measurements, reducing the signal to noise ratio of measurements or by injecting non-physical signals and correlations. The aim of this chapter is to examine fringing in the MIRI detectors and how this effect is modeled in the instrumental simulator (MIRISIM). We will examine the current status of fringe modeling and correction before discussing the modifications made to the MIRI instrumental simulator in order to model point-source fringing effects.

In order to quantify the effect of fringing on a spectrum, we examine the effect of fringing on a cross correlation between the extracted spectrum from the instrument and a known template. This provides a measure of the extent to which the signal has been degraded. In addition we examine the impact of this on the science case of molecular mapping, where cross correlations between a cube of IFU data and a molecular spectral template are used to identify the presence of a given species in an observed object.

3.1 FRINGING

Thin film interference occurs when light is coherently reflected at the internal boundaries between two layers and interferes with the incident light. This is the principle on which Fabry-Pérot interferometers function. As we wish to determine the effect of fringing on the amplitude of the signal received by the detector as a function of wavelength, we are effectively interested in the transmittance of a series of Fabry–Pérot interferometers. Assuming an ideal plane-parallel optical cavity with a reflectance R at both boundaries, thickness D, and an angle θ at which the light enters the cavity, we can compute the transmittance as:

$$T_c = \frac{1}{1 + \frac{4R}{(1-R)^2}\sin^2\left(\frac{\delta}{2}\right)} \tag{1}$$

Where the phase δ at half a wavelength ($\phi = \pi$), with wavenumber σ is:

$$\delta = 4\pi\sigma D\cos\theta - (\phi - \pi) \tag{2}$$

Systems with a spacing on the order of micrometers to millimeters produces significant interference for infrared light (Lahuis and Boogert, 2003).

The detectors of the MRS consist of several layers, as shown in Fig. 13, with a characteristic thickness of tens of micron, which results in significant (10%-30%) 'fringing' in a spectrally flat signal - visible in Fig. 10. The geometric thicknesses of the detector layers are given in table 4.

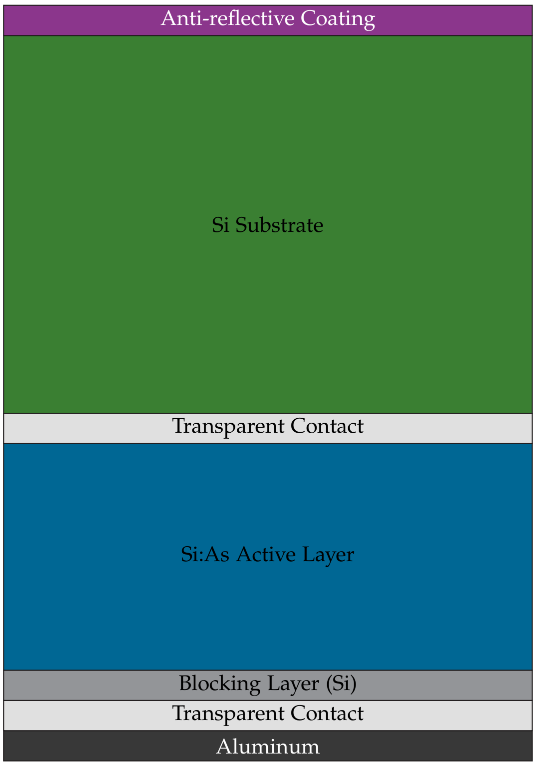

Figure 13: Layers of the MIRI MRS detectors. Note that thicknesses are not to scale (Rieke et al., 2015c).

While this is typical for infrared detectors such as those in the Spitzer Space Telescope (Lahuis and Boogert, 2003) or in the Space Telescope Imaging Spectrograph on board HST (Malumuth et al., 2003), the sensitivity and spectral resolution of the MRS increases the significance of this issue. The MIRI consortium has stated that the error budget for all detector effects must be 3.3% or less. Present fringing corrections result in a 5% deviation from a photometrically accurate signal, and can introduce correlated noise which will degrade any measured spectrum. Therefore it is critical to examine the impact of fringing on a signal, the parameters that influence the fringing strength and phase, and possible solutions for fringe correction. If all of the geometric and optical parameters were known, this would be sufficient to numerically solve for the fringing pattern within MIRI using eqn 1. Unfortunately, uncertainties in the thickness in the detector layers, variations in the layer deposition thickness, and the uncertainty of transmittance and reflectance of the materials used at cryogenic temperatures prevents the implementation of such a numerical model. Instead, we will turn to calibration data taken to empirically characterize the fringing pattern.

While a more complete treatment of proposed fringe correction can be found in (Argyriou et al., 2020) and (Fred Lahuis and Muller, 2018), this work will examine the implementation of fringing into the MIRI instrumental simulator and address the current state of fringe correction in the JWST Data Calibration Pipeline. We will discuss the architecture and usage of MIRISIM, along with the modifications we have made in order to model point-source fringing.

Layer	Material	Depth [μm]	Comments
Anti-Reflection Coating	ZnS	0.66	Optimized for λ = 6μm.
Substrate (raw wafer)	Si	460	Inactive layer.
Bottom Transparent contact	?	?	Not transparent, negative applied bias voltage.
Active layer	Si:As	35	Photoelectric absorption layer.
Blocking layer	Si	4	Inactive layer.
Top transparent contact	?	?	Not transparent. Positive applied bias voltage.
Pixel metalization	Al	semi-infinite	Forms metallized electrical contact with top transparent layer.

Table 4: Detector layer compositions and mean geometric thicknesses.

3.1.1 Current Status of Fringing Correction

Three test campaigns have been run in order to characterize MIRI: the Flight Model (FM) in 2008-09, the Cryogenic Vacuum (CV) in 2015-16, and the Optical Telescope element/ Integrated Science (OTIS) tests in 2017. Fringing was a major subject of both the FM and CV campaigns The first fringe model is fit to a spectrally flat, spatially extended source based on the FM test data. This is used to derive a 'fringe flat', and example of which is presented in 15. The extended source fringe flat is used both in MIRISIM to model the effect as well as in the JWST pipeline to correct for it.

This basic correction is insufficient to properly correct for fringing, and in the worst case can add additional fringing effects to the data. Therefore an additional iterative correction is used to attempt to remove fringing frequencies in Fourier space (Lahuis and Boogert, 2003; Fred Lahuis and Muller, 2018). Unfortunately, this can also remove real signals from the data. (Argyriou et al., 2020) proposes a novel method for fringe correction based on modeling sources as a collection of point sources, leading to a sum of overlapping point source fringe patterns. They show that this improves fringing correction to sub-percent levels, with mostly uncorrelated residuals.

Due to the dependence of fringing on the incident angle of the light, a single extended source model of fringing is insufficient to describe the full effect. In this work, we implement a more realistic fringing model based on point-source FM data and the concepts described in (Argyriou et al., 2018b). Data at various points across the detector is used to apply a unique position dependent fringe flat. We will quantify how this changes the extracted spectra after processing in the JWST pipeline, and examine to what extent present correction methods can remove the point-source fringing.

3.2 MIRISIM

The MIRI instrument has been simulated in python as a program known - perhaps unsurprisingly - as MIRISIM (Consortium, 2018). This program takes in an astronomical 'scene' along with some configuration parameters to output a detector data product, similar to what will be produced by the actual instrument. MIRISIM is relatively full-featured simulator, modeling the instrumental PSF, various noise sources and distortions, among other effects. While MIRISIM is functional for all of the MIRI sub-instruments, this report will only deal with the Medium-Resolution Spectrometer (MRS) sub instrument, described in section 2.3. The objective of this section is to describe the implementation and testing of an updated optical model of the 'fringing' effect - an optical effect caused by thin film interference from the multiple layers of the detector.

3.2.1 Architecture

While the full documentation for MIRISIM is available in (Consortium, 2018) and with python documentation in (Cossou, 2018), in this section we will outline the procedure for generating a simulated detector image. In particular, we will emphasize the parameter choices made in the setup for our simulations.

A MIRISIM simulation begins by setting up a **scene** using the `skysim`. This represents the view that the telescope will have of some astrophysical system. In general, a scene can be built from nearly anything: a fits file of an actual observation, models of galaxies and more. Built in are tools for producing simple point source and extended source objects. An SED of arbitrary spectral resolution is then attached to the object from an external file, with units of micron for the wavelength and μJy for the incident flux on the detector. There are also built in tools for blackbody SEDs, and individual lines of arbitrary position and depth. All of our SEDs are generated using petitRADTRANS from (P. Mollière et al., 2019), and attached as an external spectrum. Further details of the spectrum generation can be found in Chapter 4. A background can be applied, representing both astrophysical emission sources as well as thermal emission from the telescope itself. We chose not to include a background term, as background subtraction is using a simple model and image-from-image subtraction will result in an ideal correction.

For our observations, we only consider a single point source within the field of view. While this is an oversimplification, particularly in the case of close in planets, it is not the purpose of this thesis to explore the procedures for extracting a companion spectrum in a contrast limited regime. Instead, we assume that the spectral extraction will be adequate, though our simplification provides somewhat of a best case scenario.

The scene is then processed using a set of instrument and detector simulators `obssim`, `scasim` and `specsim`. These make use of the calibration data products (CDPs) in order to model optical distortions and detector effects. The output of this simulation is a set of uncalibrated data files, similar to what will be produced with on-sky observations. From the scene, an illumination model is produced. This transforms the on sky image using telescope and instrument optics in order to produce the intensity pattern incident on the detector itself. As our observations make use only of the MRS, they are then processed using `specsim`, which makes use of the `pySpecSim` module. This module is where most instrumental effects are applied, including detector sensitivities and fringing. These are applied by multiplying the illu-

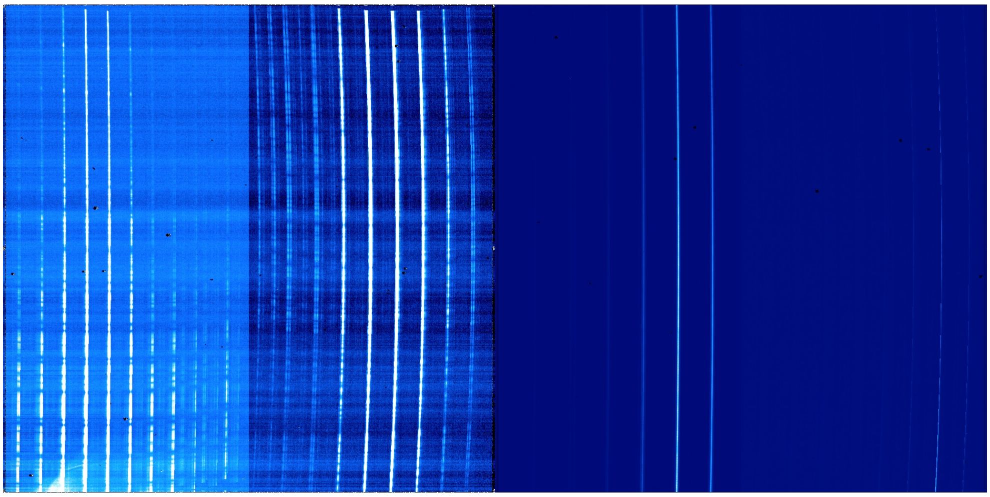

Figure 14: **Right Panel:** Channel 1 (left) and Channel 2 (right). **Left Panel:** Channels 3 (right) and 4 (left). Observation of WISE 0855 using the SHORT disperser. Fringing has been disabled for this particular observation. The color scale is in sqrt(DN) to highlight faint features.

mination model by the CDPs. The set of fringe CDPs covers each of the MRS sub-bands, and contains a fringe flat. This is a 2D array of multiplicative factors used to apply the fringe pattern to the illumination model, an example of which is given in Fig 15. Presently, these are derived from extended source CV data, CDP version 07.02.05. Once detector effects are applied, and the incident flux is converted into DN counts, a detector image is produced and stored in a fits file. A raw detector image for WISE 0855 is shown in Fig. 14

When running a simulation, the user must set the observation parameters. This includes setting the instrument used (MRS), dither pattern, readout mode, and further MRS parameters. Our parameter selections are based on the parameters used in the JWST ERS and GTO proposals for our target objects, described in more detail in 4.3 and summarized in table 6.

3.2.2 Data Products

All of the CDP files are derived from test campaign data, and represent the best empirical knowledge of the instrument. The primary CDPs of interest for this project are the photometric calibration data products and the fringe flats. The PHOTOM files map the sensitivity of each detector pixel in order to represent the varying sensitivity of the detectors with wavelength. They convert from an incident flux to detector counts based on measured efficiencies. Recently the PHOTOM files were modified from being divided into the illumination model to being multiplied in. This, along with other

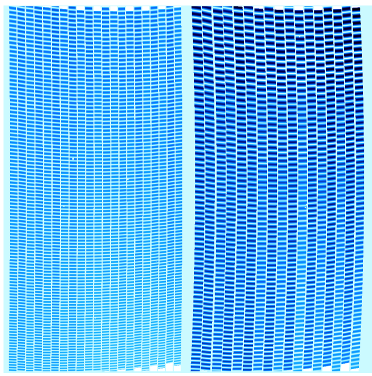

Figure 15: Fringe flat derived from FM data for the SW detector, in the SHORT sub-band v07.02.00. Color scale is linear.

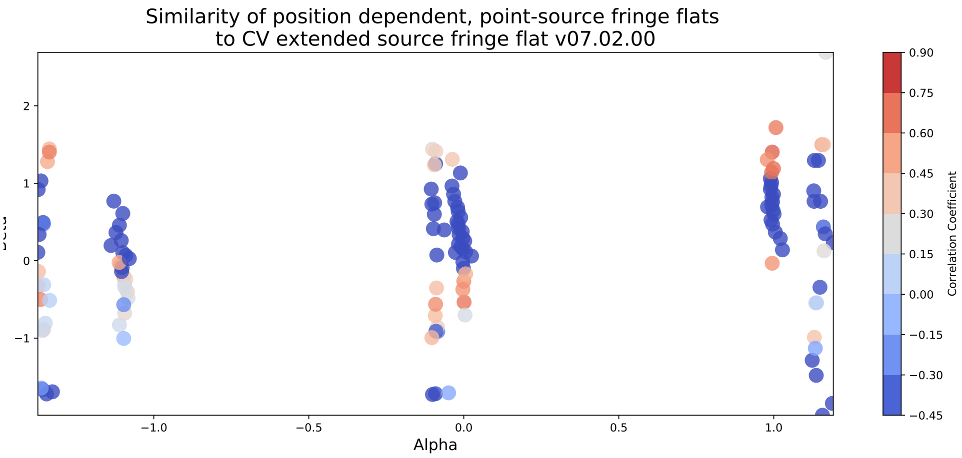

Figure 16: Spatial variation of the point source fringe flats as compared to the extended source model.

issues, has led to inconsistencies between the input flux and output of the JWST pipeline. To best correct for this, we ensure that we are using the most up-to-date PHOTOM files (v8B.04.00) in both MIRISIM and the JWST pipeline. Even still, there remains residual fringing and absorption features present in the PHOTOM CDP files, leading to errors in the extracted spectrum. Noteably there is a large spike in channel 2A, and significant high frequency modulation in channel 2C.

The FRINGE CDP files contain fringe flats which are multiplied into the illumination model. Presently, these are based off extended source CV data (v07.02.05). However, for point source observations this produces results very different than is measured (Argyriou et al., 2018b). Thus we attempt to improve the fringing model by using a set of fringe flats derived from point source FM data. In principle, a complete set of fringe flats that cover point sources located at each position in the detector plane would reproduce an extended source fringe flat. Indeed, at the center of the PSF, the extended source fringe flat models the point source fairly well, with discrepancies increasing towards the PSF wings (Argyriou et al., 2020). Due to this variation of the fringe pattern, there is a spatial variation in the similarity of the point source fringe flat as compared to the extended source, which we demonstrate in Fig. 16, where the correlation coefficients between each point source spectrum and the extended source spectrum are plotted In order to fairly compare our improvements, we will also compare to an older version of the fringe CDPs (v07.02.00) which is based on FM extended source data.

3.2.3 Fringing Model Implementation

Ultimately the data collection from the FM campaign produced a series of fringe flats of an almost point like at various position across the detector and in each channel. We implemented a new routine into the `pySpecSim` module of MIRISIM to read in the location of point sources within a scene, and apply the nearest available position dependent fringe flat.

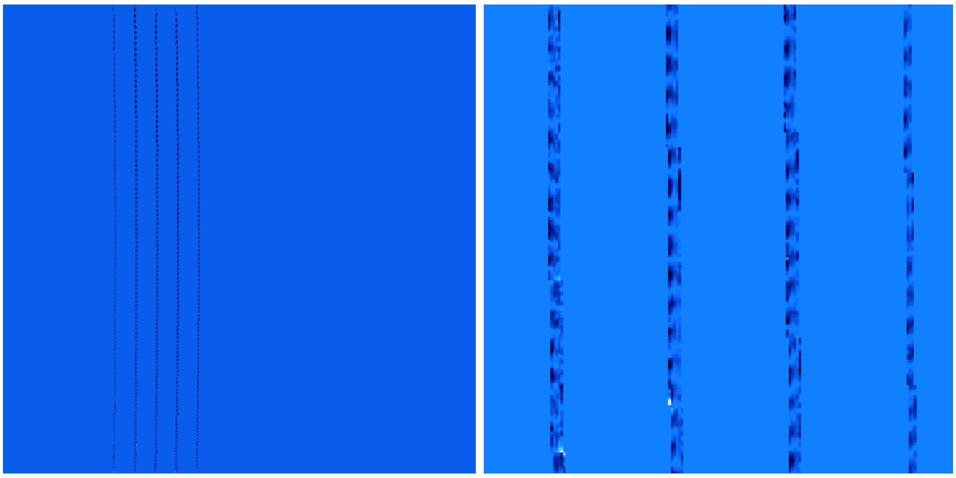

Figure 17: Fringe flat derived from FM data for a point source in channel 1A at $\alpha = 1.001$, $\beta = 0.602$. Color scale is linear, right is a closeup for detail.

Dithered observations are accounted for, with unique fringe flats being applied to each exposure. A new dithering strategy was designed, such that the locations of each exposure correspond to the locations of the nearest fringe flat to the standard dither offsets.

This implementation comes with several caveats: namely that the fringing model is not yet fully developed, so it can only be considered accurate for point sources located at the same (α, β) location as the source used to produce the fringe flat. Additionally, the source used to generate the data is not a true point source, nor are there fringe flats produced for the full MRS wavelength range. We stress that the goal of this testing is to demonstrate the significance of this effect to justify the need for a more complete model along with additional calibration data to constrain the detector layer parameters.

3.3 JWST PIPELINE

The JWST Pipeline is used for reducing all data from the telescope, and is currently under development by the Space Telescope Science Institute. The latest version of the pipeline (v0.15a) is used for all processing within this work (Bushouse et al., 2015). It is broken into several stages. Stage one is applied to all telescope data, and corrects for detector level effects. Stage two provides photometric calibration, with separate pipelines for imaging or spectroscopic data. Stage three, which is unusued in this work, will provide high level science products for end users.

3.3.1 Stage 1 Processing

The raw data files read from MIRISIM (or eventually the MIRI instrument itself) are a series of *exposures*, each made up of set of *integrations* containing a some number of *groups* or frames. Each group is a non-destructive read-out of the detector arrays, providing a series of increasing counts known as ramps in DN (digital number per second). The first stage of the JWST pipeline takes these raw files, applies a series of steps and outputs a single file for each input exposure in units of countrate. During this stage, several data quality checks are performed, looking for saturated pixels or jumps in in the data, which can be used to correct for cosmic rays. Dark current correction is also applied. Finally, the set of frames in an integration are fit with a linear slope in order to calculate the count rate in DN/s. This procedure is applied to all MIRI data. We used default pipeline settings to apply this procedure, and applied all steps applicable to the MIRI instrument. The particular calibration procedures for MIRI MRS data is described in (Labiano-Ortega et al., 2016).

Currently there are issues either in the production of uncalibrated data files in MIRISIM, or in the ramp step in the JWST pipeline. Unsaturated observations (according to ETC calculations) are treated as saturated, leading to incorrect slope calculations, particularly near the center of the PSF. This leads to a significant loss of flux in the final data products. In order to correct for this, we divide our input spectra by a factor of 10 to prevent any saturation, and multiply the final retrieved flux by the same factor.

3.3.2 Stage 2 Processing

For the second stage of processing we use the Stage 2 Spectroscopic Processing pipeline, and apply the steps individually to maintain control over parameters. The second stage pipeline applies instrument specific corrections that result in a photometrically calibrated exposure. For the MRS, this involves the following series of steps, some of which will be described in further detail below.

1. `assign_wcs` Assign a World Coordinate System (WCS) to each exposure.

2. `flat_field` Flatten photometric variation from differences in gain and dark current.

3. `srctype` Assign whether the target is a point or extended source based on input from the raw data files or observation parameters.

4. `straylight` Remove known stray light component.

5. `fringe` Divide by an extended source fringe flat.

6. `photom` Photometrically calibrate the exposure based on known pixel sensitivities and areas.

7. `cube_build` Transform from a (set of) 2D detector images to a 3D IFU cube in (α, β, λ).

Photometric Calibration

Photometric calibration is the process of removing detector and optical biases to ensure that the measured output corresponds to the true flux incident onto the telescope. This process occurs in the PHOTOM step of the JWST pipeline, and uses reference files which store per-pixel photon-to-electron conversion efficiencies along with pixel areas in arcsec to transform the count rate data product to a surface brightness measurement. This corrects for the wavelength dependent bias shown in Fig. 12.

However, this step remains under development, and does not produce absolutely calibrated images. In particular, even using the most up to date reference files (v8D.04.00) there remains discontinuities between channels, and poorly calibrated spectral slopes. In particular there remains a significant high frequency modulation in channel 2C, and a large spike in the flux in channel 2A. Fringing effects appear in most PHOTOM CDP files, adding an additional fringing component that is not removed during standard fringing correction. While we expect the photom files should not affect the output spectrum as they are simply multiplied in and divided out, these effects that are visible within the CDP files remain present in the extracted spectrum. This is a substantial limitation for spectral extraction, and must be rectified prior to analysis of on sky data.

Fringing correction

Fringing correction within the JWST pipeline is accomplished by dividing a known fringe flat into the photometrically calibrated detector image. This fringe flat is based of extended source CV data, and a unique flat is used for each detector/sub-band configuration.

Residual Fringe Correction

While not a part of the JWST pipeline, we also examined the use of Residual Fringe Correction (RFC) (Lahuis and Boogert, 2003; Fred Lahuis and Muller, 2018) to remove fringing from photometrically calibrated data products. This is an iterative procedure that fits 20 sinusoids of varying frequency and amplitude to each iso-alpha contour in order to detect and remove fringing patterns. We applied this procedure to on axis point-source fringe data in order to provide a comparison to using the standard fringe correction procedure using an extended source fringe flat.

Cube Building

In order to extract the spectrum measured by the MRS, the detector image is converted into an IFU Cube in (α, β, λ) space, using the transformation which was outlined in Fig. 9. A set of transformations for each band maps each detector pixel to a a spaxel in cube space, accounting for optical distortions. These transformations produce an irregular grid that samples the on-sky intensity, which can then be combined into a regularly spaced grid of spaxels. Each spaxel filled by a weighted sum of points, with the weight decreasing with distance from the spaxel. This should also account for changes in the MIRI PSF with wavelength, however issues with the cube building prevent use of the `miripsf` weighting scheme. Instead, the flux-conserving Shepards method is used, setting the weighting parameter to `'emsm'`. It should be noted that this procedure introduces correlations between the spaxels, which is not accounted in the error on each spaxel.

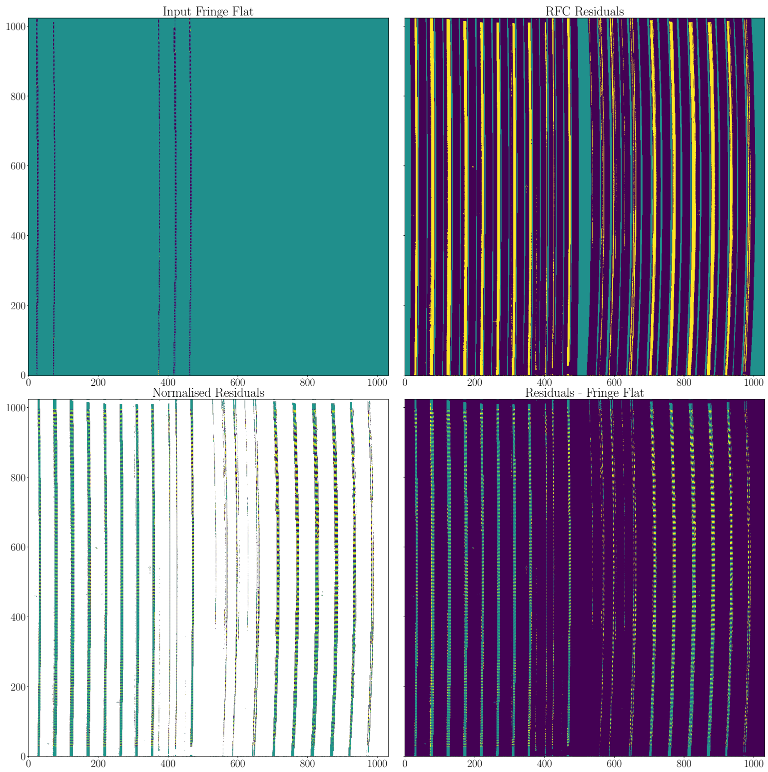

Figure 18: An example of the results produced using residual fringe correction. The top left shows the point source fringe flat applied to the data. The bottom left shows the residuals produced by the RFC, while the top left shows the same normalized to the range of the input fringe flat. The bottom right shows the result of subtracting the input fringe flat from the RFC residuals.

Aperture Photometry

Once the data from the pipeline has been transformed into a spectral cube, we can perform aperture photometry using the `photutils` package to extract a 1D spectrum of the source. For each frame in each sub-band the coordinates of the spaxel at with the peak flux is detected using `photutils find_peaks`, which provides the location for the center of a circular aperture. A radius of 5 spaxels is used to encompass the entire PSF for a point source. The input file must be photometrically calibrated, with units of surface brightness in mJy/as^2. Using the `aperture_photometry` function, we sum all of the contributions within the central aperture. Via a set of additional apertures, we measure and subtract the median background surface brightness. This measurement is then converted into flux units by multiplying by the spaxel area in as^2. The standard deviation of the background measurements is used to define the error on the flux measurement. In order to remove outliers, we consider a window of 40 points on either side of a measurement, and determine that any point that is greater than 7σ outside the median of this window to be an outlier. Outliers are set to the median value of the window, with the error on the point increased to 1/2 the value of the point. While optimal extraction techniques exist, given our known input signal and background, this procedure is adequate for producing a spectrum

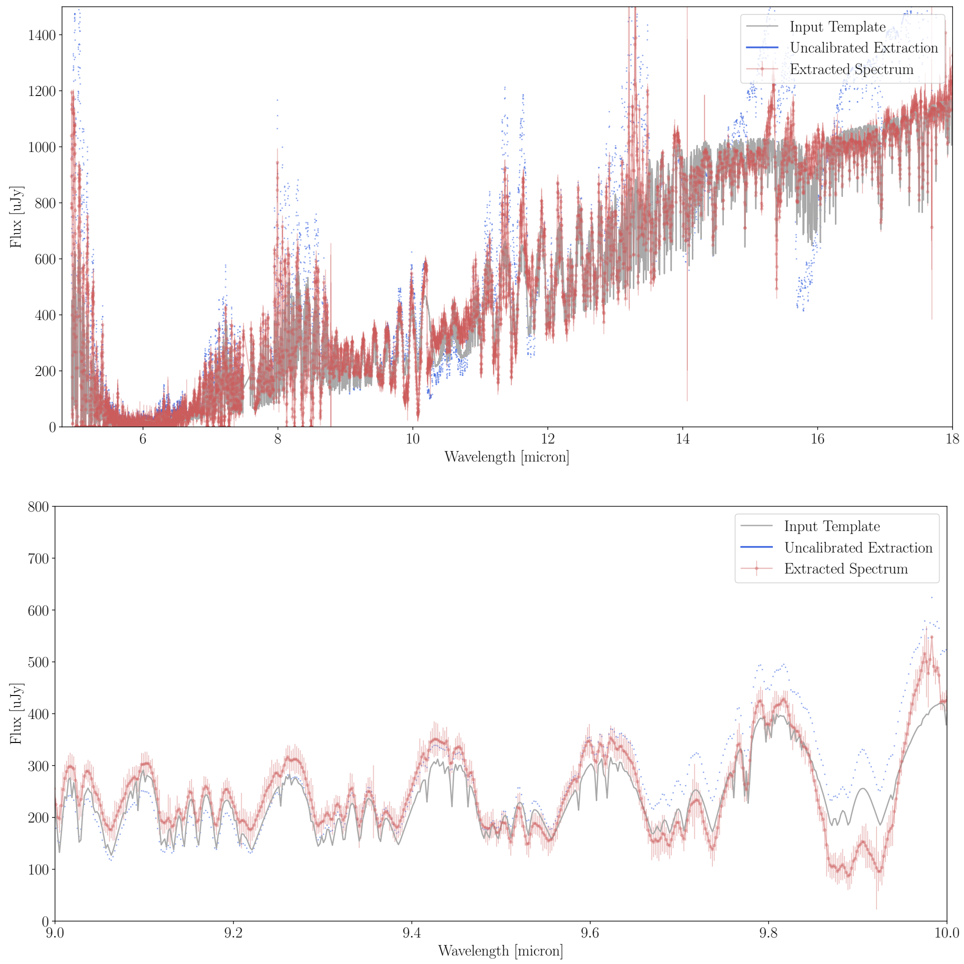

Figure 19: Top: Comparison of an input spectrum generated using petitRadTrans and the empirically calibrated output spectrum after extraction using aperture photometry from the cube produced by the JWST pipeline. **Bottom:** Close up around between 9-10μm to highlight small features.

in each sub-band, which can then be combined into a single spectrum for all measured sub-band.

Unfortunately, due to the issues described above with the PHOTOM step of the JWST pipeline, the spectrum built using aperture photometry does not accurately reflect the input spectrum in slope or absolute photometry. Therefore, we correct the extracted spectrum channel by channel. We fit a fifth order polynomial template spectrum and the extracted spectra. The fit to the extracted spectra is subtracted from the data, and the fit to the template is added. In order to justify this fit we consider the reduced chi square of the fit to the data: if the fit is not good ($\chi^2/\text{DoF} > 5$), we simply use a median filter to center the data around zero, before applying the fit to the template spectrum. This ensures that poor fits do not significantly alter the spectral shape. Thus this procedure corrects the slope and median flux value, but does not affect high frequency noise or signals. In practice, both curve fitting and median subtraction produce similar results, but it is important to note that this procedure cannot be applied to real data where the ground truth is not known, but is only a method used to correct for current issues with the simulation and data reduction software. Fig. 19 shows an example of the results of this procedure. We believe that this is a justified measure, as the errors with photometric calibration in the pipeline should be resolved before first light of the telescope.

3.4 CROSS-CORRELATION

To quantify the similarity of the spectrum output by the JWST pipeline to the input into MIRISIM, we rely on the technique of cross correlation. Originally used in a spectroscopic context by (Simkin, 1974) in order to compute galaxy velocity dispersions, cross correlations have become a popular technique used to quantify exoplanet parameters (Ignas Snellen et al., 2014).

For two arbitrary, complex-valued functions $f(t)$ and $g(t)$, we can compute the cross correlation as as function of the shift τ between the functions (typically in time or velocity space):

$$(f \star g)(\tau) \equiv \int_{-\infty}^{\infty} f^*(t) g(t+\tau) dt \tag{3}$$

Our signals of interest are astrophysical spectra, measured in a finite number of discrete wavelength bins. For such a signal with M bins:

$$(f \star g)[n] \equiv \sum_{m=0}^{M} f^*[m] g[m+n] \tag{4}$$

Care must be taken when cross-correlating signals, as differences in normalization can result in changes in the correlation coefficient. Our procedure takes in two spectra. The first is an emission spectrum produced by the petitRADTRANS program (P. Mollière et al., 2019), which provides our forward model with which we compare our data spectrum. Our data is the result of passing the template spectrum through MIRISIM, and extracting it from the resulting detector image using the JWST pipeline. We then rebin the high-resolution input spectrum to the same wavelength bins as the data spectrum, using the `spectres` package (Carnall, 2017). Prior to normalization, we remove any outliers from the spectrum (due to binning errors or instrumental effects) by setting any data points separater by more than 15 standard deviations from the mean to the median value of the spectrum. For each spectrum, we subtract the minimum value to remove any offset in the spectrum, and divide by the maximum value to restrict the range to [0,1]. We then use apply a Savitzky-Golay filter with a window of 1/4 the length of the spectrum and a polynomial order of 3, which we then subtract from the unfiltered spectrum. This removes the continuum emission from the spectrum, and centers it around 0. We then renormalize the spectrum by dividing by the maximum absolute value such that the range is in [-1,1]. This procedure removes the continuum which would introduce an overall slope to the cross correlation, but preserves the relative line depths and positions.

The cross correlation between the forward model and itself is computed, excluding the region of interest around 0 offset. This 'autocorrelation' is subtracted from the cross correlation between the forward model and the data spectrum in order to remove secondary peaks. Finally, we normalize the cross correlation by the standard deviation of the cross correlation (excluding the central peak), giving an output measured as a signal to noise ratio.

3.4.1 Residual Statistics

In addition to computing the cross correlation between the forward model and the data spectrum, we also examine the residuals between the two spectra. Here we can see any unexpected variations between the two (periodic signals, offsets or other features). We can also examine a histogram of the residuals, normalized by the standard deviation of the data spectrum. This provides us with a distribution which should have a mean of 0 and unit width if the data are unbiased and share a distribution with the true input spectrum.

3.4.2 Molecular Mapping

Cross correlations are used to identify the presence of a given molecular species in the spectrum of an atmosphere (Haffert et al., 2019; Hoeijmakers et al., 2018). By extending our iterating over each spaxel from the MRS cube and using a molecular template rather than the input spectrum, we can examine the impact of fringing on such an analysis.

We use petitRADTRANS to generate a single-species atmosphere in order to generate the molecular emission spectrum templates. We chose to use VHS1256b as our template for this study, and all other atmospheric parameters remain the same, as described in table 5. A fractional abundance of 1% was used for each species. The emission spectrum for each of these species is shown in Fig. 20. Using the same normalization procedure described in section 3.4 for each spaxel, we take the peak cross correlation value from within a narrow window around the expected peak at 0 offset between the template and measured spectra. This was repeated for each of the fringing cases and each of the molecular templates. We also compare the cross correlation as computed sub-band by sub-band to the full wavelength range used.

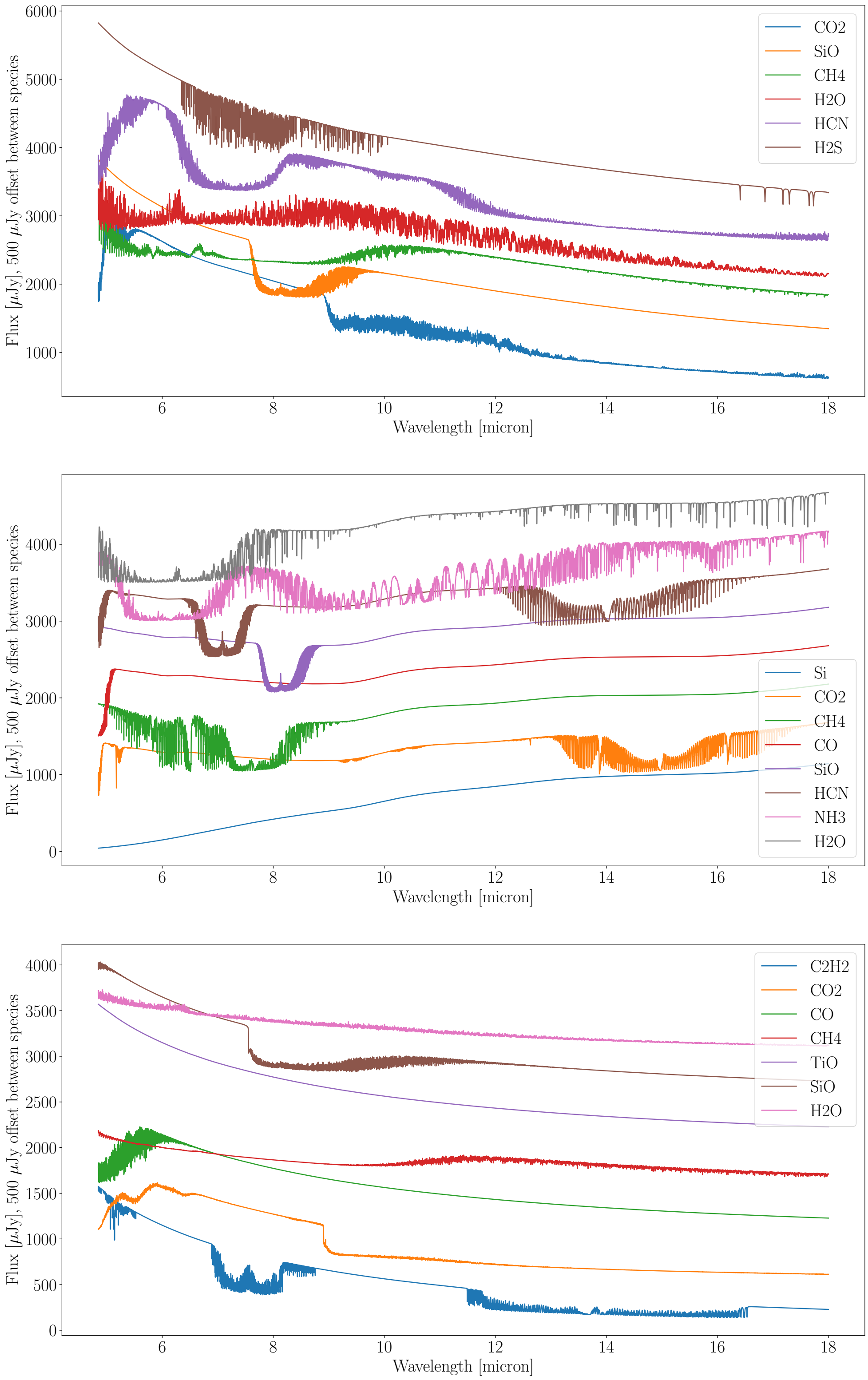

Figure 20: **Top:** Species templates for VHS1256b. Each species emission spectrum is computed using petitRADTRANS with a single species atmosphere with Jupiter-like abundances of H_2 and He, and an internal temperature of 900 K. There is a 500μJy offset between each species. **Center:** The same, but using WISE 0855 parameters. **Bottom:** The same for 2M1207b.

3.5 RESULTS

We examined the cross correlation between the input template and the extracted spectrum for each of our three targets across 5 cases:

1. No fringing applied in MIRISIM, no Correction
2. Extended source fringing, Corrected with an extended source fringe flat
3. On axis point source fringing, corrected with an extended source fringe flat
4. On axis point source fringing, corrected using residual fringing correction for each iso-alpha contour
5. Off axis point source fringing, corrected using an extended source fringe flat.

In addition, we compare the extracted spectrum to a set of molecular templates computed in petitRADTRANS, using the atmospheric parameters for each target, but only a single species other than hydrogen and helium at a 1% abundance.

Here we take VHS1256b as our template for analysis. Fig. 21 shows the results of cross correlating the extracted spectra with the input template spectrum for channel 1 of the MRS. Point source fringe flats are only available for channel 1, hence we restrict our analysis of the fringing variation to this channel alone. We show the spectrum normalized to the range [-1,1], along with the residuals from subtracting the extracted spectrum from the template. Note the fringing present in the residuals of the spectrum with point source fringing: dividing by an extended source fringe flat does not properly correct for point source fringing. While the residual fringe correction (RFC) does not have structure apparent, it also removes nearly any signal originally present, and dramatically alters the shape of the spectrum By examining the distribution of the residuals, we can also see that the widths of residuals varies, with RFC producing the widest distribution. Importantly, this corresponds directly to the reduction in SNR of the cross correlation, as shown in the bottom plot.

The cases with no fringing and with an extended source corrected by an extended source fringe flat show nearly identical SNRs of 22.3. The point source fringing corrected by an extended source fringe flat fares slightly worse, with an SNR of 20.9. If the point source is off axis, and thus has a different fringe pattern, the SNR worsens to 18.6. Finally, the RFC applied to point source fringing substantially degrades the signal, leaving an SNR of 4.3. These results are similar for each of our targets. Fig. 22 shows the cross correlation results for each target and each examined fringing case.

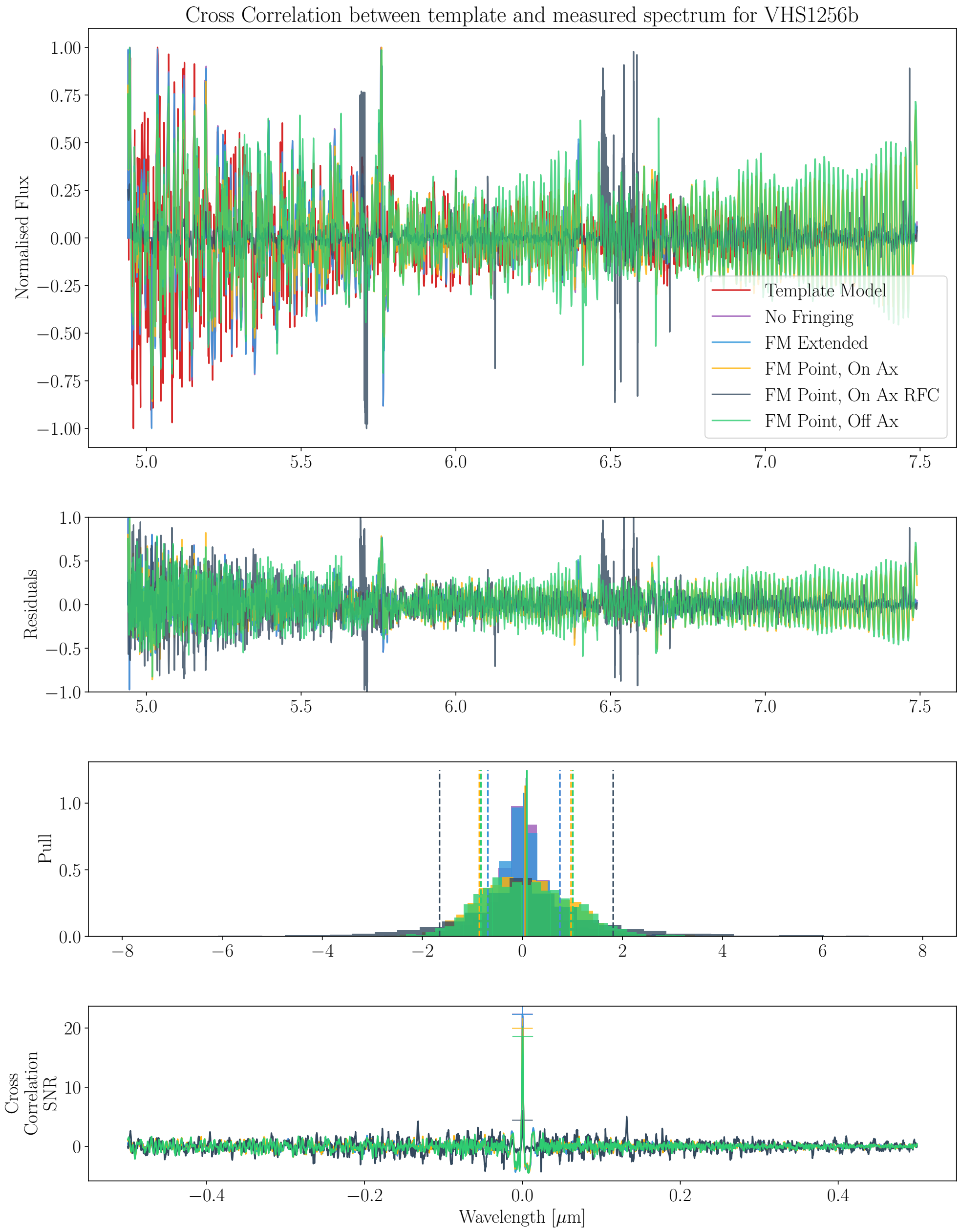

Figure 21: **A** Normalized CH1 spectra of VHS1256b. **B** Residuals found from subtracting the extracted spectra from the input template. **C** Histogram of residuals. Note the difference in the distribution widths due to fringing. **D** Cross correlation between the extracted spectra and the template.

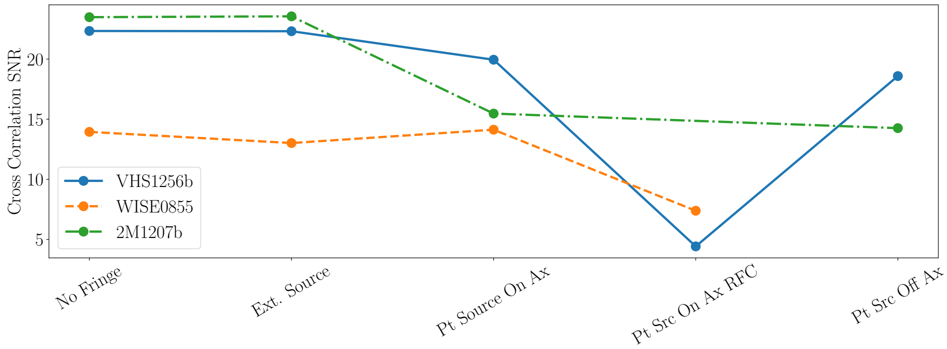

Figure 22: CH1 Cross correlation SNRs for each target and each fringing case. Cross correlations are between the input template and the extracted spectrum.

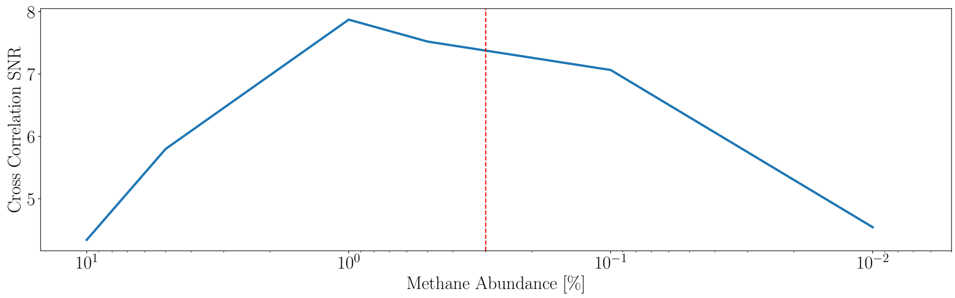

Figure 23: Dependence of the cross correlation on the abundance of a methane in the VHS 1256b species template. The true abundance in the full atmosphere is marked with the red dashed line.

3.5.1 Molecular Mapping

Species Detection

In order to best identify any molecular species present in the atmosphere, we cross correlate the 1D spectrum extracted through aperture photometry with the molecular templates in order to maximize the available flux. Following the procedure for cross correlating the extracted spectra with the full input template, we show the results of cross correlating the extracted channel 1 spectra with the molecular templates in Fig. 24 for VHS1256b. The SNR values reasonably trace the input abundances of each species. Notably though, methane is detected as less abundant than water: this may be due to the location of the methane lines around 10μm, where the spectral extraction is poor due to errors within the PHOTOM files in MIRISIM. As visible in Fig 20, the relative line depths at a 1% abundance are deeper for water than for methane, which could also lead to a more significant cross correlation. We examined the dependence of the cross correlation on the abundance of a given species by varying the abundance of methane from 0.1% to 10%, shown in Fig. 23. We see that within an order of magnitude of the true value, the cross correlation is relatively constant, but drops off at significantly higher or lower concentrations.

Another feature seen in Fig. 24 is the variation in the SNR due to the different fringe correction methods. Although below the 5σ detection threshold,

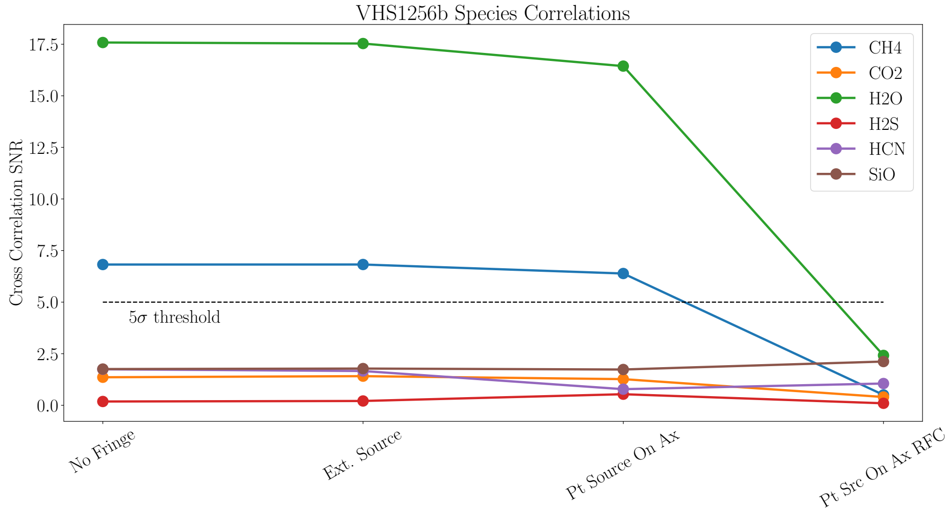

Figure 24: Channel 1 Cross correlations for each molecular species against the extracted spectra for VHS1256b. The input abundances of each species are given in table 7.

we observe that the SNR of the H_2S cross correlation increases when using the extended source fringe flat to correct the point source fringe, although H_2S is only negligibly present in the atmosphere (at an abundance of 10^{-10}). This presents challenges in determining whether a species detected is a true detection or a false positive due to poor corrections.

Fig.25 shows similar results for 2M1207b. Here we also compare the variation in cross correlation when using the full spectrum as compared to channel 1 only. For VHS1256b, the cross correlation SNR does not significantly depend on the wavelength coverage of the spectrum. Fig. 25 shows the effect of using the full wavelength regime. For CO, the increase in coverage results in a shift from a marginal to a strong detection. Note that this comparison is limited, as point source fringing is only available for channel 1, and the remainder of the spectrum uses extended source fringing. We observe significant decreases in SNR when point source fringing is used. The SNR for water is reduced by half, while CO drops below the 5σ detection threshold. This demonstrates the necessity of improved fringe correction if detections of even relatively abundant species are to be made. We also note that in some cases, the normalization procedure actually results in a higher SNR when only a single channel is used. It is important to examine specific wavelength regions of interest for each species such that important features are highlighted.

Object Detection

In addition to detecting the presence of a given species in a known planet, we can use molecular templates to identify the presence of an object. In practice, this would involve iterating through a grid of single species spectral templates, and cross-correlating with each spaxel in the IFU cube. We aim to demonstrate that this technique is effective for MRS data, and that fringing reduces the capability to make detections.

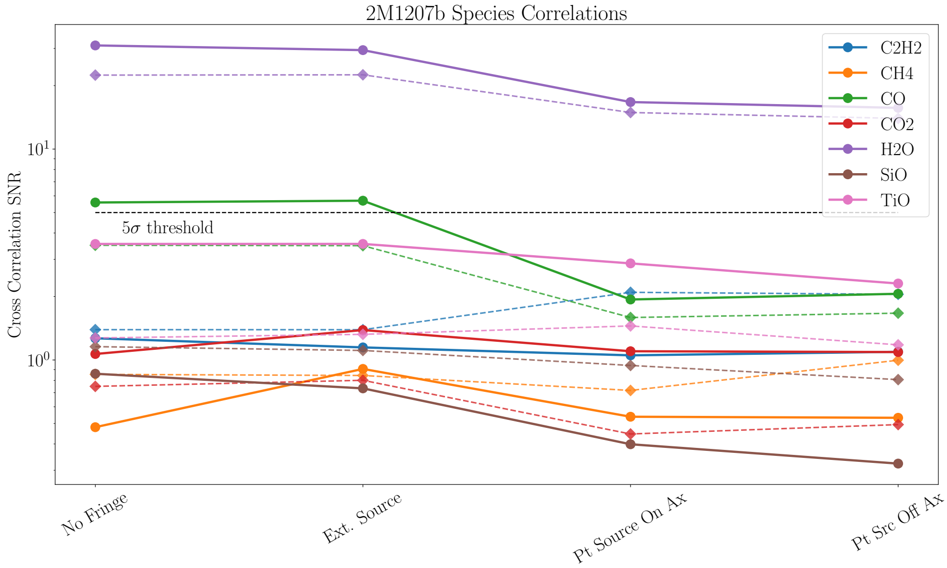

Figure 25: Cross correlations for each molecular species against the extracted spectra for 2M1207b. Solid lines indicate the full wavelength range was used, while dashed lines are for channel 1 only.

Fig. 26 illustrates the ability of the MRS to identify a point source from the presence of a species in the atmosphere. The cross correlation was performed on a spectrum from each spatial location in the IFU cube with a single species atmospheric template, with similar parameters as used in the full atmospheric model. This extends the 1D cross correlation used to infer the presence of a species to the full spatial coverage of the MRS. However, note that this the spectrum extracted from the data does NOT have the same corrections applied as in the 1D case, but is rather the raw data in MJy/sr. As noted in the section on aperture photometry, these spectra depart significantly from the input templates, and are not yet reliable. Following continuum subtraction and normalization, a cross-correlation should still provide a robust metric of similarity in the case that the relative line depths and positions are well represented by the spectrum.

We compare highly abundant species on the left, to species with low or no presence on the right for each of our targets, in the case that there is no fringing. For highly abundant targets, the cross correlation traces the JWST PSF. The peak value of the SNR in 2D is not expected to be equal to the SNR of the 1D cross correlation, which contains significantly more flux than in any individual spaxel. The peak SNR does not trace the abundance distribution of the input atmosphere. For WISE0855, H_2O has a much higher SNR than NH_3 (20 vs 4), though the underlying abundance is lower (10^{-4} vs 10^{-3}). Although CO has an extremely low abundance in WISE0855 (10^{-15}), the cross correlation produces a high SNR of 8. This suggests that the cross correlation is likely tracing the magnitude of the PSF, rather than the presence of the species itself. We therefore caution the use of cross correlations to infer the presence of a planet, as false positives are both likely and difficult to quantify. Without proper photometric calibration, the 2D cross correlations remain unreliable, and further work is required to reduce false detections.

3.5.2 Discussion

We have examined different fringing correction methods, and compared a realistic point-source fringing model to the simplified extended source model used in MIRISIM. We find that the point source fringing significantly reduces the SNR in a cross correlation. Apart from marginal detections, this will likely not be the limiting factor in determining the presence of a given species. Residual fringing correction as used in the Spitzer Space Telescope cannot be directly applied to MIRI MRS spectra. This procedure significantly removes real features from the spectra, leading to non-detections of species known to be present.

Ultimately this analysis is limited by the development status of both MIRISIM and the JWST pipeline. Calibration is an ongoing process, and the CDP files available as of March 2020 still leave significant residual effects present in the extracted spectrum. Photometric calibration must be done in an empirical, ad hoc fashion that cannot be applied to real data without ground truth photometry. Until these issues are resolved, spectral extraction of real data using the MRS will be extremely limited.

Cross correlations provide a useful tool for quantifying the similarity of two spectra, identifying the presence of molecular species and identifying variation between different data processing methods. However, a cross correlation does not retrieve an actual abundance. For that we must use an atmospheric retrieval, as described in Chapter 4. This does provide a useful tool for guiding which species should be included as free parameters in an retrieval, as well as for identifying the presence of a companion given the variation in the spectra between the host star and the companion.

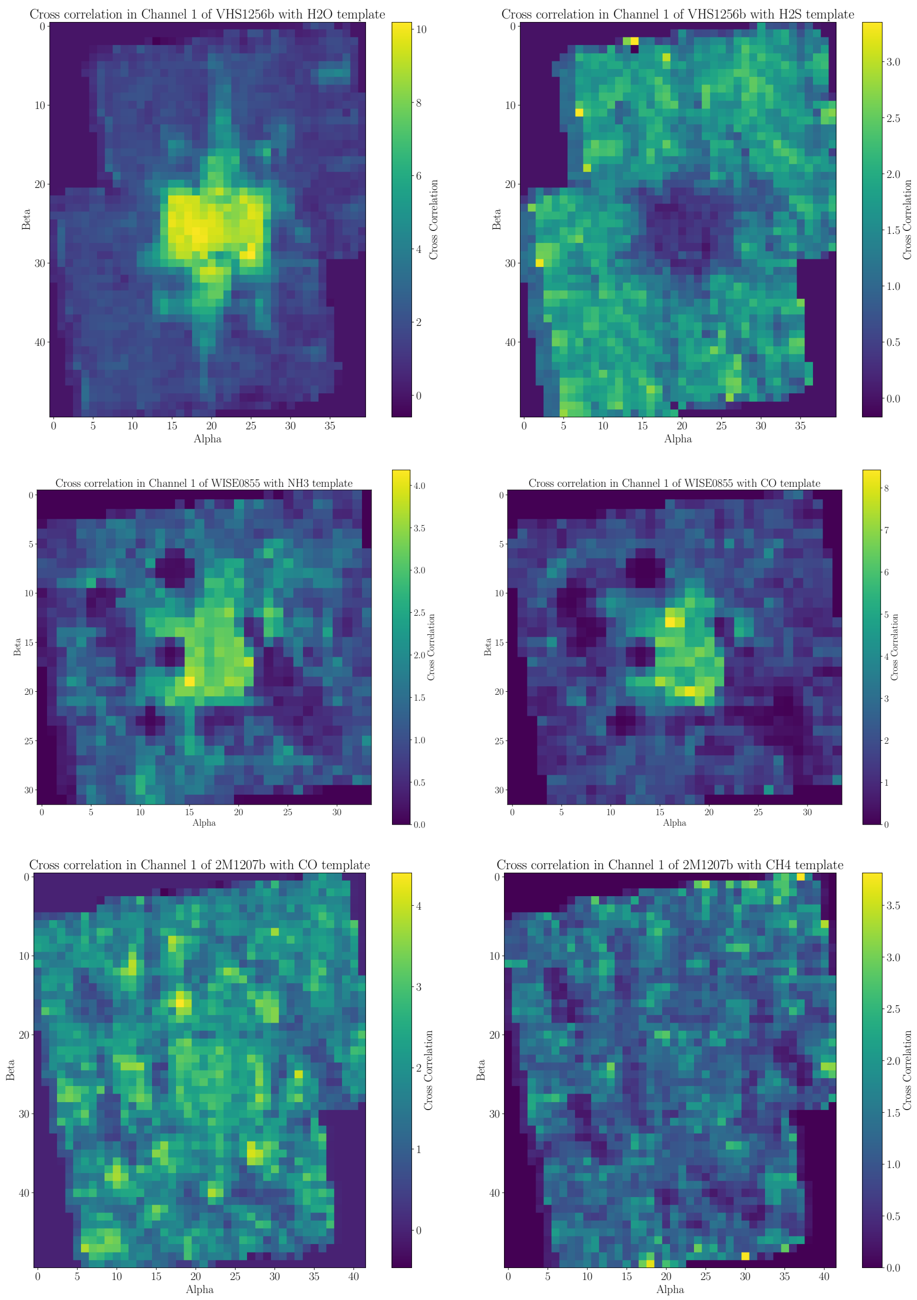

Figure 26: Cross correlations for each of the targets with a selection of molecular templates, with extended source fringe. Scales are not the same for each image. **TOP:** VHS1256b with H_2O (right) and H_2S (left). **Center** WISE0855 with NH_3 (left) and CO (right). **Bottom:** 2M1207b with CO (right) and CH_4 (left).

4 ATMOSPHERIC RETRIEVALS

Everything photon of light that we receive from an exoplanet will interact with its atmosphere, and will therefore provide us with a hint of what that atmosphere may look like. An atmospheric retrieval is the process of reconstructing the atmosphere of an object based on an observed spectrum. This process relies heavily on having accurate models which can be parameterized by the physical quantities we are interested in: generally the temperature, pressure and composition (Nikku Madhusudhan, 2018). As these models cover a very large parameter space (>10 parameters, each covering several orders of magnitude), it is necessary to have an efficient method for sampling this space, computing a model and comparing this model to the data (Bjoern Benneke and Sara Seager, 2012; Björn Benneke, 2013). Currently, atmospheric retrieval methods have been used for both exoplanets and brown dwarfs to identify water, methane, CO, CO_2 and other species (Barman et al., 2015; Konopacky et al., 2013), along with clouds being a universal feature (Michael R. Line et al., 2017; Morley et al., 2018; Schlawin et al., 2018)

This chapter will outline the process of an atmospheric retrieval from modeling to marginalization of posteriors, and will examine the impact that the instrumental effects described in Chapter 3 have on the retrieved parameters. Additionally, this will provide an example of how the MIRI MRS can be used to explore exoplanet and brown dwarf atmospheres, and what observational parameters should be considered when studying these objects, following similar studies from (Batalha et al., 2018; Schlawin et al., 2018) for NIRSpec and LRS observations and (Feng et al., 2018) for future reflected light missions.

Atmospheric Modeling

Atmospheric modeling is the task of creating an spectra based on the physical properties of the atmosphere. This is a broad task that can range from a 3D Global Circulation Model (GCM) which accounts for self-consistent atmospheric chemistry (Chen et al., 2019) to a 1D model based around an empirical temperature-pressure profile (P. Mollière et al., 2019). The choice of model depends largely on the requirements for accuracy and computational cost. Considering the potentially millions of possible atmospheres that must be examined in a retrieval problem, whatever model is used must be computationally efficient while still maintaining a close approximation of reality.

Property	Description
Temperature	Parameterized, e.g. (Guillot, 2010)
Abundances	Parameterized, e.g. vertically constant
Scattering	Cloud scattering, transmission spectra only
Clouds	Power law and condensation clouds
Cloud particle size	f_{SED} and K_{ZZ} or parameterized
Particle size distribution	log-normal, variable width
Cloud abundance	Parameterized
Wavelength spacing	R=1000 (c-k), 10^6 (lbl)
Valid emission spectra	Clear, from NIR and longer

Table 5: Description of the parameters available in petitRADTRANS. For cloud particles, f_{SED} is the mass-averaged ratio of the cloud particle settling speed and mixing velocity. K_{ZZ} is the atmospheric eddy diffusion coefficient (Ackerman and Mark S. Marley, 2001)

4.1 PETITRADTRANS

For this work we chose to use the petitRADTRANS package due to its user-friendly python implementation, high speed computation for retrieval use and extensive high resolution, line-by-line spectral library for generating planetary spectra (P. Mollière et al., 2019). It is a 1D, radiative transfer package with many parameters options, described in table 5 PetitRADTRANS can compute both emission and transmission spectra, with an output spectral resolution of R=1000 in correlated k mode, or R=1 000 000 in line-by-line mode.

Note that much of the following sections applies to many other similar 1D radiative transfer atmospheric modelling programs such as ATMO (Goyal et al., 2019), Planetary Spectrum Generator (Villanueva et al., 2018), HELIOS (Malik et al., 2017, 2019) and others. Many (or even most) of these programs rely on the same set of high-resolution molecular line lists, including HITRAN/HITEMP (Gordon et al., 2017; Rothman, 1981; Rothman et al., 2010), ExoMol/ExoCross (Tennyson and Yurchenko, 2017; Tennyson et al., 2016; Yurchenko et al., 2018) and others.

4.1.1 Radiative Transfer

In order to compute the emission spectrum an initial featureless blackbody spectrum $B(T_{int})$ is passed through multiple discrete layers of the atmosphere, parameterized by their temperature, pressure, and the opacities of each of the species present in a given layer. Modeling each layer as plane parallel, the intensity is computed as in (P. G. Irwin et al., 2008; P. Mollière et al., 2017, 2019)

$$I_{top} = B(T_{int})\mathcal{T}^{atmo} + \frac{1}{2}\sum_{i=0}^{N_L-1}\left[B(T^i) + B(T^{i+1})\right]\left(\mathcal{T}^i - \mathcal{T}^{i+1}\right) \tag{5}$$

N_L is the number of layers in the atmosphere, and $\mathcal{T}$ is the transmission from a given layer to the top of the atmosphere. All quantities are averaged per wavelength bin in c-k mode, while they are evaluated at each wavelength point in line-by-line mode.

In order to compute the temperature structure of the atmosphere, a modified Guillot model (Guillot, 2010) was used, as used in (P. Mollière et al., 2017, 2019). The temperature structure is defined as

$$T(P) = \left\langle T_{Guillot}(P)\left(1 - \frac{\alpha}{1+P/P_{trans}}\right)\right\rangle_P . \tag{6}$$

As denoted by $\langle\rangle_P$, this profile is boxcar-smoothed over log(P), with bin widths of 1.25 dex (P. Mollière et al., 2019). The modified Guillot profile is defined as

$$T_{Guillot}(P) = \frac{3T_{int}^4}{4}\left(\frac{2}{3} + \delta P\right) \tag{7}$$

$$+ \frac{3T_{eq}^4}{4}\left[\frac{2}{3} + \frac{1}{\gamma\sqrt{3}} + \left(\frac{\gamma}{\sqrt{3}} - \frac{1}{\gamma\sqrt{3}}\right)e^{-\gamma\delta\sqrt{3}P}\right] \tag{8}$$

with the second term accounting for irradiation of the upper atmosphere. The opacity parameters $\delta = \kappa_{IR}/g$ and $\gamma = \kappa_V/\kappa_{IR}$ are defined such that the optical depth $\tau = \delta \cdot P$. T_{int} is the internal temperature of the planet, and is equivalent to the effective temperature of the planet, that is the temperature of a blackbody with the same luminosity as itself. T_{eq} is the equilibrium temperature of the planet, based on the temperature of the host star and separation of the planet. For an isolated, free floating object this temperature goes to 0. The remaining free parameters α, P_{trans} simply modify the shape of the temperature structure according to the pressure.

4.1.2 Opacity Sources

To compute the emission spectra of an atmosphere, petitRADTRANS accounts for various opacity contributions including absorption and emission lines, collisionally induced absorption, cloud opacity and scattering and Rayleigh scattering cross sections. These sources are described in detail in (P. Mollière et al., 2019), summarized in tables 2 and 3. For this work we consider only the case of a cloud-free atmosphere due to the complexity of realistic cloud modeling.

Line-by-line

In its high resolution line-by-line mode, petitRADTRANS computes emission spectra with R=10^6. These spectra are computed using opacity sources for molecular and atomic lines from ExoMol/ExoCross library (Yurchenko et al., 2018). Pressure broadening is taken into account using the coefficients from HITRAN/HITEMP (Rothman et al., 2010, 2013) or from (**Sharp2007**) (Eqn. 15). The line opacities are computed from 80-3000K, and from 0.3-28μm in high resolution mode.

Correlated K

The low resolution mode of petitRADTRANS uses the correlated-k (c-k) method of computing line opacities (Fu and Liou, 1992; Goody et al., 1989;

Lacis and Oinas, 1991). This method for calculating emission and absorption features assumes that the opacity distribution functions between differing species are uncorrelated, which permits simple computation of overlapping features. While petitRADTRANS implements a c-k method with a spectral resolution of 1000, in principle it is accurate to much higher resolutions. However, the principle utility of the c-k method is in the dramatic reduction in computational cost for computing a spectra such that petitRADTRANS can be used as the foundation for an atmospheric retrieval code requiring hundreds of thousands or millions of models to be generated. (P. Mollière et al., 2019) discusses the variations between the results of the line-by-line method and the c-k method, finding discrepancy of at most 6%. Typical variation is much lower, as seen in Fig. 2 of (P. Mollière et al., 2019).

Clouds

While clouds are a seemingly universal feature in exoplanets and brown dwarfs (Jacqueline K Faherty et al., 2018; Michael R. Line and Parmentier, 2016; Morley et al., 2014), they remain a difficult problem for retrieval studies. Clouds form when a species condenses out of the gas phase, typically around a small nucleus. This creates a layer of particles at a reasonably well defined altitude in the atmosphere, and prevents the observation of deeper atmospheric layers. While a simple model of clouds may be a 'gray' cloud deck that acts uniformly across wavelength, a more complex model will account for differing IR and visible opacities, as well as particle scattering and other complex microphysics. From experience on Earth and within the solar system, cloud systems are highly complex and variable, with shifting cloud coverage and structure. The mid infrared in particular may allow for an observational window to probe deeper atmospheric layers and begin to characterize cloud composition. In current retrieval codes, clouds are generally designed from a simple model based on a given particle distribution (Ackerman and Mark S. Marley, 2001), or simply as a gray cloud deck at a specified pressure level. Both of these models are implemented in petitRADTRANS. These models do not agree well with microphysical models, and lead to substantial difficulties in the interpretation of retrieved spectra. This remains an open problem for atmospheric retrievals, and we do not attempt to examine cloud effects in this work, instead choosing the simple, though unrealistic case of a clear atmosphere. (Schlawin et al., 2018) examines potential impacts of clouds on atmospheric retrievals with the MIRI LRS.

4.2 BAYESIAN INFERENCE

An atmospheric retrieval is the process of extracting information about physical parameters from a measured spectrum. In general this procedure involves comparing the data to a series of template spectra with known parameters and identifying the best fit model. Unfortunately for astronomers, atmospheres are complicated: typical one 1D models still require many (>15) parameters to generate a somewhat realistic model. This results in a very large parameter space in which to search for the correct set of properties that describe our measurement.

Monte Carlo methods, including Nested Sampling, are used to effectively search this large space using the Baysian evidence as a goodness-of-fit metric. Here we will follow (Joshua S. Speagle, 2019) to provide a brief overview of Bayesian inference.

To measure the likelihood of a given model, we turn to Bayes' Theorem:

$$P(\mathbf{\Theta}_M|\mathbf{D}, M) = \frac{P(\mathbf{D}|\mathbf{\Theta}, M)P(\mathbf{\Theta}|M)}{P(\mathbf{D}|M)} \tag{9}$$

In our notation, $\mathbf{\Theta}$ is the set of parameters that describe a model M, that is fit to the data $\mathbf{D}$. Bayes' theorem asks what is the probability that the parameters $\mathbf{\Theta}$ are true given the data and model. The distributions for each parameter are the **posterior** distributions.

This is then related to the **likelihood** $P(\mathbf{D}|\mathbf{\Theta}, M)$ of measuring the data given the model, the **prior** probability $P(\mathbf{\Theta}|M)$ which describes our degree of belief in our model and the **evidence** $P(\mathbf{D}|M)$, which is marginalized over all possible $\mathbf{\Theta}$ and quantifies how well the model describes the data. To simplify notation, we adopt the following convention for Bayes' theorem:

$$\mathcal{P}(\mathbf{\Theta}) = \frac{\mathcal{L}(\mathbf{\Theta})\pi(\mathbf{\Theta})}{\mathcal{Z}} \tag{10}$$

In general, the goal of an atmospheric retrieval is to find the best fit model by maximizing the evidence $\mathcal{Z}$, and as a by product finding the marginalized posterior distributions for each parameter. This comes with many challenges, especially when dealing with large numbers of parameters. Selection of the priors and model will determine the extent to which a result can be interpreted, while sampling large parameter spaces and computing likelihoods introduces substantial numerical challenges. The Markov Chain Monte Carlo method and the Nested Sampling method described below attempt to solve the challenges of exploring a large parameter space.

4.2.1 MCMC

Foreman-Mackey et al., 2013 MacKay, 2003

4.2.2 Nested Sampling

Nested sampling attempts to address several of the shortcomings of MCMC methods while simultaneously improving computational efficiency (Skilling, 2004). A particular strength of the method is in the sampling of highly multimodal distributions, removing the problem where an MCMC approach may get stuck in a single local maximum. MCMC methods generate samples 'proportional to' the true posterior distributions, which lead to difficulties in computing the evidence $\mathcal{Z}$ (Joshua S Speagle, 2020). In contrast, nested sampling puts the evidence first and provides estimates of the posterior distributions from the importance weights of the final set of samples. First described in (Skilling, 2004), nested sampling has been adopted as the sampling algorithm of choice within the astrophysics community (Buchner et al., 2014; F. Feroz et al., 2009; Farhan Feroz et al., 2019; Joshua S Speagle, 2020).

With the goal of parameter estimation, nested sampling attempts to estimate the evidence $\mathcal{Z}$ rather than directly sampling the posteriors (Skilling, 2004). This is done by integrating over the entire parameter space of $\mathbf{\Theta}$

$$\mathcal{Z} = \int_{\Omega_{\mathbf{\Theta}}} \mathcal{L}(\mathbf{\Theta})\pi(\mathbf{\Theta})d\mathbf{\Theta} \tag{11}$$

This is difficult.

Rather than attempting to directly solve the entire multidimensional integral, nested sampling transforms this into an integration over the *prior* volume X:

$$\mathcal{Z} = \int_{\Omega_{\mathbf{\Theta}}} \mathcal{L}(\mathbf{\Theta})\pi(\mathbf{\Theta})d\mathbf{\Theta} = \int_0^1 \mathcal{L}(X)dX \tag{12}$$

This is now a contour integral over isocontours $\mathcal{L}(X)$ which bound the prior volume

$$X(\lambda) = \int_{\Omega_{\mathbf{\Theta}}:\mathcal{L}(\mathbf{\Theta})\geq\lambda} \pi(\mathbf{\Theta})d\mathbf{\Theta} \tag{13}$$

which is the fraction of the prior where the likelihood of the data given the model is above some threshold λ. The integration is now simplified into a 1D integration over X, given proper prior selection.

Method

Consider a parameter space with D dimensions. We will describe this space as a unit hypercube, where each parameter runs from 0 to 1. Priors are thus transformations from this space to a physical parameter space. Often the prior is a uniform distribution, which simply scales the space, but it may also be an informative prior such as a normal distribution centered at an expected physical value. In order to sample this space, N_L 'live points' are generated, each of which provides a set of parameters $\mathbf{\Theta}$. N_L must be greater than $D+1$, and typically values on the order of $50 \times D$ are used (F. Feroz et al., 2009). Using a likelihood function $\mathcal{L}(\mathbf{\Theta})$, the evidence $\mathcal{Z}$ can be computed by comparing the model to the data. Having computed the evidence at each point, the live points are then sorted and the point with the lowest evidence is discarded. A set of ellipsoids is drawn around the remaining points. The procedure for computing these ellipsoids is given in (F. Feroz and Hobson, 2008; F. Feroz et al., 2009). By using a set of ellipsoids, multiple modes in the parameter space can be encompassed. Once the ellipsoids bounding the remaining points are drawn, a new sample is drawn from within the restricted sample space. The evidence for the new point is computed, and it is accepted if the evidence is greater than the minimum evidence of the previous remaining set of points. The entire procedure is repeated until some convergence criteria is satisfied, with each iteration resulting in a smaller volume being encompassed by the ellipsoids, nested within the previous volume.

This procedure can be improved in many ways, including importance nested sampling (Farhan Feroz et al., 2019) and dyamic nested sampling (Joshua S Speagle, 2020).

4.2.3 Multinest

For our implementation of an atmospheric retrieval code, we chose to use the Multinest algorithm (F. Feroz et al., 2009) using the pyMultinest wrapper (Buchner et al., 2014) and using importance nested sampling to improve the accuracy of the Bayesian evidence calculation (Farhan Feroz et al., 2019). This particular implementation of nested sampling is commonly used in atmospheric retrieval codes due to its fast Fortran implementation, though it was initially developed for cosmological problems.

Using the pyMultinest package, we implemented the required log-prior function which transforms the unit hypercube to physical parameter space and the log-likelihood function used to compare the model to the data. The full code is available at `https://github.com/nenasedk/petitRetrieval`, and is based of the emission spectrum retrieval described in (P. Mollière et al., 2019). Retrievals were typically performed using 500 or 1000 live points, with the convergence criteria

$$\Delta \ln \mathcal{Z} = \ln Z_i - Z_{i+1} \tag{14}$$

set to 0.3 for parameter estimation and 0.8 for model comparison, as suggested in the pyMultinest documentation.

4.3 OBSERVATIONS

The targets used in our retrieval study are guided by the JWST ERS and GTO programs. This allows us to use well-defined observing strategies for each object, and present a clear case for the science that can be accomplished with these observations. While all three were discussed in Chapter 1, we will now outline the proposed observing strategies and science cases for each target.

VHS-1256B

VHS-1256b is a young (0.2Gyr), high mass (11.2M_{Jup}) planet at a distance of 12.7pc (Bowler, 2016). The wide separation of 8" makes it an easy target for observation with the MRS, as its host star will fall outside of the FoV. It has a J-band magnitude of 16.662, and a late L spectral type (Miles et al., 2018). As an object of interest for the JWST ERS program 1386, it will be observed with the NIRCam imager, along with both the NIRSpec and MRS spectrometers (Hinkley et al., 2019). Using the MRS, VHS-1256b will be observed using a SLOW readout pattern, using 30 groups per integration, with one integration per exposure using a 2 point dither pattern. This results in a total exposure time of 1433.395s in each of the MRS sub-bands, and will cover the full wavelength range of the MRS. It will be simultaneously imaged using the MIRIM instrument. An additional background only exposure will be taken using the same exposure parameters, but without dithering, for a total of half of the science exposure time.

Methane spectral features have been detected in the L-band spectrum of VHS-1256b (Miles et al., 2018), but mid infrared spectroscopy will allow the use of methane and other molecules to characterize atmospheric properties such as dis-equilibrium chemistry and vertical mixing (Charles A Beichman et al., 2019c).

2M1207b

2M1207b is a 1600K, 10 M_{Jup} object at wide separation from its brown dwarf primary (TWA 27) and a distance of 52.4pc (Bowler, 2016). In comparison to VHS-1256b, 2M1207b has a relatively small separation of 0.77", which is more characteristic of currently known objects. As one of the first directly imaged exoplanets, it provides a template for characterizing young, hot objects, and will be observed in the JWST GTO program 1270 (Birkmann et al., 2019). This observation will use the NIRSpec IFU, MIRIM and the MIRI MRS.

Using the MRS, 2M1207b will be observed using a FAST readout to prevent detector saturation, using 76 groups per integration, and one integration per exposure. It will use a 4 exposure dither pattern, for a total integration time of 843.612s per sub-band, covering the full wavelength range of the MRS. Combined with the NIRSpec observation, this will provide a continuous spectrum over the entire JWST wavelength range. The host star of 2M1207b is faint, allowing for good enough contrast for a straightforward observation (Charles A Beichman et al., 2019c).

WISE 0855-0714

Although it is a Y-type brown dwarf, WISE 0855 is the most similar known object to Jupiter outside our solar system that has been directly observed (Luhman, 2014). At 250K, WISE 0855 is very faint, with an H-band magnitude of 25, but its proximity at 2pc makes it an ideal target for characterization. The JWST GTO Program 1230 will observe WISE 0855 using NIRCam, NIRSpec and the MIRI MRS (Oliveira et al., 2019). It will use a FAST readout, with 180 groups per integration, and one integration per exposure for a total of 999s of integration time for each sub-band. No dithering will be used.

As a cold object, WISE 0855 provides the best known extra-solar template for older planetary mass objects. With the improved sensitivity and long wavelength coverage of JWST, it is hoped that more low mass and colder exoplanets may be directly imaged. Understanding the atmosphere of WISE 0855 will provide a great deal of insight for the challenges of such exoplanetary atmospheres. Clouds are suspected to be present (Jacqueline K Faherty et al., 2018), a feature which will be better understood using mid infrared observations.

Science Goals

Atmospheric retrievals are currently the best tools for characterizing the composition and structure of exoplanet atmospheres. Parameters such as the C/O ratio may trace the formation history of planets, and may be able to settle the debate between gravitational instability and core accretion formation models (Nikku Madhusudhan, 2012; Moses et al., 2013). From solar

Parameter	VHS-1256b	2M1207b	WISE 0855
ObsDate	0.0	0.0	0.0
Path	SHORT/LONG	SHORT/LONG	SHORT/LONG
Dither	2 point	4-point	None
Disperser	ALL	ALL	ALL
Detector	SW/LW	SW/LW	SW/LW
MRS Mode	SLOW	SLOW	FAST
Exposures	1	1	1
Integrations	1	1	1
Groups	30	76	180
Cosmic Rays	None	None	None

Table 6: Observing parameters for each selected target. Observation parameters are based on JWST proposals, and set in order to cover channels 1 through 3. For the disperser, ALL implies running a simulation for each of the SHORT/MEDIUM/LONG sub-bands. A total of 6 simulations are necessary to cover the entire wavelength range. Cosmic rays are turned off due to issues with MIRISIM.

system observations, along with our own experience on Earth, we know atmospheres are constantly changing, and time series observations will open the door to investigation of dynamics and variability. Understanding the composition and chemistry of these atmospheres will also provide insight into the diversity - and similarity - between these systems. Clouds are poorly understood within our own solar system, and are certain to be present in the atmospheres of other worlds. Perhaps the most interesting prospect is uncovering novel features that have not yet been predicted, and will open the door to new avenues of exploration.

For this work, we are primarily concerned with constraining the ability of the MRS to retrieve known input parameters. With simulated spectra from petitRADTRANS providing a ground truth, we can compare the results of retrievals over a range of fringing cases.

4.4 METHODS

Here we will outline how we generated our input spectra, and the procedure we used to perform our atmospheric retrieval.

4.4.1 Spectra Generation

We used petitRADTRANS in high resolution, line-by-line mode in order to calculate a spectrum that can be passed as input to MIRISIM. All three input spectra used are shown in Fig. 27. The parameters chosen for each target are given in table 7. All spectra cover a range of 4.8-18.5 micron in order to fully cover channels 1 through 3 of the MRS. Channel 4 is ignored due to photometric calibration issues and lack of sensitivity to faint sources.

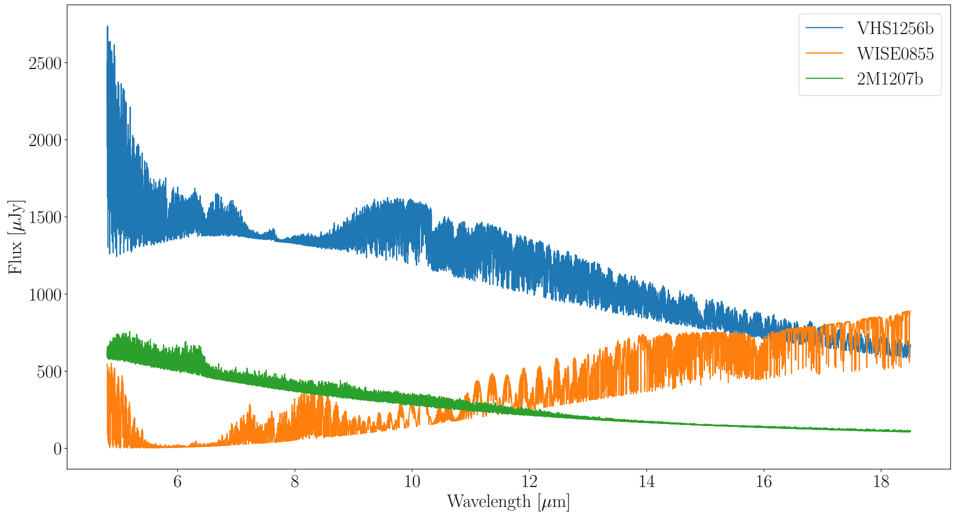

Figure 27: High resolution spectra generated by petitRADTRANS for each of the simulated targets.

The spectra generated by petitRADTRANS are in terms of the emitted flux and are in units of erg cm^{-2} m^{-2} s^{-1} Hz^{-1}. MIRISIM requires the flux incident on the detector in units of μJy, so we convert the as

$$F_{inc}[\mu\text{Jy}] = 10^{29} \times F_{em} \times \left(\frac{R_{pl}}{d_{pl}}\right)^2 \tag{15}$$

The wavelength grid produced by petitRADTRANS is log-spaced, and we use the `spectres` python package (Carnall, 2017) in order to convert to a linear spaced grid with R=12000 at 4.0μm. This ensures the input spectrum will oversample the instrumental spectral resolution by a factor of at least 4 across the whole wavelength range.

While it is possible to add a background term to a spectrum using MIRISIM, we chose not to use any background in order to improve our spectral extraction after processing with the JWST pipeline, with the understanding that errors from background subtraction will be negligible in actual data.

4.4.2 Atmospheric Retrieval Setup

Prior choice

The choice of priors is a consistent challenge when using a Bayesian framework. When performing a free-retrieval, uninformative priors must be chosen to allow the data to drive the posterior distribution. This can lead to unphysical solutions or combinations of parameters. The alternative is to use physically motivated priors, at the risk of missing unexpected phenomena.

We based our prior selection on the choices made in (P. Mollière et al., 2019). We use an uninformative uniform distribution on the temperature parameters, as well as on the log of abundance, gravity and pressure parameters. Uniformly drawing from the log of the parameters allows for better coverage of the very large parameter space (from 10^{-15} to 10^0 in each of

Parameter	VHS-1256b	2M1207b	WISE 0855
Radius [R_{Jup}]	1.29	1.5	1.17
Distance [pc]	12.7	52.4	2.23
$\log g$	4.25	3.2	4
T_{int} [K]	900	1600	250
T_{equ} [K]	3.4	10	3.4
κ_{IR}	0.01	0.01	0.01
γ	0.3	0.4	0.3
Abundances			
H_2	0.898	0.74	0.73
He	0.102	0.24	0.25
H_2O	1×10^{-3}	5×10^{-3}	5×10^{-4}
CO	1×10^{-7}	1×10^{-2}	1×10^{-15}
CO_2	1×10^{-5}	1×10^{-3}	1×10^{-14}
CH_4	3×10^{-3}	1×10^{-6}	3×10^{-4}
NH_3	1×10^{-5}	1×10^{-7}	3×10^{-3}
C_2H_2	1×10^{-8}	1×10^{-9}	...
HCN	1×10^{-10}	1×10^{-9}	1×10^{-9}
TiO	...	5×10^{-7}	...
SiO	1×10^{-6}	...	...

Table 7: Input parameters to generate spectra using petitRADTRANS. High resolution line-by-line mode was used. κ_{IR} and γ are the infrared opacity and ratio of visible to IR opacities respectively. The values chosen for these parameters are based on (P. Mollière et al., 2019). The abundances chosen are arbitrary values chosen to encompass a wide range of compositions and to test the ability of the retrieval code to recover small abundances. Where possible, values were chosen to qualitatively reflect known species present (Miles et al., 2018).

the fractional abundances). For the opacity parameters γ, δ and α we use a normal distribution centered around the expected value.

Trial runs showed that the posterior distributions for these parameters are not driven by the priors. Our prior choices and the ranges over which they cover are given in table 8.

4.5 RESULTS

4.5.1 Model Selection

Figure 28: Bayesian evidence for models of differing dimensionality.

4.5.2 Fringing Comparison

PRELIMINARY PLOTS NOT FINAL

Parameter	Prior	Constraints
$\log \delta$	$\mathcal{N}(-5.5, 2.5)$	
$\log \gamma$	$\mathcal{N}(0, 2)$	
T_{int}	$\mathcal{U}(0, 3500)$	
T_{equ}	$\mathcal{U}(0, 30)$	
$\log P_{Trans}$	$\mathcal{N}(-3, 3)$	
α	$\mathcal{N}(0.25, 0.4)$	$\alpha < 1$
$\log g$	$\mathcal{U}(2.0, 4.5)$	
$\log P_0$	$\mathcal{U}(-5, 2)$	
$\ln(X_i)$	$\mathcal{U}(-18, 0)$	$\sum X_i < 1$

Table 8: Prior choices for atmospheric retrievals. $\mathcal{U}(a, b)$ is a uniform distribution from a to b. $\mathcal{N}(\mu, \sigma)$ is a normal distribution. T_{int} corresponds to the effective temperature of an object, while T_{equ} is the equilibrium temperature between an object and a host star. For free floating objects, T_{equ} is set to 3.4K, justifying the small range of the prior. δ is in units of bar^{-1}, temperatures are in K, and pressures in bar.

Figure 29: Posterior Distributions for XX for different fringe cases

4.5.3 VHS-1256b

Figure 30: Posterior Distributions for

4.5.4 2M1207b

4.5.5 WISE 0855

4.5.6 Discussion

Figure 31: Pressure Temperature profile for

Figure 32: Best fit model for

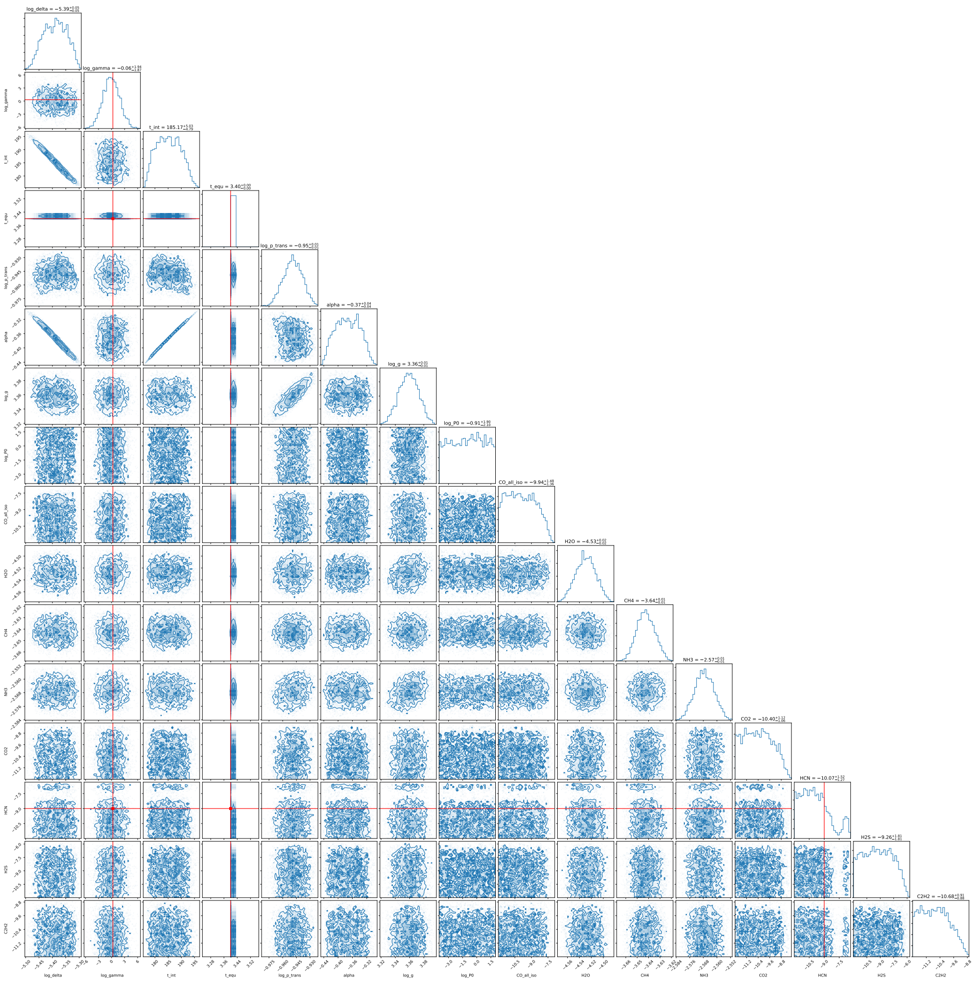

Figure 33: Posterior Distributions for 2M1207b.

Figure 34: Pressure Temperature profile for

Figure 35: Best fit model for

Figure 36: Posterior Distributions for

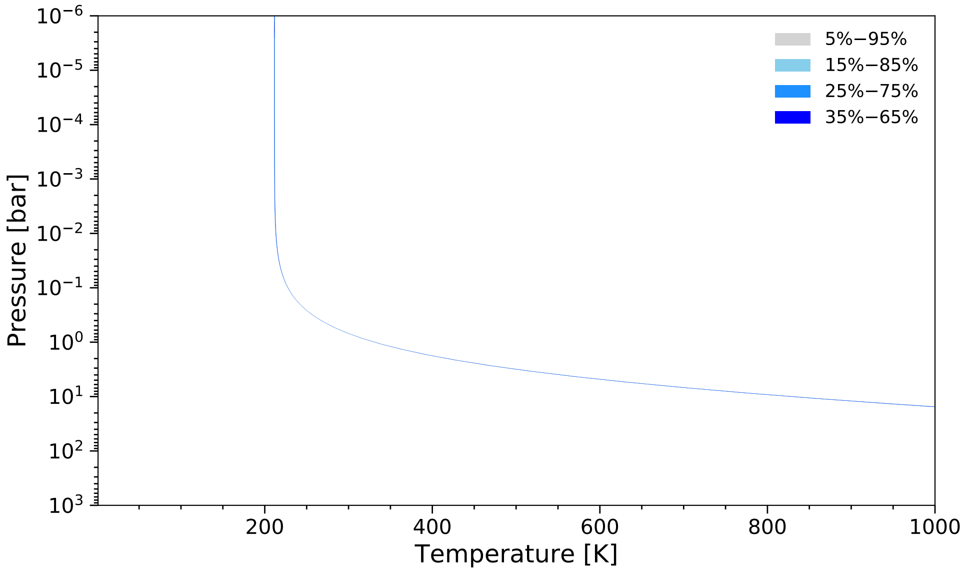

Figure 37: Pressure Temperature profile for WISE 0855.

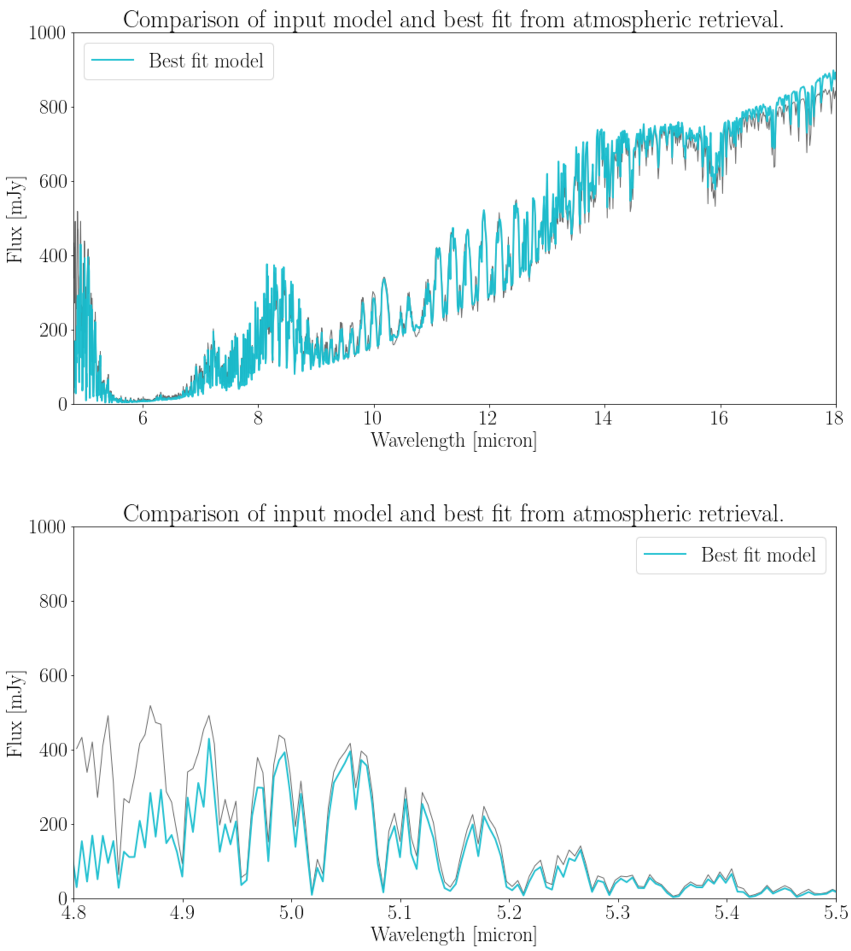

Figure 38: Best fit model for WISE0855

5 DISCUSSION AND CONCLUSIONS

5.1 SUMMARY OF RESULTS

5.1.1 Effects of fringing on cross correlations

5.1.2 Effects of fringing on atmospheric retrievals

5.1.3 Atmospheric retrievals with the MIRI MRS

5.2 DISCUSSION

5.2.1 Implications for GTO Observations

5.2.2 Caveats and Limitations

MIRISIM issues JWST pipeline issues petitRadTrans as input and output - validate models petitRadTrans spectral resolution 1D models - planets aren't 1D (Taylor et al., 2020) No background

5.2.3 Future work

Properly implement fringe model and correction Clouds + variability Designing better observing strategies Comparing different spectral models Extracting planet spectrum in contrast limited regime

5.3 CONCLUSIONS

A APPENDICES

A.1 PACKAGE REQUIREMENTS

```
astropy==3.2.1
future==0.18.2
json5==0.8.4
jsonschema==3.0.1
matplotlib==3.1.0
mpi4py==3.0.3
mpmath==1.1.0
numpy==1.16.4
pymultinest==2.7
petitradtrans==*
scipy==1.3.0
seaborn==0.9.0
spectres==2.0.0
```

WORKS CITED

Ackerman, Andrew S. and Mark S. Marley. "Precipitating condensation clouds in substellar atmospheres". *Astrophysical Journal* 596. ISSN: 15384357. DOI: 10.1088/0004-637X/765/1/75 (2001): 872–885. Print.

Aoyama, Yuhiko and Masahiro Ikoma. "Constraining Planetary Gas Accretion Rate from H α Linewidth and Intensity: Case of PDS 70 b and c". *arXiv eprint*. arXiv: arXiv:1909.08175v2 (2019). arXiv: arXiv:1909.08175v2. arXiv: arXiv:1909.08175v2.

Argyriou, Ioannis, Ruymán Azzollini, and Bart Vandenbussche. "Spectrum extraction from detector plane images for the medium-resolution spectrometer of the mid-Infrared Instrument on-board the James Webb Space Telescope." *SPIE*. 2018. 124. Print.

Argyriou, Ioannis, Bart Vandenbussche, and Martyn Wells. "Fringing solution for the mid-infrared instrument on-board the James Webb Space Telescope". *SPIE*. 2018. 127. Print.

Argyriou, Ioannis, et al. "Nature of point source fringes in mid-infrared spectra acquired with the James Webb Space Telescope". *Astronomy & Astrophysics* (2020): 1–13. Print.

Bailey, Vanessa, et al. "HD 106906 b: A planetary-mass companion outside a massive debris disk". *Astrophysical Journal Letters* 780.1. ISSN: 20418205. DOI: 10.1088/2041-8205/780/1/L4. arXiv: 1312.1265 (2014): 2–7. arXiv: 1312.1265. arXiv: 1312.1265.

Barman, Travis S., Quinn M. Konopacky, Bruce Macintosh, and Christian Marois. "Simultaneous detection of water, methane, and carbon monoxide in the atmosphere of Exoplanet hr 8799 b". *Astrophysical Journal* 804.1. ISSN: 15384357. DOI: 10.1088/0004-637X/804/1/61. arXiv: 1503.03539 (2015): 1–10. arXiv: 1503.03539. arXiv: 1503.03539. Web. <http://dx.doi.org/10.1088/0004-637X/804/1/61>.

Barstow, Joanna K., et al. "A comparison of exoplanet spectroscopic retrieval tools". DOI: 10.1093/mnras/staa548. arXiv: 2002.01063 (2020). arXiv: 2002.01063. arXiv: 2002.01063. Web. <http://arxiv.org/abs/2002.01063>.

Batalha, Natasha E., et al. " Strategies for Constraining the Atmospheres of Temperate Terrestrial Planets with JWST ". *The Astrophysical Journal* 856.2. ISSN: 2041-8213. DOI: 10.3847/2041-8213/aab896. arXiv: 1803.07983 (2018): L34. arXiv: 1803.07983. arXiv: 1803.07983. Web. <http://dx.doi.org/10.3847/2041-8213/aab896>.

Baudino, Jean-loup, et al. "Toward the Analysis of JWST Exoplanet Spectra : Identifying Troublesome Model Parameters". *The Astrophysical Journal* 850.2. ISSN: 1538-4357. DOI: 10.3847/1538-4357/aa95be (2017): 150. Web. <http://dx.doi.org/10.3847/1538-4357/aa95be>.

Beamín, J. C., et al. "Temperature constraints on the coldest brown dwarf known: WISE 0855-0714". *Astronomy and Astrophysics* 570. ISSN: 14320746. DOI: 10.1051/0004-6361/201424505 (2014): 1–4. Print.

Bean, Jacob L., et al. "The transiting exoplanet community early release science program for JWST". *Publications of the Astronomical Society of the Pacific* 130.993. DOI: 10.1088/1538-3873/aadbf3. arXiv: 1803.04985 (2018): 1–20. arXiv: 1803.04985. arXiv: 1803.04985.

Behmard, Aida, Erik A. Petigura, and Andrew W. Howard. "Data-driven Spectroscopy of Cool Stars at High Spectral Resolution". *The Astrophysical Journal* 876.1. DOI: 10.3847/1538-4357/ab14e0. arXiv: arXiv:1904.00094v1 (2019): 68. arXiv: arXiv:1904.00094v1. arXiv: arXiv:1904.00094v1.

Beichman, C., et al. "Wise y dwarfs as probes of the brown dwarf-exoplanet connection". *Astrophysical Journal* 783.2. ISSN: 15384357. DOI: 10.1088/0004-637X/783/2/68. arXiv: 1401.1194 (2014). arXiv: 1401.1194. arXiv: 1401.1194.

Beichman, Charles A., Pierre-olivier Lagage, and Marie Ygouf. "1188 - Spectroscopy of Young , Widely Separated Exoplanets". 4. Print.

Beichman, Charles A., et al. "1194 - Characterization of the HR 8799 planetary system and planet search". Print.

Beichman, Charles A and Thomas P Greene. "Observing Exoplanets with the James Webb Space Telescope". *Handbook of Exoplanets* 2009. DOI: 10.1007/978-3-319-55333-7_85 (2018): 1283–1308. Print.

Beichman, Charles A, et al. "Astro2020 Science White Paper: Direct Imaging and Spectroscopy of Exoplanets with the James Webb Space Telescope". *Astro2020 Science White Paper*. Web. <https://jwst.stsci.edu/observing-programs/approved-gto-programs.>.

Benneke, Bjoern and Sara Seager. "Atmospheric retrieval for super-earths: Uniquely constraining the atmospheric composition with transmission spectroscopy". *Astrophysical Journal* 753.2. ISSN: 15384357. DOI: 10.1088/0004-637X/753/2/100. arXiv: 1203.4018 (2012). arXiv: 1203.4018. arXiv: 1203.4018.

Benneke, Björn. "Bayesian Atmospheric Retrieval for Exoplanets". PhD Thesis. Massachusetts Institute of Technology, 2013. Print.

Benneke, Björn, et al. "Water Vapor and Clouds on the Habitable-zone Sub-Neptune Exoplanet K2-18b". *The Astrophysical Journal* 887.1. ISSN: 2041-8213. DOI: 10.3847/2041-8213/ab59dc. arXiv: 1909.04642 (2019): L14. arXiv: 1909.04642. arXiv: 1909.04642.

Biller, Beth. "The time domain for brown dwarfs and directly imaged giant exoplanets: the power of variability monitoring". *Astronomical Review* 13.1. ISSN: 2167-2857. DOI: 10.1080/21672857.2017.1303105 (2017): 1–27. Web. <http://dx.doi.org/10.1080/21672857.2017.1303105>.

Biller, Beth A. and Mickaël Bonnefoy. "Exoplanet Atmosphere Measurements from Direct Imaging". *Handbook of Exoplanets*. DOI: 10.1007/978-3-319-55333-7_101. arXiv: arXiv:1807.05136v1 (2018): 2107–2135. arXiv: arXiv:1807.05136v1. arXiv: arXiv:1807.05136v1.

Birkmann, Stephan, Pierre-olivier Lagage, and Pierre Ferruit. "1270 - Characterizing the TWA 27 system". Print.

Blanco-Cuaresma, Sergi. "Modern stellar spectroscopy caveats". *Monthly Notices of the Royal Astronomical Society* 486.2. arXiv: arXiv:1902.09558v2 (2019): 2075–2101. arXiv: arXiv:1902.09558v2. arXiv: arXiv:1902.09558v2.

Boccaletti, A., et al. "The Mid-Infrared Instrument for the James Webb Space Telescope , V: Predicted Performance of the MIRI Coronagraphs". *Publi-*

cations of the Astronomical Society of the Pacific* 127.953. ISSN: 00046280. DOI: 10.1086/682256. arXiv: 1508.02352 (2015): 633–645. arXiv: 1508.02352. arXiv: 1508.02352.

Bodis, Lorant. "Quantification of spectral similarity towards automatic spectra verification". Diss. ETH Zurich, 2007. Web. <https://doi.org/10.3929/ethz-a-005479205>.

Bouchet, Patrice, et al. "The Mid-Infrared Instrument for the James Webb Space Telescope, III: MIRIM, The MIRI Imager". *Publications of the Astronomical Society of the Pacific* 127.953. ISSN: 00046280, 15383873 (2015): 612–622. Web. <http://www.jstor.org/stable/10.1086/682254>.

Bowler, Brendan P. "Imaging Extrasolar Giant Planets". *Publications of the Astronomical Society of the Pacific* 128.968. ISSN: 1538-3873. DOI: 10.1088/1538-3873/128/968/102001 (2016): 1–38. Web. <http://dx.doi.org/10.1088/1538-3873/128/968/102001>.

Buchner, J., et al. "X-ray spectral modelling of the AGN obscuring region in the CDFS: Bayesian model selection and catalogue". *Astronomy and Astrophysics* 564. ISSN: 14320746. DOI: 10.1051/0004-6361/201322971. arXiv: 1402.0004 (2014): 1–25. arXiv: 1402.0004. arXiv: 1402.0004.

Buenzli, Esther, et al. "Cloud Structure of the Nearest Brown Dwarfs II: High Amplitude Variability for Luhman 16 A and B In and Out of the 0.99 μm FeH Feature". *Astrophysical Journal* 812.2. ISSN: 15384357. DOI: 10.1088/0004-637X/812/2/163. arXiv: 1509.06148 (2015). arXiv: 1509.06148. arXiv: 1509.06148.

Buenzli, Esther, et al. "Cloud structure of the nearest brown dwarfs: Spectroscopic variability of Luhman 16AB from the Hubble space telescope". *Astrophysical Journal* 798.2. ISSN: 15384357. DOI: 10.1088/0004-637X/798/2/127. arXiv: 1411.0003 (2015). arXiv: 1411.0003. arXiv: 1411.0003.

Burningham, Ben, et al. "Retrieval of atmospheric properties of cloudy L dwarfs". *Monthly Notices of the Royal Astronomical Society* 470.1. ISSN: 13652966. DOI: 10.1093/MNRAS/STX1246. arXiv: 1701.01257 (2017): 1177–1197. arXiv: 1701.01257. arXiv: 1701.01257.

Burrows, Adam, W. B. Hubbard, J. I. Lunine, and James Liebert. "The theory of brown dwarfs and extrasolar giant planets". *Reviews of Modern Physics* 73.3. ISSN: 00346861. DOI: 10.1103/RevModPhys.73.719. arXiv: 0103383 [astro-ph] (2001): 719–765. arXiv: 0103383 [astro-ph]. arXiv: 0103383 [astro-ph].

Burrows, Adam, David Sudarsky, and Jonathan I. Lunine. "Beyond the T Dwarfs: Theoretical Spectra, Colors, and Detectability of the Coolest Brown Dwarfs". *The Astrophysical Journal* 596. DOI: 10.1086/377709. arXiv: arXiv:1306.2144v2 (2003): 587–596. arXiv: arXiv:1306.2144v2. arXiv: arXiv:1306.2144v2. Web. <http://dx.doi.org/10.3847/0004-6256/152/6/217>.

Bushouse, Howard, Michael Droettboom, and Perry Greenfield. "The James Webb Space Telescope Data Calibration Pipeline". *14th Python in Science Conf.* 2015. 289. arXiv: 0606175 [astro-ph].

Carnall, A. C. "SpectRes: A Fast Spectral Resampling Tool in Python". Edinburgh. arXiv: 1705.05165. Web. <http://arxiv.org/abs/1705.05165>.

Chauvin, G., et al. "A giant planet candidate near a young brown dwarf Direct VLT/NACO observations using IR wavefront sensing". *Astronomy* *and Astrophysics* 425.2. ISSN: 00046361. DOI: 10.1051/0004-6361:200400056 (2004): 29–32. Print.

Chauvin, G., et al. "Orbital characterization of the β Pictoris b giant planet". *Astronomy and Astrophysics* 542. ISSN: 00046361. DOI: 10.1051/0004-6361/201118346. arXiv: 1202.2655 (2012): 1–9. arXiv: 1202.2655. arXiv: 1202.2655.

Chen, Howard, Eric T. Wolf, Zhuchang Zhan, and Daniel E. Horton. "Habitability and Spectroscopic Observability of Warm M-dwarf Exoplanets Evaluated with a 3D Chemistry-Climate Model". *The Astrophysical Journal* 886.1. DOI: 10.3847/1538-4357/ab4f7e. arXiv: 1907.10048 (2019): 23. arXiv: 1907.10048. arXiv: 1907.10048. Web. <http://arxiv.org/abs/1907.10048>.

Chilcote, Jeffrey, et al. " 1–2.4 μ m Near-IR Spectrum of the Giant Planet β Pictoris b Obtained with the Gemini Planet Imager ". *The Astronomical Journal* 153.4. ISSN: 0004-6256. DOI: 10.3847/1538-3881/aa63e9. arXiv: 1703.00011 (2017): 182. arXiv: 1703.00011. arXiv: 1703.00011. Web. <http://dx.doi.org/10.3847/1538-3881/aa63e9>.

Chilcote, Jeffrey, et al. "The first H-band spectrum of the giant planet β Pictoris b". *Astrophysical Journal Letters* 798.1. ISSN: 20418213. DOI: 10.1088/2041-8205/798/1/L3 (2015): 1–5. Print.

Christiaens, Valentin, et al. "Evidence for a Circumplanetary Disk around Protoplanet PDS 70 b". *The Astrophysical Journal* 877.2. ISSN: 2041-8213. DOI: 10.3847/2041-8213/ab212b. arXiv: 1905.06370 (2019): L33. arXiv: 1905.06370. arXiv: 1905.06370. Web. <http://dx.doi.org/10.3847/2041-8213/ab212b>.

Consortium, Miri European. "MIRISim Documentation" (2018). Print.

Cooper, Curtis S, David Sudarsky, John A Milsom, and Jonathan I Lunine. "Modeling the Formation of Clouds in Brown Dwarf Atmospheres". *The Astrophysical Journal* 156.2. DOI: 10.1086/367763. arXiv: 0205192v3 [arXiv:astro-ph] (2003): 1320–1337. arXiv: 0205192v3 [arXiv:astro-ph]. arXiv: 0205192v3 [arXiv:astro-ph].

Cossou, Christophe. "MIRISim Spreadsheet and Quick examples". Print.

Crossfield, I. J.M., et al. "A global cloud map of the nearest known brown dwarf". *Nature* 505.7485. ISSN: 00280836. DOI: 10.1038/nature12955 (2014): 654–656. Web. <http://dx.doi.org/10.1038/nature12955>.

Currie, Thayne, et al. "Direct imaging confirmation and characterization of a dust-enshrouded candidate exoplanet orbiting fomalhaut". *Astrophysical Journal Letters* 760.2. ISSN: 20418205. DOI: 10.1088/2041-8205/760/2/L32 (2012): 6–11. Print.

Cushing, Michael C., et al. "The discovery of y dwarfs using data from the wide-field infrared survey explorer (WISE)". *Astrophysical Journal* 743.1. ISSN: 15384357. DOI: 10.1088/0004-637X/743/1/50. arXiv: 1108.4678 (2011). arXiv: 1108.4678. arXiv: 1108.4678.

Danielski, Camilla, et al. " Atmospheric Characterization of Directly Imaged Exoplanets with JWST /MIRI ". *The Astronomical Journal* 156.6. ISSN: 1538-3881. DOI: 10.3847/1538-3881/aae651. arXiv: 1810.00894 (2018): 276. arXiv: 1810.00894. arXiv: 1810.00894.

De Rosa, Robert J., et al. "Spectroscopic characterization of HD 95086 b with the Gemini Planet Imager". *The Astrophysical Journal* 824.2. ISSN: 1538-4357.

DOI: 10.3847/0004-637x/824/2/121. arXiv: 1604.01411 (2016): 121. arXiv: 1604.01411. arXiv: 1604.01411. Web. <http://dx.doi.org/10.3847/0004-637X/824/2/121>.

Des Marais, David J., et al. "Remote sensing of planetary properties and biosignatures on extrasolar terrestrial planets". *Astrobiology* 2.2. ISSN: 15311074. DOI: 10.1089/15311070260192246 (2002): 153–181. Print.

Faherty, Jacqueline K., et al. "Signatures of cloud, temperature, and gravity from spectra of the closest brown dwarfs". *Astrophysical Journal* 790.2. ISSN: 15384357. DOI: 10.1088/0004-637X/790/2/90 (2014). Print.

Faherty, Jacqueline K, C G Tinney, Andrew Skemer, and Andrew J Monson. "Indications of water clouds in the coldest known brown dwarf". *The Astrophysical Journal Letters* 793.1. arXiv: arXiv:1408.4671v2 (2018). arXiv: arXiv:1408.4671v2. arXiv: arXiv:1408.4671v2.

Fegley, Bruce and Katharina Lodders. "Chemical Models of the Deep Atmospheres of Jupiter and Saturn". *Icarus* 110 (1994): 117–154. Print.

Feng, Y. Katherina, et al. "Characterizing Earth Analogs in Reflected Light: Atmospheric Retrieval Studies for Future Space Telescopes". *The Astronomical Journal* 155.5. ISSN: 1538-3881. DOI: 10.3847/1538-3881/aab95c (2018): 200. Web. <http://dx.doi.org/10.3847/1538-3881/aab95c>.

Ferguson, Henry, Perry Greenfield, and Alberto Conti. "JWST Astronomy Data Analysis Tools Roadmap Documentation v0.1". Print.

Feroz, F. and M. P. Hobson. "Multimodal nested sampling: An efficient and robust alternative to Markov Chain Monte Carlo methods for astronomical data analyses". *Monthly Notices of the Royal Astronomical Society* 384.2. ISSN: 00358711. DOI: 10.1111/j.1365-2966.2007.12353.x. arXiv: 0704.3704 (2008): 449–463. arXiv: 0704.3704. arXiv: 0704.3704.

Feroz, F., M. P. Hobson, and M. Bridges. "MultiNest: An efficient and robust Bayesian inference tool for cosmology and particle physics". *Monthly Notices of the Royal Astronomical Society* 398.4. ISSN: 00358711. DOI: 10.1111/j.1365-2966.2009.14548.x. arXiv: 0809.3437 (2009): 1601–1614. arXiv: 0809.3437. arXiv: 0809.3437.

Feroz, Farhan, Michael P. Hobson, Ewan Cameron, and Anthony N. Pettitt. "Importance Nested Sampling and the MultiNest Algorithm". *The Open Journal of Astrophysics* 2.1. DOI: 10.21105/astro.1306.2144. arXiv: 1306.2144 (2019): 1–17. arXiv: 1306.2144. arXiv: 1306.2144.

Fisher, Chloe, et al. "Interpreting High-Resolution Spectroscopy of Exoplanets Using Cross-Correlations and Supervised Machine Learning". arXiv: 1910.11627 (2019): 1–15. arXiv: 1910.11627. arXiv: 1910.11627. Web. <http://arxiv.org/abs/1910.11627>.

Foreman-Mackey, Daniel. "corner.py: Scatterplot matrices in Python". *The Journal of Open Source Software* 1.2. ISSN: 2475-9066. DOI: 10.21105/joss.00024 (2016): 24. Print.

Foreman-Mackey, Daniel, David W. Hogg, Dustin Lang, and Jonathan Goodman. "emcee : The MCMC Hammer ". *Publications of the Astronomical Society of the Pacific* 125.925. ISSN: 00046280. DOI: 10.1086/670067. arXiv: 1202.3665 (2013): 306–312. arXiv: 1202.3665. arXiv: 1202.3665.

Fu, Qiang and K. N. Liou. "On the correlated k-distribution method for radiative transfer in nonhomogeneous atmospheres". *Journal of the Atmo-*

spheric Sciences 49.22. ISSN: 00224928. DOI: 10.1175/1520-0469(1992)049<2139:otcdmf>2.0.co;2 (1992): 2139–2156. Print.

Galicher, Raphael, et al. "M-band imaging of the hr 8799 planetary system using an innovative loci-based background subtraction technique". *The Astrophysical Journal Letters* 41. DOI: 10.1088/2041-8205/739/2/L41 (2011): 3–7. Print.

Gandhi, Siddharth and Nikku Madhusudhan. "Retrieval of exoplanet emission spectra with HyDRA". *Monthly Notices of the Royal Astronomical Society* 474.1. ISSN: 13652966. DOI: 10.1093/mnras/stx2748. arXiv: 1710.06433 (2018): 271–278. arXiv: 1710.06433. arXiv: 1710.06433.

Garcia, E. Victor, et al. "Individual, Model-independent Masses of the Closest Known Brown Dwarf Binary to the Sun". *The Astrophysical Journal* 846.2. ISSN: 1538-4357. DOI: 10.3847/1538-4357/aa844f. arXiv: 1708.02714 (2017): 97. arXiv: 1708.02714. arXiv: 1708.02714.

Garland, R. and P. G. J. Irwin. "Effectively Calculating Gaseous Absorption in Radiative Transfer Models of Exoplanetary and Brown Dwarf Atmospheres". *arXiv eprint* March. arXiv: 1903.03997 (2019). arXiv: 1903.03997. arXiv: 1903.03997. Web. <http://arxiv.org/abs/1903.03997>.

Gauza, Bartosz, et al. "Discovery of a young planetary mass companion to the nearby M dwarf VHS J125601.92-125723.9". *Astrophysical Journal* 804.2. ISSN: 15384357. DOI: 10.1088/0004-637X/804/2/96. arXiv: 1505.00806 (2015): 1–18. arXiv: 1505.00806. arXiv: 1505.00806. Web. <http://dx.doi.org/10.1088/0004-637X/804/2/96>.

Glasse, Alistair, et al. "The Mid-Infrared Instrument for the James Webb Space Telescope , IX: Predicted Sensitivity". *Publications of the Astronomical Society of the Pacific* 127.953. ISSN: 00046280. DOI: 10.1086/682259. arXiv: 1508.02427 (2015): 686–695. arXiv: 1508.02427. arXiv: 1508.02427.

Goody, Richard, Robert West, Luke Chen, and David Crisp. "The correlated-k method for radiation calculations in nonhomogeneous atmospheres". *Journal of Quantitative Spectroscopy and Radiative Transfer* 42.6. ISSN: 00224073. DOI: 10.1016/0022-4073(89)90044-7 (1989): 539–550. Print.

Gordon, I. E., et al. "The HITRAN2016 molecular spectroscopic database". *Journal of Quantitative Spectroscopy and Radiative Transfer* 203. ISSN: 00224073. DOI: 10.1016/j.jqsrt.2017.06.038 (2017): 3–69. Print.

Goyal, Jayesh M., et al. "Fully scalable forward model grid of exoplanet transmission spectra". *Monthly Notices of the Royal Astronomical Society* 482.4. ISSN: 13652966. DOI: 10.1093/mnras/sty3001. arXiv: 1810.12971 (2019): 4503–4513. arXiv: 1810.12971. arXiv: 1810.12971.

GRAVITY Collaboration, et al. "Peering into the formation history of beta Pictoris b with VLTI/GRAVITY long baseline interferometry". *Astronomy & Astrophysics* 633. DOI: 10.1051/0004-6361/201936898. arXiv: 1912.04651 (2020): 1–21. arXiv: 1912.04651. arXiv: 1912.04651. Web. <http://arxiv.org/abs/1912.04651>.

Greenbaum, Alexandra Z., et al. "GPI Spectra of HR 8799 c, d, and e from 1.5 to 2.4 μm with KLIP Forward Modeling". *The Astronomical Journal* 155.6. ISSN: 0004-6256. DOI: 10.3847/1538-3881/aabcb8. arXiv: 1804.07774 (2018): 226. arXiv: 1804.07774. arXiv: 1804.07774.

Guillot, T. "On the radiative equilibrium of irradiated planetary atmospheres". *Astronomy and Astrophysics* 520.18. ISSN: 00046361. DOI: 10.1051/0004-

6361/200913396. arXiv: 1006.4702 (2010): 1–13. arXiv: 1006.4702. arXiv: 1006.4702.

Haffert, S. Y., et al. "Two accreting protoplanets around the young star PDS 70". *Nature Astronomy* 3.8. ISSN: 23973366. DOI: 10.1038/s41550-019-0780-5 (2019): 749–754. Web. <http://dx.doi.org/10.1038/s41550-019-0780-5>.

Helling, Christiane and Sarah Casewell. "Atmospheres of Brown Dwarfs". *The Astronomy and Astrophysics Review* 22. arXiv: arXiv:1410.6029v2 (2014): 1–53. arXiv: arXiv:1410.6029v2. arXiv: arXiv:1410.6029v2.

Hinkley, Sasha, et al. "1386 - High Contrast Imaging of Exoplanets and Exoplanetary Systems with JWST". Print.

Hoeijmakers, H. J., et al. "Medium-resolution integral-field spectroscopy for high-contrast exoplanet imaging: Molecule maps of the β Pictoris system with SINFONI". *Astronomy and Astrophysics* 617. ISSN: 14320746. DOI: 10.1051/0004-6361/201832902. arXiv: 1802.09721 (2018): 1–11. arXiv: 1802.09721. arXiv: 1802.09721.

Irwin, P. G.J., et al. "The NEMESIS planetary atmosphere radiative transfer and retrieval tool". *Journal of Quantitative Spectroscopy and Radiative Transfer* 109.6. ISSN: 00224073. DOI: 10.1016/j.jqsrt.2007.11.006 (2008): 1136–1150. Print.

Janson, Markus, et al. "Direct imaging detection of methane in the atmosphere of GJ 504 b". *Astrophysical Journal Letters* 778.1. ISSN: 20418205. DOI: 10.1088/2041-8205/778/1/L4 (2013). Print.

JWST. "JWST Pipeline Documentation". Print.

Keppler, M., et al. "Discovery of a planetary-mass companion within the gap of the transition disk around PDS 70". *Astronomy and Astrophysics* 617. ISSN: 14320746. DOI: 10.1051/0004-6361/201832957. arXiv: 1806.11568 (2018): 1–21. arXiv: 1806.11568. arXiv: 1806.11568.

Keppler, M, et al. "Discovery of a planetary-mass companion within the gap of the transition disk around PDS 70". *Astronomy & Astrophysics* 617. DOI: 10.1051/0004-6361/201832957. arXiv: arXiv:1806.11568 (2018): 1–23. arXiv: arXiv:1806.11568. arXiv: arXiv:1806.11568.

Konopacky, Quinn M., Travis S. Barman, Bruce A. Macintosh, and Christian Marois. "Detection of carbon monoxide and water absorption lines in an exoplanet atmosphere". *Science* 339.6126. ISSN: 10959203. DOI: 10.1126/science.1232003 (2013): 1398–1401. Print.

Kreidberg, Laura. "Exoplanet Atmosphere Measurements from Transmission Spectroscopy and Other Planet Star Combined Light Observations". *Handbook of Exoplanets*. DOI: 10.1007/978-3-319-55333-7_100. arXiv: arXiv:1709.05941v2 (2018): 2083–2105. arXiv: arXiv:1709.05941v2. arXiv: arXiv:1709.05941v2.

Kreidberg, Laura, et al. "A precise water abundance measurement for the hot jupiter WASP-43b". *Astrophysical Journal Letters* 793.2. ISSN: 20418213. DOI: 10.1088/2041-8205/793/2/L27. arXiv: 1410.2255 (2014): 2–7. arXiv: 1410.2255. arXiv: 1410.2255.

Labiano-Ortega, Alvaro, et al. "The MIRI Medium Resolution Spectrometer calibration pipeline". *SPIE Astronomical Telescopes + Instrumentation*. Edinburgh, 2016. 117. Print.

Lacis, A. A. and V. Oinas. "A description of the correlated k distribution method for modeling nongray gaseous absorption, thermal emission, and multiple scattering in vertically inhomogeneous atmospheres". *Journal of Geophysical Research* 96.D5. ISSN: 01480227. DOI: 10.1029/90JD01945 (1991): 9027–9063. Print.

Lacour, S., et al. "First direct detection of an exoplanet by optical interferometry". *Astronomy & Astrophysics* 623. ISSN: 0004-6361. DOI: 10.1051/0004-6361/201935253 (2019): L11. Print.

Lafrenière, David, Christian Marois, René Doyon, and Travis Barman. "HST/nicmos detection of HR 8799 B in 1998". *Astrophysical Journal* 694.2. ISSN: 15384357. DOI: 10.1088/0004-637X/694/2/L148 (2009): 148–152. Print.

Lagage, Pierre-olivier and David Barrado. "1278 - MIRI Spectroscopic Observations of Brown Dwarfs". Print.

Lagage, Pierre-olivier, J. Bouwman, and Fred Lahuis. "1275 - Spectroscopic characterization of PSO J318". Print.

Lagage, Pierre-olivier and Thomas L Roellig. "1276 - Spectroscopic Observations of WD 0806-661B". Print.

Lagage, P, et al. "The Mid-Infrared Instrument for the James Webb Space Telescope , IV : The Low Resolution Spectrometer". *Publications of the Astronomical Society of the Pacific* 127.953. DOI: 10.1086/682255. arXiv: 1512:03000 (2015): 1–23. arXiv: 1512:03000. arXiv: 1512:03000.

Lagrange, A. M., et al. "A probable giant planet imaged in the β Pictoris disk* VLT/NaCo deep L′-band imaging". *Astronomy and Astrophysics* 493.2. ISSN: 00046361. DOI: 10.1051/0004-6361:200811325 (2009): 21–25. Print.

Lagrange, A. M., et al. "Evidence for an additional planet in the β Pictoris system". *Nature Astronomy* 3.12. ISSN: 23973366. DOI: 10.1038/s41550-019-0857-1 (2019): 1135–1142. Web. <http://dx.doi.org/10.1038/s41550-019-0857-1>.

Lahuis, F and A Boogert. "How to Get Rid of Fringes in SIRTF/IRS Data". *SFChem 2002: Chemistry as a Diagnostic of Star Formation*. Waterloo, 2003. 335. Print.

Lahuis, Fred and Michael Muller. "MIRI MRS FM Fringing Analysis". Print.

Lavie, Baptiste, et al. " HELIOS–RETRIEVAL: An Open-source, Nested Sampling Atmospheric Retrieval Code; Application to the HR 8799 Exoplanets and Inferred Constraints for Planet Formation ". *The Astronomical Journal* 154.3. ISSN: 0004-6256. DOI: 10.3847/1538-3881/aa7ed8. arXiv: 1610.03216 (2017): 91. arXiv: 1610.03216. arXiv: 1610.03216.

Lee, J. M., L. N. Fletcher, and P. G.J. Irwin. "Optimal estimation retrievals of the atmospheric structure and composition of HD189733b from secondary eclipse spectroscopy". *Monthly Notices of the Royal Astronomical Society* 420.1. ISSN: 00358711. DOI: 10.1111/j.1365-2966.2011.20013.x. arXiv: 1110.2934 (2012): 170–182. arXiv: 1110.2934. arXiv: 1110.2934.

Leggett, S. K., Caroline V. Morley, M. S. Marley, and D. Saumon. "Near-infrared photometry of Y dwarfs: Low ammonia abundance and the onset of water clouds". *Astrophysical Journal* 799.1. ISSN: 15384357. DOI: 10.1088/0004-637X/799/1/37 (2015). Print.

Li, Jianfeng, D. Brynn Hibbert, Stephen Fuller, and Gary Vaughn. "A comparative study of point-to-point algorithms for matching spectra". *Chemo-*

metrics and Intelligent Laboratory Systems 82.1-2 SPEC. ISS. ISSN: 01697439. DOI: 10.1016/j.chemolab.2005.05.015 (2006): 50–58. Print.

Line, Michael R. and Vivien Parmentier. "the Influence of Nonuniform Cloud Cover on Transit Transmission Spectra". *The Astrophysical Journal* 820.1. ISSN: 1538-4357. DOI: 10.3847/0004-637x/820/1/78. arXiv: 1511.09443 (2016): 78. arXiv: 1511.09443. arXiv: 1511.09443. Web. <http://dx.doi.org/10.3847/0004-637X/820/1/78>.

Line, Michael R., et al. "A systematic retrieval analysis of secondary eclipse spectra. I. A comparison of atmospheric retrieval techniques". *Astrophysical Journal* 775.2. ISSN: 15384357. DOI: 10.1088/0004-637X/775/2/137. arXiv: 1304.5561 (2013). arXiv: 1304.5561. arXiv: 1304.5561.

Line, Michael R., et al. "Uniform Atmospheric Retrieval Analysis of Ultracool Dwarfs. I. Characterizing Benchmarks, Gl 570D and HD 3651B". *Astrophysical Journal* 807.2. ISSN: 15384357. DOI: 10.1088/0004-637X/807/2/183. arXiv: 1504.06670 (2015): 183. arXiv: 1504.06670. arXiv: 1504.06670. Web. <http://dx.doi.org/10.1088/0004-637X/807/2/183>.

Line, Michael R., et al. "Uniform Atmospheric Retrieval Analysis of Ultracool Dwarfs. II. Properties of 11 T dwarfs". *The Astrophysical Journal* 848.2. ISSN: 1538-4357. DOI: 10.3847/1538-4357/aa7ff0. arXiv: 1612.02809 (2017): 83. arXiv: 1612.02809. arXiv: 1612.02809.

Line, Michael R, et al. "Astro2020 Science White Paper The Importance of Thermal Emission Spectroscopy for Understanding Terrestrial Exoplanets Thematic Areas". Print. Astro2020.

López-Morales, Mercedes, et al. "Detecting Earth-like Biosignatures on Rocky Exoplanets around Nearby Stars with Ground-based Extremely Large Telescopes". arXiv: 1903.09523. Web. <http://arxiv.org/abs/1903.09523>. Astro2020.

Luhman, K L. "Discovery of a ~250K Brown Dwarf at 2pc from the Sun". *The Astrophysical Journal Letters* 18. DOI: 10.1088/2041-8205/786/2/L18 (2014): 2–7. Print.

Lupu, Roxana E., et al. "Developing Atmospheric Retrieval Methods for Direct Imaging Spectroscopy of Gas Giants in Reflected Light. I. Methane Abundances and Basic Cloud Properties". *The Astronomical Journal* 152.6. ISSN: 0004-6256. DOI: 10.3847/0004-6256/152/6/217. arXiv: 1604.05370 (2016): 217. arXiv: 1604.05370. arXiv: 1604.05370. Web. <http://dx.doi.org/10.3847/0004-6256/152/6/217>.

LUVOIR Mission Concept Study Team. "The LUVOIR Final Report". Print.

MacDonald, Ryan J. and Nikku Madhusudhan. "HD 209458b in new light: evidence of nitrogen chemistry, patchy clouds and sub-solar water". *Monthly Notices of the Royal Astronomical Society* 469.2. ISSN: 0035-8711. DOI: 10.1093/mnras/stx804. arXiv: 1701.01113 (2017): 1979–1996. arXiv: 1701.01113. arXiv: 1701.01113.

Macintosh, B., et al. "Discovery and spectroscopy of the young jovian planet 51 Eri b with the Gemini Planet Imager". *Science* 350.6256. ISSN: 10959203. DOI: 10.1126/science.aac5891 (2015): 64–67. Print.

MacKay, David J.C. *Information Theory, Inference, and Learning Algorithms*. Fourth Edi. Cambridge University Press, 2003. Print.

Madhusudhan, N and S Seager. "A Temperature and Abundance Retrieval Method for Exoplanet Atmospheres". *The Astrophysical Journal* 707.1. DOI:

10.1088/0004-637X/707/1/24. arXiv: arXiv:0910.1347v2 (2009): 24–39. arXiv: arXiv:0910.1347v2. arXiv: arXiv:0910.1347v2.

Madhusudhan, Nikku. "Atmospheric Retrieval of Exoplanets". *Handbook of Exoplanets*. DOI: 10.1007/978-3-319-55333-7_104. arXiv: 1808.04824 (2018): 2153–2182. arXiv: 1808.04824. arXiv: 1808.04824.

—–."C/O ratio as a dimension for characterizing exoplanetary atmospheres". *Astrophysical Journal* 758.1. ISSN: 15384357. DOI: 10.1088/0004-637X/758/1/36. arXiv: 1209.2412 (2012). arXiv: 1209.2412. arXiv: 1209.2412.

Madhusudhan, Nikku, Marcelino Agúndez, Julianne I. Moses, and Yongyun Hu. "Exoplanetary Atmospheres—Chemistry, Formation Conditions, and Habitability". *Space Science Reviews* 205.1-4. ISSN: 15729672. DOI: 10.1007/s11214-016-0254-3. arXiv: arXiv:1604.06092v1 (2016): 285–348. arXiv: arXiv:1604.06092v1. arXiv: arXiv:1604.06092v1.

Madhusudhan, Nikku, Daniel Apai, and Siddharth Gandhi. "Atmospheric Compositions of Three Brown Dwarfs and Implications for their Formation Conditions". *arXiv eprint*. arXiv: arXiv:1612.03174v1 (2018). arXiv: arXiv:1612.03174v1. arXiv: arXiv:1612.03174v1.

Madhusudhan, Nikku, Heather Knutson, Jonathan J Fortney, and Travis Barman. "Exoplanetary Atmospheres". 2014. arXiv: arXiv:1402.1169v1. arXiv: arXiv:1402.1169v1.

Madhusudhan, Nikku, et al. "High C / O Ratio and Weak Thermal Inversion in the Very Hot Atmosphere of Exoplanet WASP-12b". *Nature* 469.7328. DOI: 10.1038/nature09602. arXiv: arXiv:1012.1603 (2011): 64–67. arXiv: arXiv:1012.1603. arXiv: arXiv:1012.1603.

Malik, Matej, et al. "Helios: an Open-Source, Gpu-Accelerated Radiative Transfer Code for Self-Consistent Exoplanetary Atmospheres". *The Astronomical Journal* 153.2. ISSN: 0004-6256. DOI: 10.3847/1538-3881/153/2/56. arXiv: 1606.05474 (2017): 56. arXiv: 1606.05474. arXiv: 1606.05474. Web. <http://dx.doi.org/10.3847/1538-3881/153/2/56>.

Malik, Matej, et al. " Self-luminous and Irradiated Exoplanetary Atmospheres Explored with HELIOS ". *The Astronomical Journal* 157.5. ISSN: 0004-6256. DOI: 10.3847/1538-3881/ab1084. arXiv: 1903.06794 (2019): 170. arXiv: 1903.06794. arXiv: 1903.06794. Web. <http://dx.doi.org/10.3847/1538-3881/ab1084>.

Malumuth, Eliot M., et al. "Removing the Fringes from Space Telescope Imaging Spectrograph Slitless Spectra". *Publications of the Astronomical Society of the Pacific* 115.804. ISSN: 0004-6280. DOI: 10.1086/345913 (2003): 218–234. Print.

Mamajek, Eric E. and Cameron P.M. Bell. "On the age of the β pictoris moving group". *Monthly Notices of the Royal Astronomical Society* 445.3. ISSN: 13652966. DOI: 10.1093/mnras/stu1894 (2014): 2169–2180. Print.

Manjavacas, Elena. "Physical characterization of brown dwarfs". Diss. Ruperto-Carola-University of Heidelberg, 2014. Print.

Marley, M S and T D Robinson. "On the Cool Side : Modeling the Atmospheres of Brown Dwarfs and Giant Planets arXiv : 1410 . 6512v1 [astro-ph . EP] 23 Oct 2014". *Annual Review of Astronomy and Astrophysics* 53. DOI: 10.1146/annurev-astro-082214-122522. arXiv: arXiv:1410.6512v1 (2015): 279–323. arXiv: arXiv:1410.6512v1. arXiv: arXiv:1410.6512v1.

Marois, Christian, Bruce Macintosh, Daniel Nadeau, and David Lafrenie. "Angular Differential Imaging: A Powerful High-Contrast Imaging Technique". *The Astrophysical Journal* 641 (2006): 556–564. Print.

Marois, Christian, et al. "Direct imaging of multiple planets orbiting the star HR 8799". *Science* 322.5906. ISSN: 00368075. DOI: 10.1126/science.1166585. arXiv: 0811.2606 (2008): 1348–1352. arXiv: 0811.2606. arXiv: 0811.2606.

Marois, Christian, et al. "Images of a fourth planet orbiting HR 8799". *Nature Letters* 468.23. DOI: 10.1038/nature09684 (2010): 8–11. Print.

Mayor, M and D Queloz. "A Jupiter-mass companion to a solar-type star". *Nature* 378 (1995): 667–668. Print.

McLatchey, R.A., et al. "AFCRL atmospheric absorption line parameters compilation". *Environmental Research Papers* 434. ISSN: 0003-6935. DOI: 10.1364/ao.20.000791 (1973): 87. Print.

Mesa, D., et al. "VLT/SPHERE exploration of the young multiplanetary system PDS70". *Astronomy and Astrophysics* 632. ISSN: 14320746. DOI: 10.1051/0004-6361/201936764. arXiv: 1910.11169 (2019): 1–12. arXiv: 1910.11169. arXiv: 1910.11169.

Miles, Brittany E., et al. "Methane in Analogs of Young Directly Imaged Exoplanets". *The Astrophysical Journal* 869.1. ISSN: 1538-4357. DOI: 10.3847/1538-4357/aae6cd. arXiv: 1810.04684 (2018): 18. arXiv: 1810.04684. arXiv: 1810.04684. Web. <http://dx.doi.org/10.3847/1538-4357/aae6cd>.

Mohanty, Subhanjoy, Ray Jayawardhana, Nuria Huelamo, and Eric Mamajek. "The Planetary Mass Companion 2MASS 1207-3932B: Temperature, Mass, and Evidence for an Edge-on Disk". *The Astrophysical Journal* 657.2. ISSN: 0004-637X. DOI: 10.1086/510877 (2007): 1064–1091. Print.

Molliere, P. and I. A.G. Snellen. "Detecting isotopologues in exoplanet atmospheres using ground-based high-dispersion spectroscopy". *Astronomy and Astrophysics* 622. ISSN: 14320746. DOI: 10.1051/0004-6361/201834169. arXiv: 1809.01156 (). arXiv: 1809.01156. arXiv: 1809.01156.

Mollière, P., et al. "Observing transiting planets with JWST: Prime targets and their synthetic spectral observations". *Astronomy and Astrophysics* 600. ISSN: 14320746. DOI: 10.1051/0004-6361/201629800. arXiv: 1611.08608 (2017): 1–23. arXiv: 1611.08608. arXiv: 1611.08608.

Mollière, P., et al. "petitRADTRANS: a Python radiative transfer package for exoplanet characterization and retrieval". *Astronomy & Astrophysics* 627. ISSN: 0004-6361. DOI: 10.1051/0004-6361/201935470. arXiv: 1904.11504 (2019): 1–17. arXiv: 1904.11504. arXiv: 1904.11504. Web. <http://arxiv.org/abs/1904.11504%7B%5C%%7D0Ahttp://dx.doi.org/10.1051/0004-6361/201935470>.

Mollière, P, et al. "Model Atmospheres of Irradiated Exoplanets: The Influence of Stellar Parameters, Metallicity and the C/O Ratio". *The Astrophysical Journal* 813.1. ISSN: 1538-4357. DOI: 10.1088/0004-637X/813/1/47 (2015): 47. Web. <http://dx.doi.org/10.1088/0004-637X/813/1/47>.

Morley, Caroline V., et al. "An L Band Spectrum of the Coldest Brown Dwarf". *The Astrophysical Journal* 858.2. ISSN: 1538-4357. DOI: 10.3847/1538-4357/aabe8b. arXiv: 1804.07771 (2018): 97. arXiv: 1804.07771. arXiv: 1804.07771. Web. <http://dx.doi.org/10.3847/1538-4357/aabe8b>.

Morley, Caroline V., et al. “Water clouds in y dwarfs and exoplanets”. *Astrophysical Journal* 787.1. ISSN: 15384357. DOI: 10.1088/0004-637X/787/1/78. arXiv: 1404.0005 (2014). arXiv: 1404.0005. arXiv: 1404.0005.

Moroz, V.I. “On the infrared spectra of Jupiter and Saturn (0.9-2.5um)”. *Soviet Astronomy* 5.6 (1962). Print.

Moses, J. I., N. Madhusudhan, C. Visscher, and R. S. Freedman. “Chemical consequences of the C/O ratio on hot jupiters: Examples from WASP-12b, CoRoT-2b, XO-1b, and HD 189733b”. *Astrophysical Journal* 763.1. ISSN: 15384357. DOI: 10.1088/0004-637X/763/1/25. arXiv: 1211.2996 (2013). arXiv: 1211.2996. arXiv: 1211.2996.

Müller, A., et al. “Orbital and atmospheric characterization of the planet within the gap of the PDS 70 transition disk”. *Astronomy and Astrophysics* 617. ISSN: 14320746. DOI: 10.1051/0004-6361/201833584. arXiv: 1806.11567 (2018): 1–10. arXiv: 1806.11567. arXiv: 1806.11567.

National Academies of Sciences Engineering and Medicine. *Exoplanet science strategy*. Washington, DC: The National Academies Press, 2018. 1–172. DOI: 10.17226/25187. Print.

Oliveira, Catarina Alves De. “Peering into the physics of brown dwarfs : spectroscopy with JWST / NIRSpec”. Web. <https://www.cosmos.esa.int/documents/739790/758041/AlvesdeOliveiraC.pdf>.

Oliveira, Catarina Alves De, et al. “1230 - The Physics of Brown Dwarfs - Part # 3”. 1. Print.

Oreshenko, Maria, et al. “Supervised Machine Learning for Inter-comparision of Model Grids of Brown Dwarfs: Application to GJ 570D and the Epsilon Indi B Binary System”. *The Astronomical Journal* 159.1. DOI: 10.3847/1538-3881/ab5955. arXiv: arXiv:1910.11795v1 (2020): 15. arXiv: arXiv:1910.11795v1. arXiv: arXiv:1910.11795v1.

Petermann, R. “Atmospheric characterization of terrestrial planets using high-resolution spectroscopy with ELT / METIS A study of Proxima Cen b”. Master’s Thesis. ETH Zurich, 2019. Print.

Quanz, Sascha P., et al. “Atmospheric characterization of terrestrial exoplanets in the mid-infrared: biosignatures, habitability & diversity”. arXiv: 1908.01316. Web. <http://arxiv.org/abs/1908.01316>. Voyage 2050 long-term plan.

Quanz, Sascha P., et al. “First results from very large telescope NACO apodizing phase plate: 4 μm images of the exoplanet β Pictoris b”. *Astrophysical Journal Letters* 722.1 PART 2. ISSN: 20418213. DOI: 10.1088/2041-8205/722/1/L49 (2010): 49–53. Print.

Rameau, J., et al. “Confirmation of the Planet Around Hd 95086 By Direct Imaging”. *The Astrophysical Journal* 779.2. ISSN: 2041-8205. DOI: 10.1088/2041-8205/779/2/l26 (2013): L26. Print.

Ressler, M. E., et al. “The Mid-Infrared Instrument for the James Webb Space Telescope , VIII: The MIRI Focal Plane System”. *Publications of the Astronomical Society of the Pacific* 127.953. ISSN: 00046280. DOI: 10.1086/682258 (2015): 675–685. Print.

Rich, Evan A., et al. “Thermal Infrared Imaging and Atmospheric Modeling of VHS J125601.92-125723.9 b: Evidence for Moderately Thick Clouds and Equilibrium Carbon Chemistry in a Hierarchical Triple System.” *The Astrophysical Journal* 830.2. ISSN: 1538-4357. DOI: 10.3847/0004-637x/830/2/114.

arXiv: 1607.06007 (2016): 114. arXiv: 1607.06007. arXiv: 1607.06007. Web. <http://dx.doi.org/10.3847/0004-637X/830/2/114>.

Rieke, G. H., et al. "The Mid-Infrared Instrument for the James Webb Space Telescope , I: Introduction". *Publications of the Astronomical Society of the Pacific* 127.953. ISSN: 00046280. DOI: 10.1086/682252 (2015): 584–594. Print.

——." The Mid-Infrared Instrument for the James Webb Space Telescope , I: Introduction ". *Publications of the Astronomical Society of the Pacific* 127.953. ISSN: 00046280. DOI: 10.1086/682252 (2015): 584–594. Print.

Rieke, G. H., et al. "The Mid-Infrared Instrument for the James Webb Space Telescope , VII: The MIRI Detectors". *Publications of the Astronomical Society of the Pacific* 127.953. ISSN: 00046280. DOI: 10.1086/682257 (2015): 665–674. Print.

Robinson, Tyler D., Karl R. Stapelfeldt, and Mark S. Marley. "Characterizing rocky and gaseous exoplanets with 2m class space-based coronagraphs". *Publications of the Astronomical Society of the Pacific* 128.960. ISSN: 00046280. DOI: 10.1088/1538-3873/128/960/025003 (2016): 1–22. Web. <http://dx.doi.org/10.1088/1538-3873/128/960/025003>.

Rothman, L. S. "AFGL atmospheric absorption line parameters compilation: 1980 version". *Applied Optics* 20.5. ISSN: 0003-6935. DOI: 10.1364/ao.20.000791 (1981): 791. Print.

Rothman, L. S., et al. "HITEMP, the high-temperature molecular spectroscopic database". *Journal of Quantitative Spectroscopy and Radiative Transfer* 111.15. ISSN: 00224073. DOI: 10.1016/j.jqsrt.2010.05.001 (2010): 2139–2150. Web. <http://dx.doi.org/10.1016/j.jqsrt.2010.05.001>.

Rothman, L. S., et al. "The HITRAN2012 molecular spectroscopic database". *Journal of Quantitative Spectroscopy and Radiative Transfer* 130. ISSN: 00224073. DOI: 10.1016/j.jqsrt.2013.07.002 (2013): 4–50. Print.

Sahlmann, J. and P. F. Lazorenko. "Mass ratio of the 2 pc binary brown dwarf LUH 16 and limits on planetary companions from astrometry". *Monthly Notices of the Royal Astronomical Society: Letters* 453.1. ISSN: 17453933. DOI: 10.1093/mnrasl/slv113. arXiv: 1506.07994 (2015): L103–L107. arXiv: 1506.07994. arXiv: 1506.07994.

Sallum, S., et al. "Accreting protoplanets in the LkCa 15 transition disk". *Nature* 527.7578. ISSN: 14764687. DOI: 10.1038/nature15761. arXiv: 1511.07456 (2015): 342–344. arXiv: 1511.07456. arXiv: 1511.07456. Web. <http://dx.doi.org/10.1038/nature15761>.

Schlawin, Everett, et al. " Clear and Cloudy Exoplanet Forecasts for JWST : Maps, Retrieved Composition, and Constraints on Formation with MIRI and NIRCam ". *The Astronomical Journal* 156.1. ISSN: 0004-6256. DOI: 10.3847/1538-3881/aac774. arXiv: 1803.08173 (2018): 40. arXiv: 1803.08173. arXiv: 1803.08173.

Schneider, Adam C., Michael C. Cushing, J. Davy Kirkpatrick, and Christopher R. Gelino. "the Collapse of the Wien Tail in the Coldest Brown Dwarf? Hubble Space Telescope Near-Infrared Photometry of WISE J085510.83-071442.5". *The Astrophysical Journal* 823.2. ISSN: 2041-8213. DOI: 10.3847/2041-8205/823/2/l35. arXiv: 1605.05618 (2016): L35. arXiv: 1605.05618. arXiv: 1605.05618. Web. <http://dx.doi.org/10.3847/2041-8205/823/2/L35>.

Seager, Sara and Drake Deming. "Exoplanet Atmospheres". *Annual Review of Astronomy and Astrophysics* 48.1. ISSN: 0066-4146. DOI: 10.1146/annurev-astro-081309-130837. arXiv: 1005.4037 (2010): 631–672. arXiv: 1005.4037. arXiv: 1005.4037.

Simkin, Susan M. "Measurements of Velocity Dispersions and Doppler Shifts from Digitized Optical Spectra". *Astronomy & Astrophysics* 32 (1974): 129–136. Print.

Sing, David K., Jonathan J. Fortney, Jonathan Tennyson, and Davide Grassi. *Astrophysics of Exoplanetary Atmospheres*. Edited by Valerio Bozza, Luigi Mancini, and Alessandro Sozzetti. Vietri sul Mare: Springer Nature, 2018. 199. DOI: 10.1007/978-3-319-89701-1. Print.

Skemer, Andrew J., et al. "First light LBT AO images of HR 8799 bcde at 1.6 and 3.3 μm: New discrepancies between young planets and old brown dwarfs". *Astrophysical Journal* 753.1. ISSN: 15384357. DOI: 10.1088/0004-637X/753/1/14. arXiv: 1203.2615 (2012). arXiv: 1203.2615. arXiv: 1203.2615.

Skemer, Andrew J., et al. "The First Spectrum of the Coldest Brown Dwarf". *The Astrophysical Journal* 826.2. ISSN: 2041-8213. DOI: 10.3847/2041-8205/826/2/l17. arXiv: 1605.04902 (2016): L17. arXiv: 1605.04902. arXiv: 1605.04902. Web. <http://dx.doi.org/10.3847/2041-8205/826/2/L17>.

Skemer, Andrew J., et al. "The LEECH Exoplanet Imaging Survey: Characterization of the Coldest Directly Imaged Exoplanet, GJ 504 b, and Evidence for Super-Stellar Metallicity". *The Astrophysical Journal* 817.2. ISSN: 1538-4357. DOI: 10.3847/0004-637x/817/2/166. arXiv: 1511.09183 (2016): 166. arXiv: 1511.09183. arXiv: 1511.09183. Web. <http://dx.doi.org/10.3847/0004-637X/817/2/166>.

Skilling, John. "Nested Sampling". *Bayesian Inference and Maximum Entropy Methods in Science and Engineering*. 2004. 395–405. Print.

Snellen, I., et al. "Combining high-dispersion spectroscopy with high contrast imaging: Probing rocky planets around our nearest neighbors". *Astronomy and Astrophysics* 576.3. ISSN: 14320746. DOI: 10.1051/0004-6361/201425018. arXiv: 1503.01136 (2015). arXiv: 1503.01136. arXiv: 1503.01136.

Snellen, Ignas, et al. "The fast spin-rotation of a young extrasolar planet". *Nature* 509.7498. ISSN: 0028-0836, 1476-4687. DOI: 10.1038/nature13253. arXiv: 1404.7506 [astro-ph.EP] (2014): 63–65. arXiv: 1404.7506 [astro-ph.EP]. arXiv: 1404.7506 [astro-ph.EP]. Web. <http://arxiv.org/abs/1404.7506%7B%5C%%7D5Cnhttp://www.arxiv.org/pdf/1404.7506.pdf>.

Soummer, Rémi, et al. "Orbital motion of HR 8799 b, c, d using hubble space telescope data from 1998: Constraints on inclination, eccentricity, and stability". *Astrophysical Journal* 741.1. ISSN: 15384357. DOI: 10.1088/0004-637X/741/1/55. arXiv: 1110.1382 (2011). arXiv: 1110.1382. arXiv: 1110.1382.

Speagle, Joshua S. "dynest: A Dynamic Nested Smpling Package for Estimating Bayesian Posteriors and Evidences". *Monthly Notices of the Royal Astronomical Society* 4. ISSN: 0035-8711. DOI: 10.1093/mnras/staa278 (2020). Print.

——."A Conceptual Introduction to Markov Chain Monte Carlo Methods". *Journal of Statistics Education*. arXiv: 1909.12313 (2019). arXiv: 1909.12313. arXiv: 1909.12313. Web. <http://arxiv.org/abs/1909.12313>.

Stephens, D. C., et al. "The 0.8-14.5 μm Spectra of mid-L to mid-T dwarfs: Diagnostics of effective temperature, grain sedimentation, gas transport, and surface gravity". *Astrophysical Journal* 702.1. ISSN: 15384357. DOI: 10.1088/0004-637X/702/1/154 (2009): 154–170. Print.

Stolker, Tomas, et al. "MIRACLES: atmospheric characterization of directly imaged planets and substellar companions at 4-5 micron. I. Photometric analysis of β Pic b, HIP 65426 b, PZ Tel B and HD 206893 B". *arXiv ePrint in Press*. arXiv: 1912.13316 (2020): 1–25. arXiv: 1912.13316. arXiv: 1912.13316. Web. <http://arxiv.org/abs/1912.13316>.

Stone, Jordan M., et al. "Adaptive Optics Imaging of Vhs 1256–1257: a Low Mass Companion To a Brown Dwarf Binary System". *The Astrophysical Journal* 818.1. ISSN: 2041-8213. DOI: 10.3847/2041-8205/818/1/l12 (2016): L12. Web. <http://dx.doi.org/10.3847/2041-8205/818/1/L12>.

Taylor, Jake, et al. "Understanding and Mitigating Biases when Studying Inhomogeneous Emission Spectra with JWST". *accepted Monthly Notices of the Royal Astronomical Society* in Press.February. arXiv: 2002.00773 (2020): 1–13. arXiv: 2002.00773. arXiv: 2002.00773. Web. <http://arxiv.org/abs/2002.00773>.

Tennyson, Jonathan and Sergei N. Yurchenko. "The ExoMol project: Software for computing large molecular line lists". *International Journal of Quantum Chemistry* 117.2. ISSN: 1097461X. DOI: 10.1002/qua.25190. arXiv: 1607.01220 (2017): 92–103. arXiv: 1607.01220. arXiv: 1607.01220.

Tennyson, Jonathan, et al. "The ExoMol database: Molecular line lists for exoplanet and other hot atmospheres". *Journal of Molecular Spectroscopy* 327. ISSN: 1096083X. DOI: 10.1016/j.jms.2016.05.002. arXiv: 1603.05890 (2016): 73–94. arXiv: 1603.05890. arXiv: 1603.05890. Web. <http://dx.doi.org/10.1016/j.jms.2016.05.002>.

Tinney, C G, et al. "The Luminosities of the Coldest Brown Dwarfs". *The Astrophysical Journal* 39.Luhman. DOI: 10.1088/0004-637X/796/1/39 (2014): 1–13. Print.

Tokunaga, Alan T. "High-Resolution Infrared Spectroscopy of Planetary Atmospheres". *Publications of the Astronomical Society of the Pacific* 95.October (1983): 691–699. Print.

Tremblin, P., et al. "Fingering convection and cloudless models for cool brown dwarf atmospheres". *Astrophysical Journal Letters* 804.1. ISSN: 20418213. DOI: 10.1088/2041-8205/804/1/L17. arXiv: 1504.03334 (2015): 6. arXiv: 1504.03334. arXiv: 1504.03334. Web. <http://dx.doi.org/10.1088/2041-8205/804/1/L17>.

Tsiaras, Angelos, et al. "Water vapour in the atmosphere of the habitable-zone eight-Earth-mass planet K2-18 b". *Nature Astronomy* 3.12. ISSN: 23973366. DOI: 10.1038/s41550-019-0878-9. arXiv: 1909.05218 (2019): 1086–1091. arXiv: 1909.05218. arXiv: 1909.05218. Web. <http://dx.doi.org/10.1038/s41550-019-0878-9>.

Turrini, D., R. P. Nelson, and M. Barbieri. "The role of planetary formation and evolution in shaping the composition of exoplanetary atmospheres".

Experimental Astronomy 40.2-3. DOI: 10.1007/s10686-014-9401-6 (2015): 501–522. Print.

VanderPlas, Jacob T. "Understanding the Lomb–Scargle Periodogram". *The Astrophysical Journal Supplement Series* 236.1. ISSN: 0067-0049. DOI: 10.3847/1538-4365/aab766. arXiv: 1703.09824 (2018): 16. arXiv: 1703.09824. arXiv: 1703.09824. Web. <http://dx.doi.org/10.3847/1538-4365/aab766>.

Villanueva, G. L., et al. "Planetary Spectrum Generator: An accurate online radiative transfer suite for atmospheres, comets, small bodies and exoplanets". *Journal of Quantitative Spectroscopy and Radiative Transfer* 217. ISSN: 00224073. DOI: 10.1016/j.jqsrt.2018.05.023. arXiv: 1803.02008 (2018): 86–104. arXiv: 1803.02008. arXiv: 1803.02008. Web. <https://doi.org/10.1016/j.jqsrt.2018.05.023>.

Vos, Johanna M., et al. "Astro2020 White Paper: The L/T Transition". arXiv: 1903.06691. Web. <http://arxiv.org/abs/1903.06691>. Astro2020.

Waldmann, I. P., et al. "T-REx. II. Retrieval of Emission Spectra". *Astrophysical Journal* 813.1. ISSN: 15384357. DOI: 10.1088/0004-637X/813/1/13. arXiv: 1508.07591 (2015): 13. arXiv: 1508.07591. arXiv: 1508.07591. Web. <http://dx.doi.org/10.1088/0004-637X/813/1/13>.

Waldmann, I. P., et al. "Tau-REx I: A next generation retrieval code for exoplanetary atmospheres". *Astrophysical Journal* 802.2. ISSN: 15384357. DOI: 10.1088/0004-637X/802/2/107. arXiv: 1409.2312 (2015): 107. arXiv: 1409.2312. arXiv: 1409.2312. Web. <http://dx.doi.org/10.1088/0004-637X/802/2/107>.

Wells, Martyn, et al. "The Mid-Infrared Instrument for the James Webb Space Telescope , VI: The Medium Resolution Spectrometer". *Publications of the Astronomical Society of the Pacific* 127.953. ISSN: 00046280. DOI: 10.1086/682281. arXiv: 1508.03070 (2015): 646–664. arXiv: 1508.03070. arXiv: 1508.03070.

Wright, Edward L., et al. "NEOWISE-R observation of the coolest known brown dwarf". *Astronomical Journal* 148.5. ISSN: 00046256. DOI: 10.1088/0004-6256/148/5/82 (2014): 2012–2015. Print.

Wright, G S, et al. "The Mid-Infrared Instrument for JWST , II : Design and Build". *Publications of the Astronomical Society of the Pacific* 127.953. DOI: 10.1086/682253. arXiv: 1508.02333 (2015): 595. arXiv: 1508.02333. arXiv: 1508.02333.

Yurchenko, Sergei N., Ahmed F. Al-Refaie, and Jonathan Tennyson. "EXO CROSS: A general program for generating spectra from molecular line lists". *Astronomy and Astrophysics* 614. ISSN: 14320746. DOI: 10.1051/0004-6361/201732531. arXiv: 1801.09803 (2018): 1–12. arXiv: 1801.09803. arXiv: 1801.09803.

Zalesky, Joseph A., Michael R. Line, Adam C. Schneider, and Jennifer Patience. "A Uniform Retrieval Analysis of Ultra-cool Dwarfs. III. Properties of Y Dwarfs". *The Astrophysical Journal* 877.1. ISSN: 1538-4357. DOI: 10.3847/1538-4357/ab16db. arXiv: 1903.11658 (2019): 24. arXiv: 1903.11658. arXiv: 1903.11658.

Zhang, Michael, Yayaati Chachan, Eliza M.R. Kempton, and Heather A. Knutson. "Forward modeling and retrievals with PLATON, a fast open-source tool". *Publications of the Astronomical Society of the Pacific* 131.997. ISSN:

00046280. DOI: 10.1088/1538-3873/aaf5ad. arXiv: 1811.11761 (2019). arXiv: 1811.11761. arXiv: 1811.11761.

Zhou, Yifan, et al. "Cloud Atlas: High-contrast Time-resolved Observations of Planetary-mass Companions". *The Astronomical Journal* 157.3. ISSN: 0004-6256. DOI: 10.3847/1538-3881/ab037f. arXiv: 1902.00085 (2019): 128. arXiv: 1902.00085. arXiv: 1902.00085. Web. <http://dx.doi.org/10.3847/1538-3881/ab037f>.

Zucker, S. "Cross-correlation and maximum-likelihood analysis : a new approach to combining cross-correlation functions". *Monthly Notices of the Royal Astronomical Society* 342 (2003): 1291–1298. Print.

Zurlo, A., et al. "First light of the VLT planet finder SPHERE: III. New spectrophotometry and astrometry of the HR 8799 exoplanetary system". *Astronomy and Astrophysics* 587. ISSN: 14320746. DOI: 10.1051/0004-6361/201526835. arXiv: 1511.04083 (2016): 1–13. arXiv: 1511.04083. arXiv: 1511.04083.